N 69 38308

NASA CR-72574

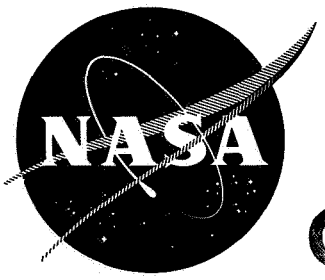

CONTRACTOR REPORT

EXPERIMENTAL STUDIES OF THE VAPORIZATION OF DROPLETS IN HEATED AIR AT HIGH PRESSURES

by

C. William Savery

prepared for

NATIONAL AERONAUTICS AND SPACE ADMINISTRATION

August 1, 1969

NASA Grant NGR 50-002-017

Technical Management
NASA Lewis Research Center
Cleveland, Ohio
Special Projects Division
Paul R. Wieber

THE UNIVERSITY OF WISCONSIN
DEPARTMENT OF MECHANICAL ENGINEERING
Madison, Wisconsin

NASA CR-72574

CONTRACTOR REPORT

EXPERIMENTAL STUDIES OF THE VAPORIZATION OF DROPLETS IN HEATED AIR AT HIGH PRESSURES

by

C. William Savery

prepared for

NATIONAL AERONAUTICS AND SPACE ADMINISTRATION

August 1, 1969

NASA Grant NGR 50-002-017

Technical Management

NASA Lewis Research Center

Cleveland, Ohio

Special Projects Division

Paul R. Wieber

THE UNIVERSITY OF WISCONSIN

DEPARTMENT OF MECHANICAL ENGINEERING

Madison, Wisconsin

EXPERIMENTAL STUDIES OF THE VAPORIZATION OF DROPLETS IN HEATED AIR AT HIGH PRESSURES

Clyde William Savery

Under the Supervision of Associate Professor Gary L. Borman

ABSTRACT

Measured histories of vaporizing n-heptane and Freon-13 droplets suspended in a heated air stream are reported. The range of air conditions was $1.5 < P < 100$ atm and $100 < T_\infty < 300^\circ$ F. Comparisons are made with film theory calculations corrected for the effects of total pressure on thermodynamic properties. Agreement was satisfactory for liquid steady-state temperatures and mass transfer rates except for Freon-13 where significant differences were found at air pressures above $1.25\ P_c$. Freon-13 droplet histories were found to be completely unsteady for pressures above 60 atm. The absence of steady-state conditions was found to correlate with the critical mixing point for the Freon-13-air system.

SUMMARY

The problem of droplet vaporization at ambient gas pressures in the near and supercritical pressure range of the vaporizing liquid was investigated by a technique wherein drops were suspended on a temperature probe and observed by means of shadowgraph movies. The forced flow of heated air was upward and uniform during the droplet lifetime.

N-heptane drop vaporization data corresponding to the range of conditions, air temperature 100-300° F, air pressure 1.5-100 atm abs, drop Reynolds number 150-600, and initial drop diameter 1275-2025 microns were obtained. These data constituted the low ambient gas temperature ($T_\infty/T_c < 0.8$) and high pressure ($0 < P/P_c < 3.7$) range for n-heptane which has a critical temperature of 312° F and a critical pressure of 27 atm abs.

Chlorotrifluoromethane (Freon 13) drop vaporization data corresponding to the range of conditions, air temperature 100-300° F, air pressure 29-68 atm abs, drop Reynolds number 250-450, and initial drop diameter 980-1200 microns, were acquired. The Fr-13, which has a critical temperature of 84° F and a critical pressure of 38.2 atm abs, results are in the range of moderate gas temperature ($1 < T_\infty/T_c < 1.5$) and high pressure ($0.75 < P/P_c < 1.75$).

Vaporization rates and drop plateau temperatures predicted by the application of existing empirical heat and mass transfer correlations were compared with measured values for individual droplet histories. The calculations accounted for high pressure vapor-liquid phase equilibrium, enthalpy of vaporization at high pressures, drop surface regression, and high mass transfer rate disruption of predicted heat and mass transfer rates. Calculations with these high pressure corrections produced agreement with the measured values to within the estimated comparison uncertainty range of $\pm$ 13^{o} F for plateau temperature and $\pm$ 25% on mass transfer rate for all data except that in the moderate ambient gas temperature range and reduced pressures above 1.25 where the calculations underestimated mass transfer rates by more than 25%. Calculations with low pressure assumptions gave good predictions of drop plateau temperatures over the entire range but underestimated mass transfer rates considerably at gas pressures above 5 atm abs.

A departure from the commonly observed drop temperature history phenomenon wherein the temperature rapidly approaches a plateau value and remains there until vaporization is practically complete was observed at moderate gas temperatures and reduced pressures greater than 1.5. This new vaporization regime which is identified by a

steadily increasing drop temperature was successfully correlated with the drop interface gas mixture critical state in the range of reduced gas pressure of 1.5-1.8 with respect to the critical pressure of Freon-13.

ACKNOWLEDGMENTS

This work was performed as one project under NASA grant Number NsG-601. The grant was administered by Mr. Paul R. Wieber of NASA Lewis Research Center, and the principal investigators were Professors G. L. Borman, O. A. Uyehara and P. S. Myers of the University of Wisconsin Mechanical Engineering Department.

Acknowledgment is given to the Wisconsin Alumni Research Foundation (WARF) for their support in the form of salary for summer semester, 1969.

The author wishes to extend his appreciation to his advisor, Professor G. L. Borman, whose encouragement and sound technical advice contributed significantly to this work.

Jaime A. Ricart, a graduate student, designed, procured and supervised the fabrication of the large, pressure-containing components of the apparatus. Lee D. Alexander, another graduate student, contributed extensively in the provision of services and instrumentation, probe fabrication, and initial performance testing for the apparatus. Helpful assistance in the form of data analysis was given by David Wantz, an undergraduate.

The helpful suggestions, high quality shop work and general openly cooperative attitudes of the many graduate students and university support personnel with whom the author had contact are greatly appreciated.

Special thanks go to my wife, Meredith, for her editing and typing assistance with this manuscript as well as her constant encouragement, sacrifices and emotional support.

TABLE OF CONTENTS

LIST OF FIGURES

LIST OF TABLES

NOMENCLATURE

A	drop surface area, $in.^2$
a	constant in Eq. (2.29), $cm^3/gm\text{-}mole$
B	$(y_0 - y_\infty)/(1 - y_\infty)$, dimensionless
b	constant in Eq. (2.29), $cm^3/gm\text{-}mole\text{-}^oK$; circulation parameter defined in Eq. (2.1), dimensionless
C	constant in Eq. (4.11), $in.\text{-}atm\text{-}min/ft^3\text{-}sec$
C_p	specific heat, $BTU/lb_m\text{-}^oR$
D	drop diameter, in.
D_{ch}	drop mean chord length defined by Eq. (4.5), in.
$\mathcal{D}_{AB}$	binary diffusivity, $in.^2/sec$
f	fugacity, atm
Gr	Grashof number = $D^3\rho^2\beta(T_\infty - T_L)/\mu^2$, dimensionless
Gr_{AB}	Grashof number due to concentration difference = $D^3\rho^2\zeta\, y_{Ao}/\mu^2$, dimensionless
$(H^*\text{-}H)$	liquid enthalpy deviation at 25^o C, BTU/lb_m
h	heat transfer coefficient, $BTU/sec\text{-}in.^2\text{-}^oR$; drop segment height, in.
K	phase equilibrium constant defined by Eq. (2.24), dimensionless
K_i	scale factors, various dimensions
k	film thermal conductivity, $BTU/sec\text{-}in.\text{-}^oR$
k_x	mass transfer coefficient, $moles/in.^2\text{-}sec$
$k^\#$	ratio of high to low pressure thermal conductivities, dimensionless
M	molecular weight, $lb_m/mole$

m	drop mass, lb_m
N	molar flux, moles/in.^{2}-sec
N_R	ratio of fluxes defined by Eq. (2.3), dimensionless
Nu	Nusselt number defined by Eq. (2.14), dimensionless
Nu_{AB}	Sherwood number defined by Eq. (2.15), dimensionless
Nu_0	Nusselt number for Prandtl number = 0, dimensionless
Nu_∞	Nusselt number for Prandtl number = ∞, dimensionless
P	pressure, atm
Pr	Prandtl number = $C_p\mu/k$, dimensionless
P_r	reduced pressure = P/P_c, dimensionless
R	result, various units; gas constant, cal/gm-mole-^oR
Re	Reynolds number = $\rho uD/\mu$, dimensionless
R_{AB}	mass transfer flux ratio defined by Eq. (2.8), dimensionless
r	tube radius, in.
Sc	Schmidt number = $\mu/\rho\mathcal{D}_{AB}$, dimensionless
T	temperature, ^oR
T_r	reduced temperature = T/T_c, dimensionless
u	air velocity, in./sec
V	molal volume, cm^3/gm-mole; drop volume, in.^{3}; total measured gas flow volume, ft^3
V_ω	constant in Eq. (2.28), cm^3/gm-mole
v	molal liquid volume, cm^3/gm-mole
v_{tc}	thermocouple potential, mv
$\mathcal{V}$	gas meter measured flow rate, ft^3/min

W	drop weight, lb_m
We	Weber number defined by Eq. (4.1), dimensionless
x	liquid mole fraction or independent variable, dimensionless
y	gas mole fraction, dimensionless
z	rate factor for heat transfer defined by Eq. (2.7), dimensionless
β	thermal coefficient of volumetric expansion, $1/^{\circ}R$
γ	activity coefficient, dimensionless
δ	solubility factor, $(cal/cm^3)^{1/2}$
ζ	concentration coefficient of volumetric expansion, dimensionless
$\Delta\theta$	drop lifetime, sec
θ	time, sec; surface fraction defined by Eq. (2.22), dimensionless
λ	enthalpy of vaporization, BTU/lb_m
μ	viscosity, $lb_m/in.\text{-}sec$
ϕ	vapor phase fugacity coefficient or empirical factor in Eq. (4.2), dimensionless
ϕ_{ij}	weighting factor defined by Eq. (2.36), dimensionless
ρ	density, $lb_m/in.^3$
σ	drop surface tension, $lb_f/in.$
σ_D	standard deviation of drop diameter measurement, in.

Subscripts

A	species A, usually vapor
B	species B, usually air
c	continuous phase
calc	determined by calculation

conv	convergence
d	dispersed phase
exp	experimentally determined
i	species i
L	liquid or drop
m	mixture
n	index
sat	saturated
total	total
0	drop-film interface
∞	free stream

Superscripts

$\cdot$	at high mass transfer rates
$\bar{}$	average film quantity or uncertainty interval of barred quantity
0	ideal
*	at 25° C
lp	atmospheric pressure value

INTRODUCTION

The importance of droplet vaporization to the combustion process in diesel, jet and rocket engines has been realized for many years. Early studies of this phenomenon, both in chemical engineering and combustion, were confined to low pressure conditions. Several recent articles review the data accumulated since World War II for heat and mass transfer from single drops (19, 25, 50).*

In the last decade improved performance in combustion devices has led to ever higher operating pressure levels which are now approaching the critical pressure range of fuels. In addition, oscillatory combustion in liquid-fueled rocket engines creates large amplitude variations in the instantaneous chamber pressure causing droplets to experience much higher than normal design pressures.

The ability to predict both steady state and transient performance of engines is dependent in part on the successful application of a droplet vaporization model in the high pressure region. The application of empirical heat and mass transfer coefficients based upon boundary layer average properties led to a film theory vaporization model which has been successfully correlated with data at atmospheric pressure (6, 44). Thus, strong motivation exists for adapting the film theory model for the high pressure region and testing it with the results of high pressure vaporization experiments.

*Numbers in parenthesis refer to references listed alphabetically by first author.

At atmospheric pressure both experiment and theory show that a drop which is suddenly exposed to a high temperature inert gas environment will first show a gradual rise in droplet temperature followed by a period of constant droplet temperature. The rising temperature portion of the history is referred to as the unsteady or "heating up" period and the constant temperature portion as the steady state period. The steady state temperature will be referred to here as the plateau temperature or "wet bulb" temperature. During the unsteady state the droplet temperature rise causes the mole fraction of droplet vapor at the droplet surface to increase, thus providing a larger driving potential for mass transfer. At the same time the decreasing temperature difference between droplet and ambient gas causes a decrease in the driving potential for heat transfer. During the unsteady period some of the energy reaching the droplet surface goes into vaporizing the liquid, and the excess goes into sensible heating of the droplet liquid. From previous studies it has been shown that because of internal circulation within the drop, the droplet temperature is essentially uniform being then only a function of time. At steady state all of the heat transfer reaching the surface goes into mass vaporization and the droplet temperature remains constant. The ratio of heat to mass transfer coefficients is essentially independent of rela-

tive gas velocity and droplet size. Thus, for a given liquid and given ambient gas, the plateau temperature depends only on ambient gas temperature and pressure.

Turning to the effects of high ambient pressure on the vaporization process, one must first recognize the existence of critical points for binary mixtures. At high pressures the ambient gas dissolves in the drop forming a mixture in the liquid phase. A critical point for a two component mixture of a given composition is the single point on the line bounding the two-phase region of a pressure-temperature diagram where the phases become indistinguishable (23). The locus of these critical points for all compositions is called the critical mixing line. If one assumes thermodynamic equilibrium at the droplet surface, it is intuitive that at sufficiently high ambient temperatures and pressures the mixture at the surface may reach or exceed the critical mixing point state. Such states usually occur for ambient pressures above that of the pure liquid critical pressure and mixture temperatures well below the critical temperature of the pure liquid.

For droplet histories where the mixture critical point is approached, the thermodynamic and transport properties become increasingly dependent on pressure. In particular, the mole fraction of droplet vapor at the droplet surface and the enthalpy of vaporization must be calculated to include the influence of total pressure. The enthalpy of vaporization

(latent heat) vanishes at the mixture critical point. Thus, if the droplet interface conditions reach the mixture critical point during the unsteady portion of the history, all subsequent heat transfer to the drop will result in sensible droplet heating. For such conditions no plateau temperature will exist, and the droplet temperature history will be completely unsteady.

Recently two investigations of high pressure droplet vaporization have been undertaken at the University of Wisconsin under NASA sponsorship. In the first, Manrique performed detailed calculations of the vaporization of carbon dioxide droplets in a high pressure nitrogen atmosphere (35). Both steady state and transient vaporization models were investigated as well as the case of pressure fluctuation. In the second investigation, which is reported here, a high pressure chamber which can achieve air temperatures up to 300° F and pressures up to 100 atm was built to study suspended droplets. An upward flowing stream of heated, high pressure air vaporizes the droplet. The experiment gives droplet temperature histories and two-dimensional size histories via motion picture records.

Water, n-heptane, and Freon-13 (Fr-13) data were obtained. The apparatus was tested with water drops. The n-heptane experimentation provided data in the region of supercritical pressure but at temperatures below the near critical range and below the ignition point. Fr-13,

chlorotrifluoromethane, was selected because its low critical temperature, 84° F, gave promise of achieving a critical state during vaporization in the rig, and its high thermal stability with air avoided consideration of chemical reactions or combustion. In addition, Fr-13 is relatively non-toxic and has a moderate critical pressure of 38.2 atm.

The high pressure data are compared with calculations based on a film theory that has been modified for application in the high pressure region. The transition from quasi-steady to unsteady drop temperature histories is examined, and its relation to the critical state of the gas mixture in the boundary layer is demonstrated.

The combustion vaporization literature is reviewed in Chapter I. In Chapter II the film theory which was developed with low pressure assumptions (17) is presented, discussed and modified for high pressure application. Chapter III contains a description of the experimental apparatus and techniques.

The experimental problems encountered and the data reduction techniques employed are discussed in Chapter IV. The experimental results are presented in Chapter V where they are compared with calculated values. Finally, in Chapter VI the conclusions of the study and recommendations for future work in this research area are given.

I. REVIEW OF THE LITERATURE

Droplet vaporization has been an active area of combustion research since the early 1950's. The earlier work which is briefly summarized below was concentrated in the low pressure region.

As time has progressed, attention has been increasingly focused on the high pressure region. In 1959 Spalding (53) proposed a droplet burning rate model for high pressures. Recent experimental results of burning droplets first gave evidence of a new mechanism of vaporization at gas pressures exceeding the critical pressure of the vaporizing liquid (18). Although the mechanism was recognized by the experimenters and correctly associated with the critical region of the vaporizing media, a firm physical basis has only very recently been tendered. These interesting developments are reviewed in this chapter.

Experimental and Theoretical Results at Atmospheric Pressure

A wealth of data on the vaporization of suspended droplets at atmospheric pressure was obtained by Priem and his co-workers (44). The droplet temperatures and size histories data covered a range of conditions: air temperatures of 680-1430^{o} R, air velocity of 27-228 in./sec, initial drop diameter of 490-2180 microns, and 10 paraffin fuels. They compared their data with histories calculated with quasi-

steady low pressure film theory.

The film theory used by Priem was first developed by El-Wakil, Uyehara and Myers (17). The Ranz-Marshall correlations for heat and mass transfer provided the empirical heat and mass transfer coefficients. The coefficients as applied include corrections for unidirectional molal diffusion and the effect of mass transfer on heat transfer. Ideal properties such as the pure liquid latent heat of vaporization and vapor pressure relationship were assumed.

In applying the low pressure film theory model to his data, Priem found that temperature histories agreed to within 10° F and mass transfer rates within 20%. The agreement was considered to be within experimental accuracy.

Experimental Results at High Pressures

The earliest vaporization data in forced flow at pressures above atmospheric of which the author knows is that of Ingebo (26). Ingebo's data included four pure liquids vaporizing in air at pressures of 0.2-2 atm abs and methanol vaporizing in air, argon, helium, and carbon dioxide at atmospheric pressure. A steady state porous sphere arrangement was utilized in the study. He found that the film temperature difference and mass vaporization rate both decreased with increasing pressure, other conditions remaining constant.

Hall and Diederichsen (21) using an apparatus, which

was built for the study of suspended burning drops, obtained evaporation lifetime measurements of water drops in air heated by a gas flame or a carbon arc igniter. The pressure range of 1-20 atm was covered. They found that the rate of vaporization depended on the second power of drop radius and that the evaporation lifetime of a given diameter drop decreased with increased pressure.

Petrazhitskiy (42) reported the results of an extensive experimental investigation of droplet vaporization at high pressures. He obtained liquid plateau temperatures and vaporization constant measurements, $\frac{d(D^2)}{dt}$, for water, 96% ethyl alcohol and kerosene drops suspended and vaporizing in flowing, heated air. The air pressure was varied from 11-41 atm in each test except for water where the range was 11-60 atm. A Reynolds number range of 100-500 was covered in the tests. His quasi-steady results with measured flow conditions were given with neither comparisons to theory nor developed correlations.

In their combustion tests of aniline droplets at high pressures, Brzustowski and Natarajan (7) performed some vaporization experiments. They vaporized supported aniline droplets in a mixture of 90% nitrogen and 10% oxygen. The drops were located in a closed chamber and in one series of tests were heated by carbon electrodes and in the other by the combustion of a solid propellant strand. The maximum temperature near the drop and the evaporation constant

were determined. The test chamber pressure was varied from 100 to 800 psig. They concluded that the evaporation mechanism of aniline into a gas above its critical pressure but below its critical temperature is similar to its mechanism at low pressure.

A fifth series of high pressure vaporization experiments was performed by Torda and Matlosz (55). They obtained temperature and size histories of n-pentane droplets injected into and supported in a heated and pressurized test chamber containing nitrogen. Data covering a range of pressure of 200-1400 psi at a fixed gas environment temperature of 850° R were reported. Presumably, the mode of heat and mass transfer was a combination of free convection and simple diffusion. Their attempts at simulating the experimental results with calculations were not particularly successful.

Borman et al. (6) reported the results of suspended hexane, decane, and hexadecane drops vaporizing in air at various temperatures and pressures from 1 to 5 atm abs with measured flow conditions. The experimental drop temperatures and mass transfer rates compared favorably with computed results over the rang e of temperatures and pressures investigated.

Of all the high pressure vaporization experiments summarized above, only the work of Brzustowski and Natarajan and that of Torda and Matlosz extended into the supercritical

pressure range. Of these two experiments, apparently only Torda and Matlosz observed steadily increasing droplet temperatures which did not attain the plateau which is characteristic of low pressure drop temperature histories. All six of the vaporization experiments summarized above utilized supported drops in a 1 g gravity field.

NASA Lewis supported work is in progress at Illinois Institute of Technology and University of Wisconsin on free-falling drops vaporizing in high pressure gases. The principal investigators of these projects are Professor T. P. Torda at IIT and Professors P. S. Myers, O. A. Uyehara and G. L. Borman at Wisconsin.

A few studies of burning drops at high pressures have been reported. In addition to their preliminary vaporization experiments previously discussed, Brzustowski and Natarajan (7) carried out burning experiments with suspended aniline drops at pressures up to slightly above the critical pressure of aniline. They inferred from their motion picture data that a different regime of burning occurred in the supercritical pressure range. Hall and Diederichsen (21) obtained burning lifetimes of suspended kerosene, tetralin, decane, furfuryl alcohol and amyl acetate drops at elevated pressures but not into the near or supercritical pressure region.

Probably the most interesting high pressure droplet burning experiments, at least from the standpoint of vapori-

zation mechanisms, are those of Faeth, Dominicis and Olson (18). They measured the temperature and size history of suspended burning droplets in a zero g pressurized test chamber. In a series of tests of n-decane burning at increasing air pressures, the temperature histories showed a decreasing tendency toward a plateau attainment, and at a reduced pressure of about 1.6, only a slight inflection point in the temperature trace occurred. At the highest reduced pressure reported, 3.5, the droplet temperature increased steadily. They also noted the tendency for combustion lifetime to increase with pressure at pressures somewhat above the critical pressure.

Theoretical Results at High Pressures

Spalding (53) raised doubts about the application of the low pressure quasi-steady burning theory to predict droplet burning times at high pressures. In the high pressure region he abandoned the quasi-steady theory wherein the burning rate was vaporization rate limited. Spalding's theory considered the fuel to be a point source and utilized a first order chemical reaction as the outer boundary condition. He obtained a penetration theory result for the transient constant property case. As an initial condition, he assumed that all of the fuel was introduced instantaneously. His theory which is inapplicable to purely vaporization phenomena because of the outer boundary

condition is interesting nevertheless since it avoids the problems of transition to the critical state and the corresponding vanishing of the enthalpy of vaporization. The point source assumption has recently been relaxed by Rosner (49).

Wieber (57) investigated the attainment of droplet critical state conditions in rocket chambers. The results of his quasi-steady film theory calculations indicated that oxygen and heptane droplets would approach their critical temperature at reduced pressures of approximately one and two, respectively. Ambient conditions of 5000° R gas temperature, 800 ft/sec final gas velocity, initial conditions of 10-1000 micron drop size and 80 ft/sec injection velocity were considered. Furthermore, the trends of his results showed that the fractional droplet mass vaporized before attainment of critical temperature decreased with increasing pressure.

More recently, Manrique and Borman (36) investigated high pressure vaporization. They performed detailed numerical calculations for the steady-state vaporization of carbon dioxide drops in a nitrogen environment. For the case of a spherically symmetric boundary layer (i.e., no free or forced convection heat and mass transfer), they included the effects of thermodynamic non-idealities, property variation through the boundary layer and high pressure liquid-vapor equilibrium.

The most significant result of Manrique's and Borman's analysis is that at sufficiently high pressures they found steady state conditions cannot be obtained. Prior to their work it had been realized that if the liquid component could reach its critical temperature, a different regime of vaporization would be expected. However, they focused attention on the state of the gas mixture at the liquid-vapor interface. They pointed out the fact that this mixture could reach its critical state at a temperature below the pure liquid critical temperature but above the pure liquid critical pressure. This criterion determines whether a new regime is obtained. It would be expected that probably a third regime of droplet vaporization would be reached when the droplet temperature reached its critical temperature and a puff of supercritical fluid resulted.

Manrique (35) has extended his work to the unsteady case and has made comparisons with quasi-steady film theory models. Generally, he has found that the simpler theories give a fair prediction of vaporization lifetimes but give fairly large errors in predicting temperature and mass histories. Under some conditions of pressure and temperature, he found that film theory gives physically unrealistic steady state results. In the high ambient density region (high pressure and low temperature), film theory corrected for high pressure produced better results than the low pressure model. However, the low pressure model gave better

predictions than the high pressure film theory model in the high temperature, high pressure region although neither model gave close agreement with the exact calculations in this region.

In view of the recent work, two regions of droplet vaporization behavior were expected: 1) subcritical pressure range exhibiting a quasi-steady drop temperature history; 2) supercritical pressure range exhibiting a completely unsteady drop temperature history and characterized by a supercritical gas mixture in the boundary layer. The droplet temperature history could be expected to exhibit the classical plateau only in the low pressure regime. Departures from this form would indicate a transition to the second regime.

Manrique's calculations suggest that film theory modified for high pressures may be expected to give approximate results at pressures in the near critical region. In addition, a correlation between transition from the first to the second regime and the gas mixture critical point should be obtainable. These predictions and modifications to the low pressure film theory are discussed in the following chapter.

II. DISCUSSION OF THE THEORY

In this chapter a physical picture of droplet vaporization is presented. This is followed by the development of the film theory equations. The topics of gas mixture critical state calculations, property non-idealities due to high pressure effects and spatial variations through the boundary layer are discussed in relation to the film theory corrections required at near critical conditions.

Physical Description of Droplet Vaporization

The process of droplet vaporization can be idealized as a boundary layer problem with simultaneous heat, mass and momentum transfer between a stationary sphere and a steady flow of gas.

Boundary layer development times equal to droplet radius divided by gas velocity were found to be short compared to droplet lifetimes, thus allowing the steady state idealization (9).

Contrary to the usual boundary condition in rigid sphere cases, i.e., zero velocity in the zimuthal direction at the sphere-boundary layer interface, a finite velocity results from droplet internal circulation effects. Winnikow and Chao (58) in their studies of liquid-liquid

systems have correlated their observed reduction in measured drag coefficients with an internal circulation parameter, b, which involves the viscosities of the dispersed (d) and continuous (c) phases.

$$b = \left[2 + 3\left(\frac{\mu_d}{\mu_c} \right) \right] \left[1 + \left(\frac{\rho_d \mu_d}{\rho_c \mu_c} \right)^{1/2} \right]^{-1} \qquad (2.1)$$

They also observed an increase in the angle of the boundary layer separation point and its dependence on their circulation parameter. Predictions of the effects of internal circulation upon drag coefficients in any systems other than highly purified fluids are, however, very questionable because of the large dependence of interfacial behavior on small impurities.

When the drop Weber number, the ratio of drag to surface tension force, reaches a critical value, droplet oscillations begin. If no stabilizing trends such as radius reduction due to vaporization or relative velocity reduction due to droplet momentum gain are established, droplet breakup in the case of unsupported drops or loss of droplet support in the case of supported drops occurs after a time lag. Results of critical Weber number experiments vary, but a typical value is 4 where the Weber number is based upon diameter (58). This criterion, although providing insight, does not strictly apply to supported droplet behavior. In

addition to the drag and circumferential surface tension force on a free drop, a supported drop has a surface tension force at the support point. The latter force accomodates itself to balance the weight and drag force and can, in fact, have a resultant force either in the direction of the flow or in the opposite sense. Increases in droplet temperature and pressure will increase droplet Weber number through the effect of decreasing surface tension thereby increasing the possibility of oscillation.

The conditions of the experiment and, in general, those existing in sprays, place the flow in the laminar regime. It would be possible to calculate the heat and mass transfer rates by solving the boundary layer equations except for the effects of flow separation. For average values of heat and mass transfer coefficients, one can resort to semi-empirical correlations such as those of Ranz and Marshall (46). The data synthesized with the Ranz-Marshall correlation were obtained under the conditions of low mass transfer rates, and the heat transfer results were independent of mass transfer. These correlations can be utilized with appropriate correction (4) for simultaneous heat and mass transfer at high mass transfer rates.

Normally, only two parameters, Reynolds number and Schmidt number, are used to correlate the dimensionless mass transfer coefficient, $Nu_{AB}(Re,Sc)$. However, at high mass transfer rates in fluid-fluid systems, one would expect

a more complicated Sherwood number dependence: Nu_{AB} = f(Re, Sc, B, b). The B parameter accounts for the effects of high mass transfer rates (1). The effects of internal circulation would be accounted for by the b parameter given by Chao and repeated in Eq. (2.1).

Film Theory

Film theory applies dimensionless transfer coefficients based on average film properties to compute heat and mass transfer rates. In this section the film theory differential equations for droplet temperature, T_L, and mass, m, as a function of time, θ, are derived under the assumptions of a quasi-steady model. Then the steady state result is developed as a special case. Physically, the steady state result corresponds to a simulated sphere experiment where the vaporization rate is balanced by the liquid feed rate.

As a preliminary the definition of the mass transfer coefficient, k_x, is given by Eq. (2.2). Its definition is based upon the molar flux of species A with respect to the molar average velocity. This convention, which is in accordance with Bird, Stewart and Lightfoot (4), has the advantage that k_x has a simple dependence upon concentration level and mass transfer rate. In other words, k_x gives the mass transfer coefficient for mass transfer alone; the bulk-flow term is subtracted.

$$k_x^{\cdot} = \frac{N_{Ao} - y_{Ao}(N_{Ao} + N_{Bo})}{y_{Ao} - y_{A\infty}} \qquad (2.2)$$

N_{Ao}, N_{Bo} and y_{Ao} are the molar flux of A, the molar flux of B and the mole fraction of A at the droplet surface and $y_{A\infty}$ is the mole fraction of A in the free stream. If the ratio of fluxes, N_R, is defined as

$$N_R = N_{Bo}/N_{Ao}, \tag{2.3}$$

Eq. (2.2) becomes

$$k_x^{\bullet} = \frac{N_{Ao}[1 - y_{Ao}(1 + N_R)]}{y_{Ao} - y_{A\infty}} \tag{2.4}$$

The superscript black dot ($\bullet$) denotes that the transfer coefficients depend on mass transfer rate. The film theory summarized in paragraph 21.5 of Ref. (4)* was selected to relate the coefficients $h^{\bullet}$ and $k_x^{\bullet}$ to the transfer coefficients, h and k_x, which apply at low mass transfer rates.

The film theory corrections were obtained by assuming laminar flow in plane geometry. The fluxes, in terms of the boundary layer thicknesses, resulted from integrating the equations of change assuming constant properties. Then the boundary layer thicknesses were evaluated in terms of the uncorrected transfer coefficients. There are two major assumptions inherent in the derivation (4) which may have implications for application to high pressure droplet evaporation. The first and probably most serious is the

*This "film theory" uses a simplified unidirectional transport model to predict the variation of the transfer coefficients with mass transfer rate, and it should not be confused with the use of the term in the present work.

assumption of constant properties across the boundary layer, particularly constant heat capacity and the neglect of heat of mixing between the vapor and continuous gas phase. The second questionable assumption is that the film thickness is unaffected by high mass transfer rates.

The results of these film theory correction are given by

$$h^{\bullet} = h \frac{z}{e^{z} - 1} \tag{2.5}$$

$$k_x^{\bullet} = k_x \frac{\ln(1 + R_{AB})}{R_{AB}} \tag{2.6}$$

where

$$z = \frac{N_{Ao}(C_{pA} + N_R C_{pB})}{h} \tag{2.7}$$

$$R_{AB} = \frac{y_{Ao} - y_{A\infty}}{\frac{1}{1 + N_R} - y_{Ao}} \tag{2.8}$$

and C_{pA} is the vapor specific heat of species A. The parameter z is equivalent to the "rate factor" for heat transfer and R_{AB} to the mass transfer "flux ratio" cited in Ref. (4).

With these preliminaries in mind, the quasi-steady energy equations can be written for a vaporizing drop. There are a number of assumptions implicit in this development.

1. The drop temperature at any moment is uniform.

2. Viscous dissipation is negligible.
3. Work done by pressure or gravitational forces is negligible.
4. The energy transferred to the drop by radiation is negligible.
5. Thermo-diffusion and diffusion-thermo effects are negligible.
6. Steady state heat and mass transfer correlations are applicable.

The following word equation corresponds to the terms in the energy balance, Eq. (2.9)

$$\left[\begin{array}{l}\text{Energy}\\ \text{stored}\\ \text{in drop}\end{array}\right] = \left[\begin{array}{l}\text{Energy transferred}\\ \text{to drop by}\\ \text{convection}\end{array}\right] - \left[\begin{array}{l}\text{Energy carried}\\ \text{away from drop}\\ \text{by mass transfer}\end{array}\right]$$

$$\frac{\pi}{6} D^3 \rho_L C_{pL} \frac{dT_L}{d\theta} = \pi D^2 h^{\bullet}(T_\infty - T_L) - \lambda \frac{dm}{d\theta} \qquad (2.9)$$

where ρ_L and C_{pL} are the density and specific heat of the drop liquid, T_L and T_∞ are temperatures of the drop and free stream gas, λ is the heat of vaporization of the liquid, m is the droplet mass and θ is the independent variable time. The vaporization rate is given by Eq. (2.10) which follows from Eq. (2.4)

$$\frac{dm}{d\theta} = \frac{\pi D^2 M_A k_x^{\bullet} (y_{Ao} - y_{A\infty})}{1 - y_{Ao}(1 + N_R)} \qquad (2.10)$$

where D, the droplet diameter, is defined by Eq. (2.11)

$$D = \left(\frac{6m}{\pi \rho_L}\right)^{1/3} \tag{2.11}$$

The mass transfer coefficients independent of mass transfer rate are determined by the Ranz-Marshall correlations (46):

$$Nu = 2 + 0.6\ Re^{1/2}\ Pr^{1/3} \tag{2.12}$$

$$Nu_{AB} = 2 + 0.6\ Re^{1/2}\ Sc^{1/3} \tag{2.13}$$

where Reynolds, Prandtl and Schmidt numbers are designated by Re, Pr and Sc, respectively. The Nusselt, Nu, and Sherwood, Nu_{AB}, numbers are defined by Eqs. (2.14) and (2.15).

$$Nu = \frac{hD}{k} \tag{2.14}$$

$$Nu_{AB} = \frac{k_x\ D\bar{M}}{\rho \mathcal{D}_{AB}} \tag{2.15}$$

Average film properties of thermal conductivity (k), molecular weight ($\bar{M}$), density (ρ) and binary diffusivity ($\mathcal{D}_{AB}$) are used.

Combining Eqs. (2.4), (2.10) and (2.15), the result for drop mass is obtained,

$$\frac{dm}{d\theta} = \frac{\pi\ D M_A\ \rho \mathcal{D}_{AB}\ \ Nu_{AB}}{\bar{M}}\ \ln(1 + R_{AB}) \tag{2.16}$$

Similarly, Eqs. (2.5), (2.7), (2.9) and (2.14) yield Eq. (2.17) for the drop temperature time derivative,

$$\frac{dT_L}{d\theta} = \frac{6}{\rho_L C_{pL} D^2}\left[\frac{k\ Nu\ z(T_\infty - T_L)}{e^z - 1} - \frac{\lambda}{\pi D}\frac{dm}{d\theta}\right] \qquad (2.17)$$

Three auxiliary equations are required.

$$z = \frac{\rho \mathcal{D}_{AB}\ Nu_{AB}\ M_A}{k\ \bar{M}\ Nu}\ \frac{\ln(1 + R_{AB})}{(1 + N_R)}\ (C_{pA} + N_R\ C_{pB}) \qquad (2.18)$$

$$D = \left(\frac{6m}{\pi \rho_L}\right)^{1/3} \qquad (2.19)$$

$$N_R = -\frac{P\ M_A\ (1 - y_{Ao})}{\rho_L\ R T_L} \qquad (2.20)$$

Eq. (2.20) is derived by assuming that the molar flux of species B is equal to the concentration of B at the drop interface times the velocity of liquid species A.

Eqs. (2.16) and (2.17) constitute a coupled set of first order differential equations. The equations, with their initial conditions, were solved numerically by a fourth order Runge-Kutta method which has an automatic step size adjustment (56). It takes less than one minute to solve a three second drop history on the UNIVAC 1108 computer. The film properties ρ, $\mathcal{D}_{AB}$, μ, k, C_p, and $\bar{M}$ are determined at average film temperature and composition

values, and the Nusselt and Sherwood numbers are based upon average film values. The gas mixture component specific heats, C_{pA} and C_{pB}, are evaluated at the average film temperature. The properties ρ_L and C_{pL} refer to the liquid at the liquid temperature.

The steady state result is obtained by setting the derivative in Eq. (2.17) to zero. After substitution for z and rearrangement,

$$T_\infty - T_L = \frac{\lambda\ (e^z - 1)}{C_{pA} + N_R\ C_{pB}} \tag{2.21}$$

The equation for the steady state mass transfer rate is given by Eq. (2.16). The terms on the right hand side of the equation are functions of T_∞ and T_L, so it is necessary to solve by iteration. Since the right side is less sensitive to T_∞, it was found most convenient to treat T_∞ as the dependent variable and T_L as the independent variable. A digital computer code for the IBM 1620 computer was written in FORGO language to perform steady state calculations.

Mixture Critical State Transition

In the description of the physical process of droplet vaporization, the hypothesis of a transition from a vaporization process occuring at a constant plateau temperature to a steadily increasing one was advanced. The key to this

transition is the state of the gas mixture in the film surrounding the drop at the drop-film interface. If the gas mixture at this point exceeds the critical temperature corresponding to the total pressure in the gas mixture, an unsteady droplet temperature history results. Manrique and Borman's calculations (36) illustrate this phenomenon. Consequently, an estimate of the critical mixing line for the gas mixture is necessary to predict the low limit of this regime.

A rigorous solution to this problem consists of solving the problem of thermodynamic equilibrium for the vapor-liquid interface. But in this case of the critical mixing line, one has to find the locus of the critical points of the $y_A(P, T)$ functions. Chueh and Prausnitz (13) in a recent article presented a method of estimating the critical mixing lines for non-polar binary mixtures. This method was adopted and programmed for computing the relationships for the n-heptane-air and Fr-13-air systems. A brief outline of the method is given below.

Chueh and Prausnitz proposed that the critical temperature and critical volume be computed as a quadratic function of surface fraction, θ_A,

$$\theta_A = y_A v_{cA}^{2/3} \Big/ \left(y_A v_{cA}^{2/3} + y_B v_{cB}^{2/3} \right) \qquad (2.22)$$

where

v_{ci} = critical volume of component i,

y_i = mole fraction of component i.

Parameters are introduced which are coefficients of the quadratic terms. They present correlations for these parameters which are functions of the pure component critical properties.

Because of the strongly nonlinear dependence of the critical pressure on composition, a different procedure is presented for computing the mixture critical pressure. The correlations for critical temperature and critical volume are used in conjunction with a slightly modified version of the Redlich-Kwong equation of state. They compared computed critical pressures for 36 binary systems with data and found a mean average deviation of 3.6% The average deviations of experimental and fitted critical temperatures are found to be 0.4% for 65 binary systems. Their scheme for determining the mixture critical volume was found to correlate the data for 25 systems within an average deviation of 1.9%.

Property Non-Idealities

The low pressure model departs from a realistic representation of droplet vaporization as the system pressure increases. Considerations of the critical state of the gas mixture were presented in the previous section. This

section is concerned with the variations in the properties which enter into the film theory model. High pressure non-ideal effects are treated first and are followed by a discussion of the spatial variation of properties through the boundary layer. The implications of the use of properties averaged over the film are assessed.

High Pressure Effects

The properties of the gas mixture, y_{Ao}, λ, k, C_p, $\mathcal{D}_{AB}$, μ, and ρ, all appear in the film theory results given in Eqs. (2.16) and (2.17). The first three, which are corrected in the high pressure application of the film theory, are discussed individually in subsequent parts of this section. The last four properties are used in their uncorrected form in the high pressure theory. Corrections for them were considered but discarded for various reasons.

Calculations were made for a Fr-13 drop vaporizing at high pressure within the range of experimental conditions reported in Chapter V. Then arbitrary variations in the various mixture properties were introduced, and the sensitivity of the calculated plateau temperature and instantaneous vaporization rate to these changes were assessed.

Negligible effects due to 10% variations in mixture specific heat, C_p, viscosity, μ, and density, ρ, were found. Therefore, high pressure corrections were not introduced for these properties. Since these values enter into

the dimensionless numbers which appear fractionally exponentiated in the heat and mass transfer correlations, the insensitivity is not too surprising.

However, a 10% variation in the binary diffusion coefficient, $\mathcal{D}_{AB}$, produced about a 10% change in the steady state drop-air temperature difference and a 2% change in vaporization rate. No data exists for binary diffusion coefficients in Fr-13-air mixtures. The diffusivity values used were calculated by means of a corresponding state correlation which is estimated to be accurate only within approximately 10% (25). Consequently, high pressure corrections to the binary diffusion coefficients (54) were omitted.

Droplet-Film Interface Mole Fraction

The determination of the mole fraction, y_{Ao}, at the droplet-film interface is a vapor-liquid equilibrium problem. In the case of a pure liquid drop vaporizing into a pure inert gas environment, there are two components and two phases. Designating the mole fraction in the liquid and vapor phases by x_{Ao} and y_{Ao}, respectively, of the four variable factors (y_{Ao}, x_{Ao}, P, T) there are two degrees of freedom for the system according to Gibbs Phase Rule (40).

A common and simple approach is to use the saturation pressure relationship for the vaporizing component.

$$y_{Ao} = P_{sat}/P_{total} \tag{2.23}$$

At total pressures low compared to the critical pressure of A, this usually gives a satisfactory approximation. This approximation is utilized in the low pressure film theory.

At thermodynamic equilibrium the chemical potential of any given component in all phases of a multicomponent system is identical (40). This basic approach or its equivalent of determining the mole fractions which give equivalent fugacities in the liquid and vapor phases for each component was used by Manrique and Borman (36) in their analysis of the CO_2-N_2 system. They specified the temperature and total pressure of the system and determined the fugacity of the components as a function of component mole fractions using the Redlich-Kwong equation of state for the mixture. In this manner they obtained a map of equilibrium mole fraction, y_A and x_A, for the range of atmospheric to the gas mixture critical pressure for a given temperature.

Manrique and Borman demonstrated their approach by making a satisfactory comparison with data for the CO_2-N_2 system. However, at the same time their approach is time consuming, particularly the algebra involved in obtaining simultaneous solutions to the component fugacities in both phases and satisfying species continuity in each phase.

Hougen, Watson and Ragatz (23) describe another approach. It is applicable to the region near the critical point, and was used for the n-heptane-air calculations

given in Chapter V. This convergence pressure technique has been developed for hydrocarbon mixtures and extensive charts (39) have been prepared which give the vapor liquid equilibrium ratio, K, which is a function of P_r, T_r, and the convergence pressure, P_{conv} for each hydrocarbon, nitrogen and carbon dioxide. The convergence pressure corresponds to the mixture critical pressure. Hougen, Watson and Ragatz indicated that this semi-empirical method requires judgment, but it yields generally acceptable results at pressures less than 80% of the convergence pressure.

A fourth method which was considered for use with the Fr-13-air calculations and finally selected upon the basis of tests with data is summarized below. The method is a variation of the one outlined by Reid and Sherwood (47) for calculating phase-equilibrium constants, K_i,

$$K_i = y_i/x_i \tag{2.24}$$

where the subscript o denoting the drop-film interface is dropped for convenience.

$$K_i = \gamma_{iL}(f^o_{iL}/P)/\phi_i \tag{2.25}$$

where

f^o_{iL} is the fugacity of pure i at T and P as a liquid. If $P > P_{sat}$, the saturation pressure at T, f^o_{iL} is estimated from the fugacity of i saturated at T using the Poynting correction. If $P < P_{sat}$, the saturated value of f^o_{iL}

corresponding to T is used. For cases where $T > T_c$, usually the case for nitrogen and air, the vapor pressure relationship is extrapolated to a fictitious value of P_{sat}.

The vapor phase fugacity coefficient for component i in the gas mixture, ϕ_i, is determined from the Redlich-Kwong equation of state as shown by Chao and Seeder (10).

The liquid mixture is treated as a regular solution and the activity coefficient, γ_{iL}, is calculated by the Scatchard-Hildebrand equation

$$\ln \gamma_{iL} = V_i^* (\delta_i - \bar{\delta})^2/RT \tag{2.26}$$

where

$$\bar{\delta} = \sum_i x_i V_i^* \delta_i / \sum_i x_i V_i^* \tag{2.27}$$

and

$$V_i^* = \left(V_\omega\right)_i (5.7 + 3 T_{ri}) \tag{2.28}$$

The molar liquid volume, V_i^*, and the solubility parameter, δ_i, have been treated as empirical constants by various authors. Cavett (29) reviewed the literature and selected and tabulated values for many components. Cavett's values for N_2, O_2, CO_2, and n-heptane were utilized in test calculations which are summarized below.

In the case of Fr-12 and Fr-13 which were not listed

by Cavett, V_i^* (25° C) was determined by extrapolating the equation given by Prausnitz et al. (43).

$$V_i = a + bT \tag{2.29}$$

Two values of the molal liquid volume at temperatures removed from the critical were substituted in order to evaluate the constant in Eq. (2.29). Then $(V_\omega)_i$ was derived from Eq. (2.28) by substituting the 25° C value of V_i^*.

Cavett's method (8) of determining δ_i was applied to give

$$\delta_i = \left[\frac{(H^* - H) - RT}{V^*} + P\right]^{1/2} \tag{2.30}$$

where $(H^* - H)$ is the enthalpy derivation for the liquid at 25° C, V^* is the V_i^* (25° C) previously found and P is the saturation value at 25° C. Table I contains the constants derived for Fr-12 and Fr-13.

Table I

Calculated Constants for Liquid Phase Activity Coefficients

Component i	$(V_\omega)_i \left(\frac{cm^3}{gm\ mole}\right)$	$\delta_i \left(\frac{cal}{cm^3}\right)^{1/2}$
Fr-12	11.53	6.96
Fr-13	11.86	4.19
Air	2.60	2.97

An iterative procedure was developed to calculate the

equilibrium mole fractions for a two component mixture at a fixed temperature and pressure. Initially, K_A was assumed to be equal to P_{sat}/P, $K_B = \infty$, and $x_A = 1$. Then

$$x_B = (1 - x_A K_A)/K_B \tag{2.31}$$

$$x_A = 1 - x_B \tag{2.32}$$

$$y_A = x_A K_A \tag{2.33}$$

$$y_B = 1 - y_A \tag{2.34}$$

These four equations were solved and K_A and K_B were calculated from Eq. (2.25). These calculated values were used as a second estimate and the procedure repeated until the fractional change in K_A between successive iteration was less than 0.005.

In order to avoid the difficulties of treating a three component mixture, air was assumed to be a single component. The constants in the liquid phase activity coefficient calculation were determined by mole fraction weighting of N_2 and O_2 values for the air composition. They are given in Table I.

The results of a comparison of calculated and measured mole fractions for the CO_2-N_2 system are shown on Fig. 1 (60). The calculated gas phase values agree within 15% at

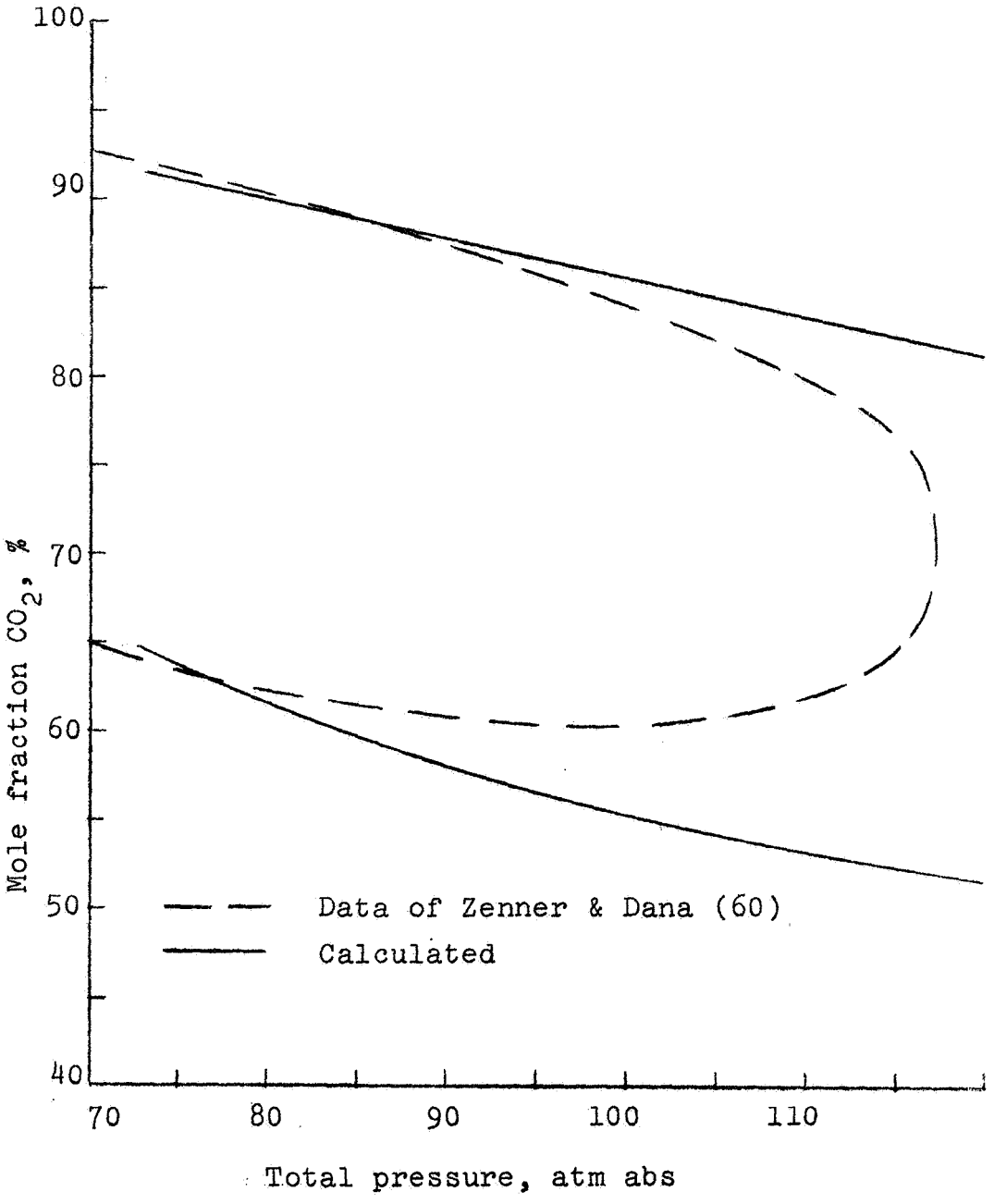

Fig. 1. Vapor-Liquid Equilibrium Relations for Carbon Dioxide-Nitrogen Mixtures at 0° C

$P_r \sim 1.5$ and $T_r = 0.9$ with respect to CO_2.

Three methods of calculating equilibrium mole fractions for n-heptane in air are compared with data (11) on Fig. 2. A constant pressure of $P_r \sim 3$ and a subcritical range of temperatures is covered. The calculated phase equilibrium constant method gives the best agreement.

Fr-12-air system calculations are compared with the data of Parmelee (41) in Fig. 3. The agreement over the range of data, up to P_r of 0.3, is good.

The Chemical Abstracts from 1955-1969 were searched for vapor-liquid equilibrium data of any sort for Fr-13. The compilation of Chu et al. (12) published in 1956 was consulted in addition. No data was found. This negative result, of course, provided the motivation for developing and testing a method of computing the equilibrium mole fractions of binary mixtures at high pressures.

Only the case of thermodynamic equilibrium at the interface has been considered to this point. It seems possible that the concentration of the continuous phase gas in the liquid may not reach the equilibrium value particularly if the vaporization rates are rapid. A limiting value would be the case of no absorption in the vaporizing liquid. The phase equilibrium constants and, thence, the interface mole fractions for the limiting case of no absorption can be easily calculated by the method outlined if the liquid phase activity coefficient, γ_{iL}, in Eq. (2.25) and

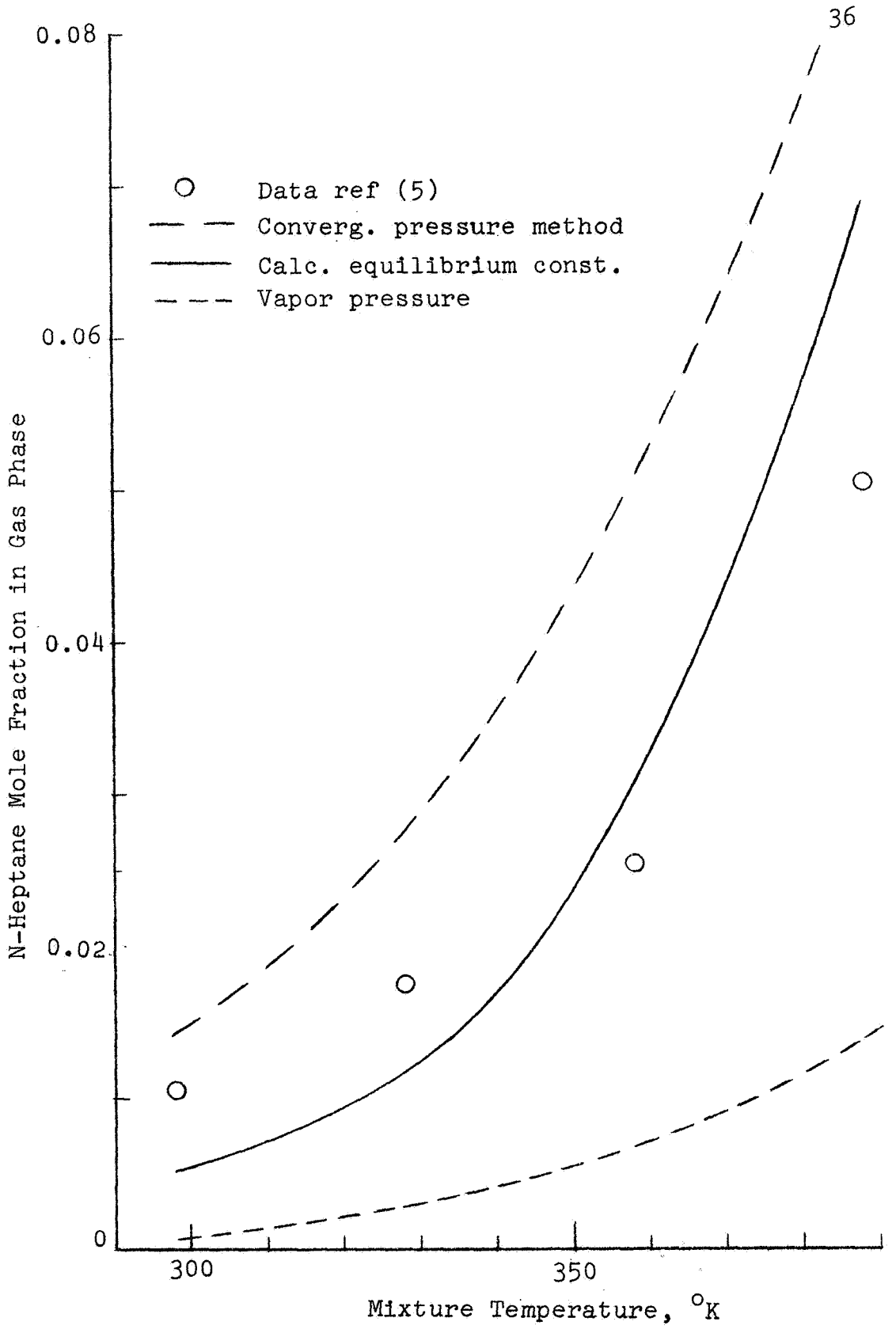

Fig. 2. Equilibrium Gas Phase N-Heptane Mole Fraction in N-Heptane-Nitrogen Two Phase Mixture at 100 Atm

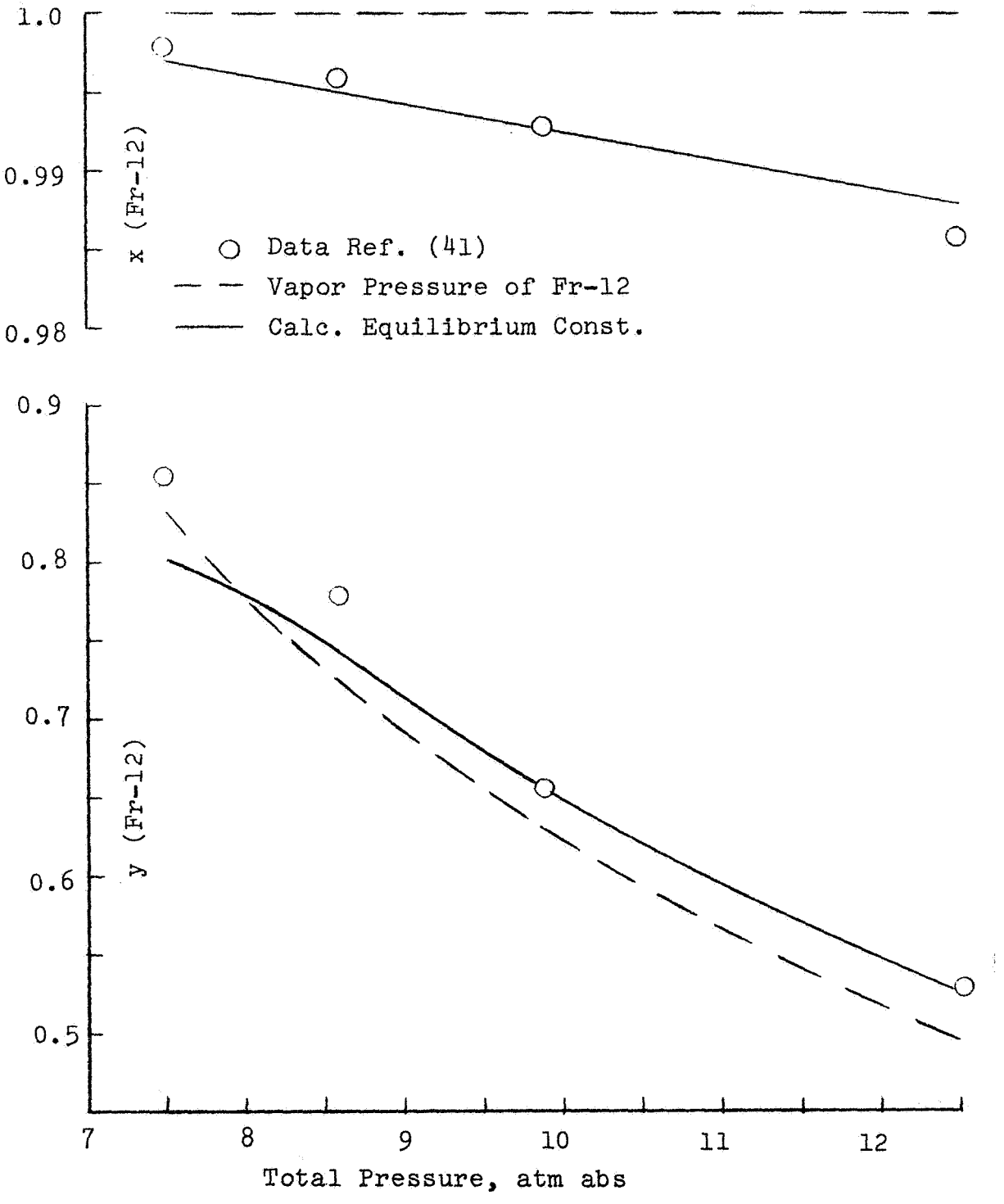

Fig. 3. Vapor-Liquid Equilibrium Relations for Fr-12-Air Mixtures at 24° C

x_A in Eq. (2.32) are unity. The results of calculations employing this assumption for Fr-13 drops vaporizing in air are discussed in Chapter V.

Latent Heat of Vaporization

Consider a binary mixture in vapor-liquid equilibrium such as is normally assumed to exist at a vaporizing drop-film interface. The latent heat of vaporization of A, λ_A, is defined as the difference between the partial molar enthalpy of A in the vapor and the enthalpy of A in the liquid.

At low total pressures the assumption of substituting the heat of vaporization of pure A at $T = T_{sat}$ is commonly used. This assumption is made in the low pressure film theory calculations. However, this approach will lead to substantial errors at total pressures in the vicinity of or greater than critical pressure of component A. A method of accounting for these high pressure effects has been developed by Manrique and Borman (36). Their method which is applied to the determination of partial molal enthalpies of gas mixture components for use in the high pressure film theory calculations is outlined below.

The Redlich-Kwong equation of state is applied to a gaseous mixture. The equation for the mixture compressibility factor is rearranged into the form of a cubic and solved by the Newton-Raphson method. The enthalpy deviation

from the ideal state is computed from the temperature partial derivative of the log fugacity partial pressure ratio.

Reid and Sherwood (47) have tabulated generalized enthalpy deviation as a function of reduced pressure, temperature and critical compressibility factor. Their generalized results based upon an integrated three parameter equation of state were extended to liquid phase enthalpy deviations by the use of a generalized correlation of latent heat of vaporization. The Reid and Sherwood values were used to find the liquid phase enthalpy deviations.

Thus, the latent heat of vaporization in the high pressure region was computed as the difference of gas and liquid phase enthalpy deviations. Typical computed values for the Fr-13-air system are compared with the pure Fr-13 values in Fig. 4.

Thermal Conductivity

Lenoir, Junk and Comings (34) developed a corresponding-states-type correlation for gases at high pressure. Their correlation is based upon nitrogen, methane, argon, ethane, ethylene, and carbon dioxide data over a large pressure range. Thermal conductivity ratio, $k^{\#}$, is correlated as a function of reduced pressure and temperature. It is defined as the ratio of conductivity at any pressure divided by the thermal conductivity at atmospheric pressure.

Values of thermal conductivity for the pure components

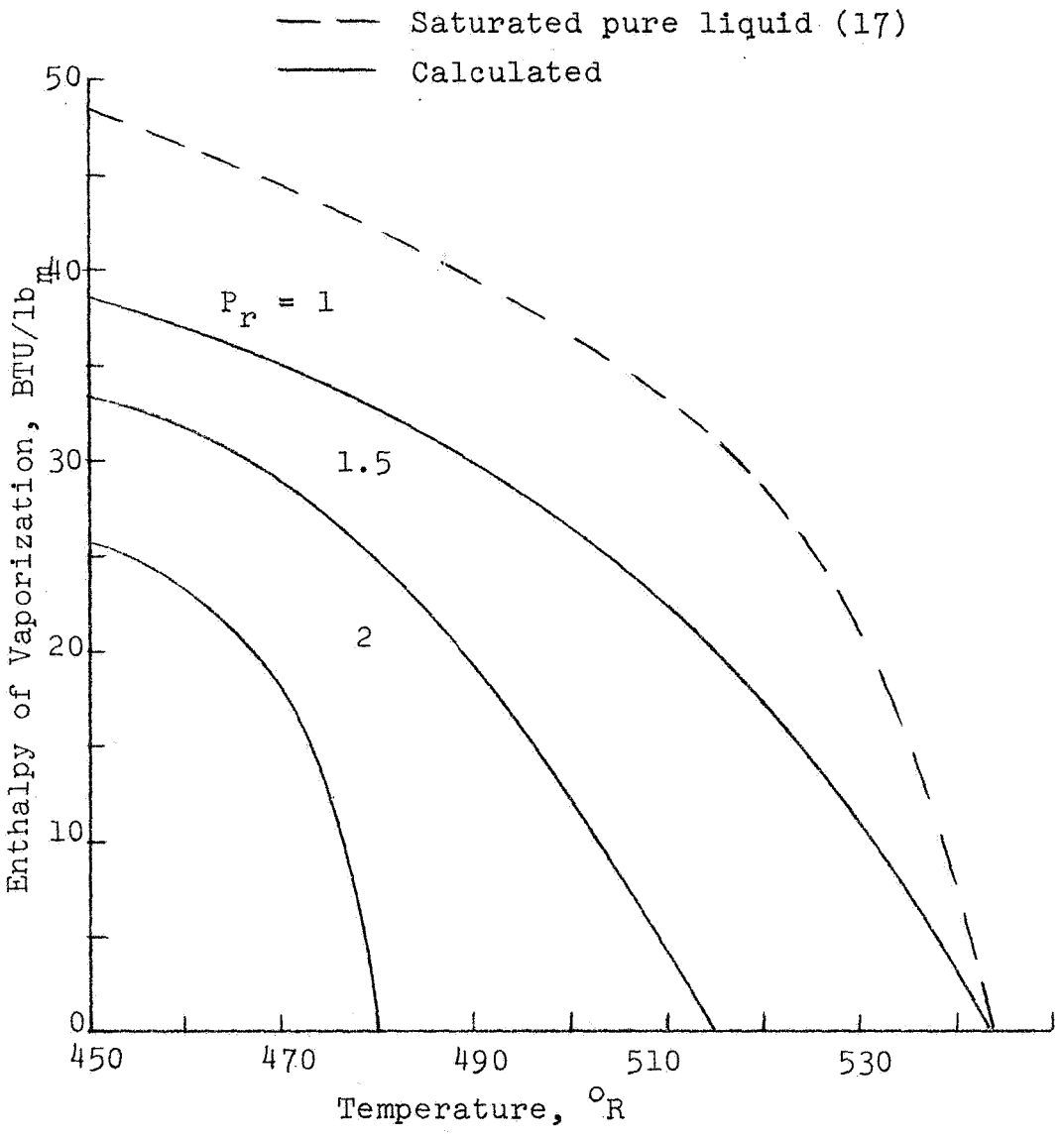

Fig. 4. Effect of Pressure on Enthalpy of Vaporization of Fr-13 in Air

of the film gas mixture, e.g., Fr-13 and air, are computed at the average film temperature. Atmospheric values are utilized. The low pressure values, k_i, are combined by means of the Mason-Saxena method which is given by Bird, Stewart and Lightfoot (4). They are weighted by mean film values of component mole fractions.

$$k_m^{lp} = \sum_{i=1}^{n} \frac{y_i \, k_i}{\sum_{j=1}^{n} y_i \, \phi_{ij}} \tag{2.35}$$

where

$$\Phi_{ij} = \frac{1}{\sqrt{8}} \left(1 + \frac{M_i}{M_j} \right)^{-1/2} \left[1 + \left(\frac{\mu_i}{\mu_j} \right)^{1/2} \left(\frac{M_j}{M_i} \right)^{1/4} \right]^2 \tag{2.36}$$

$$k_m = k^{\#} \, k_m^{lp} \tag{2.37}$$

k_m^{lp} is the mixture thermal conductivity at atmospheric pressure, k_m is the corrected value of mixture thermal conductivity, M_i and μ_i are the molecular weights and the viscosity of species i, and y_i is the film average mole fraction of species i.

In order to correct this value for high pressure, the correlation of Lenoir, Junk and Comings is utilized with the pseudocritical properties determined by mole fraction averages of the pure component critical temperature and pressure values. Then the reduced pressure and temperature are

based on the total pressure and average film temperature values.

Operationally, the values from the Lenoir, Junk and Comings correlation at various reduced temperatures at a specific reduced pressure were fitted by a third order least squares routine. This derived function was then utilized for Fr-13 drop vaporization calculations at a particular pressure. The reduced pressure could be fixed because fortunately the critical pressures of air and Fr-13 are almost identical, and therefore, the pseudocritical mixture pressure is independent of mixture composition.

Property Variation Through the Boundary Layer

A major uncertainty in the application of film theory to droplet vaporization problems at high pressures and temperatures is the variation of properties through the boundary layer. Consideration was given to including a correction term or providing an averaging technique to account for this. This approach was abandoned after techniques were investigated. The techniques considered were found to be complicated and uncertain since no comparisons with data were given. Nevertheless, the techniques surveyed are interesting, and they are briefly summarized. The matched asymptotic series (1), reference state (32), successive iteration (52), and stagnation point methods are discussed.

Acrivos (1) showed that by piecing together exact asymptotic solutions for the cases of Prandtl or Schmidt numbers equal to zero, Nu_0, and infinity, Nu_∞, a simple expression for the Nusselt number in laminar boundary layer flow can be obtained. In the case of the constant property solution Acrivos demonstrated that the Nusselt number divided by the square root of the Reynolds number reduced by the asymptotic result for Prandtl number equal to zero is a simple function of Nu_0/Nu_∞. Comparison of exact numerical solutions indicated that his results were almost insensitive to geometry.

He generalized this result to the case of variable properties. However, in order to solve for the Nusselt number, it is necessary to solve two separate non-linear integro-differential equations by expansion and summing of an asymptotic series. Derivatives and integrals of the properties have to be evaluated, and the algebra is very complicated. His approach is not easily adaptable to a digital computer. It would be necessary to further generalize his result for the case of simultaneous heat and mass transfer which would add further complication. Acrivos admits that there may be some question about the independence of the variable property result from geometry.

A method of reference states was proposed by Knuth (32). He developed reference state prescriptions by a combination of exact calculations for laminar couette flow and the

analysis of few calculated results of boundary layer problems. There is substantial uncertainty in applying his results to correlations for over all transfer numbers to geometries other than flat plate particularly where separation occurs. Furthermore, he claims that the composition reference state reduces to a linear average in all cases except where the ratio of molecular weights of the two species exceeds a factor of ten. The deviation of his reference states from those obtained by linear averages of temperature and composition were very small for a typical Fr-13 case.

In the case of laminar boundary layer flow over a flat plate Schuh (52) performed calculations of variable properties. His method is quite simple and appears to be well suited for a digital computer. He starts with the constant property Blasius and Pohlhausen solution for the velocity and temperature profiles, determines the velocity profile with the viscosity and density variation from the initial temperature variation, and finally the new temperature profile from the new velocity and initial density profiles. It is claimed that this procedure converges after four repetitions.

Schuh's calculations were applied to air with variable properties. He found that although the boundary layers thickened, there was no appreciable change in shearing stress or heat transfer coefficient over the constant

property case. The uncertainty of applying this method to correcting heat and mass transfer coefficients for spheres exists since the flat plate equation is used.

The idea of applying Schuh's successive iteration approach to the forward stagnation point on a two or three dimensional body of revolution naturally arises. However, there is again the question of applicability of a correction for a single point to an average value determined empirically. Intuitively, one would expect better results than in applying the flat plate or plane two dimensional result directly.

III. EXPERIMENTAL APPARATUS

The experimental apparatus provides a means of introducing and supporting a droplet in a stream of heated high pressure air and obtaining a size and temperature history of the evaporating droplet. J. A. Ricart-Lowe (48) and L. D. Alexander (2) have previously described parts of this apparatus. A complete description of the rig which is shown in a photograph, Fig. 5, is given here.

Rig Components

The rig is conveniently subdivided into a heater, test section and probe assembly. These components are described in order.

A cross sectional view of the heater is shown in Fig. 6. It consists of a cylindrical flanged pressure vessel which contains a packed bed heated by four semi-circular pipe heaters. The heater is "wye" connected with a 220 v three phase a-c source which provides a maximum total power of 4.6 kw.

The air flow passes up from the inlet nozzle over the top of the radiation shield, down between the radiation shield and heater units, and up through the heater bed to the test section. The structural and thermal design of the heater are discussed by Ricart-Lowe (48).

The test section consists of a 12 in. high rectangular

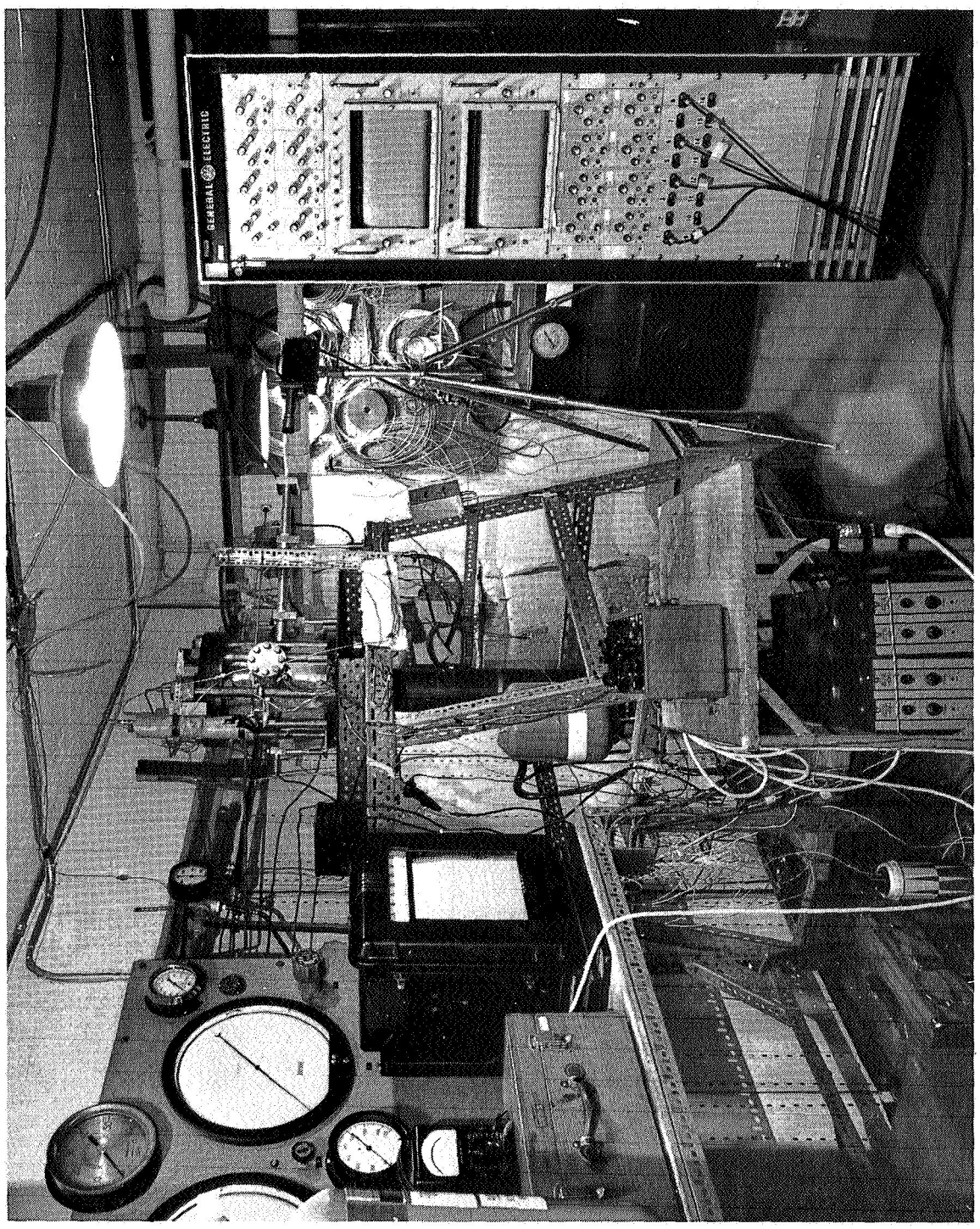

Fig. 5. High Pressure Suspended Droplet Vaporization Apparatus

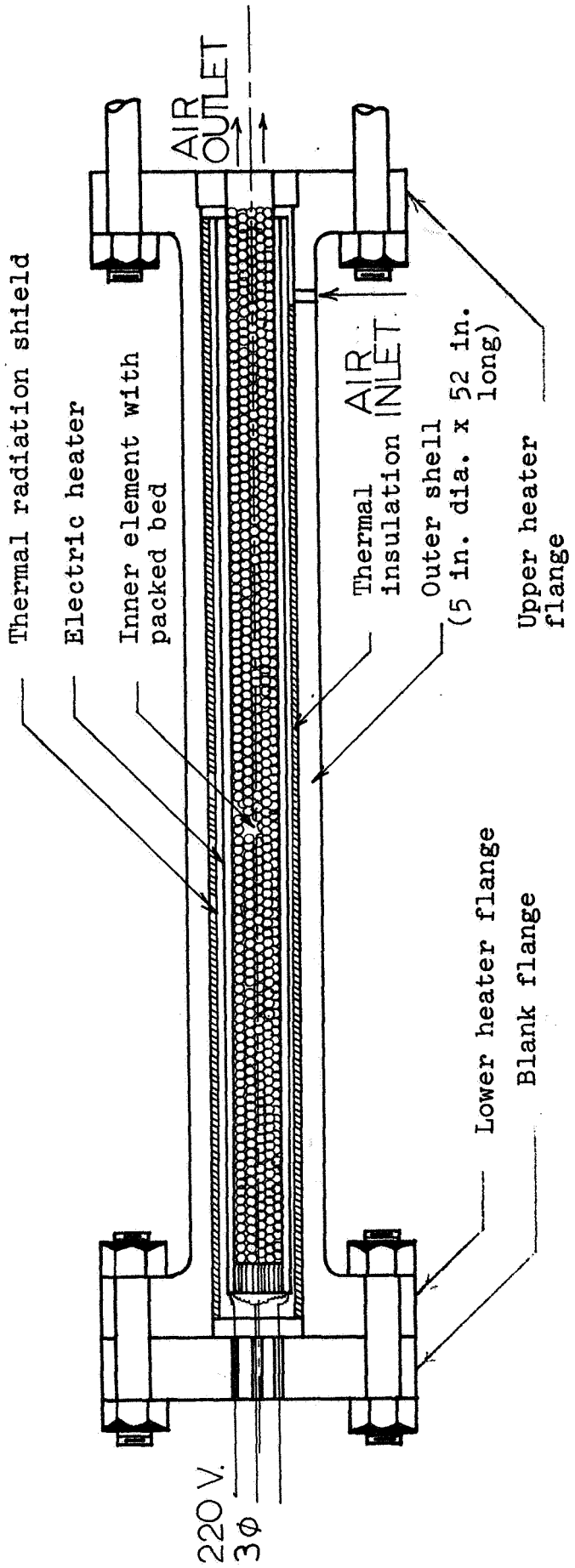

FIG. 6. VERTICAL SECTION THROUGH HIGH PRESSURE HEATER

block of stainless steel with a 6 in. square cross section. Fig. 7 shows a cross sectional view. Two window assemblies, a probe assembly which is described below, an inlet calming section and nozzle, numerous penetrations, and a top flange complete the list of components of the test section.

The calming section, which is composed of a series of screens and spacers, tends to break up turbulence and flatten the air stream temperature profile. A 1 in. diameter ASME nozzle (3) was utilized. A teflon sleeve with an inside diameter of 1 in. fits upon the top or throat of the nozzle in order to isolate the region around the probe tip from free convection currents.

Penetrations in the test section are provided for a pressure gauge line (1/2 NPT) and the probe thermocouple leads (3/8 NPT). The probe assembly and two window subassemblies bolt to the sides of the test section. The test section is clamped by means of bolts between the heater upper flange and another blank flange which rests on top of the test section. A detailed discussion of the test section is given by Ricart-Lowe (48).

The probe which introduces and supports the droplet is an independent assembly which bolts to the side of the test section. It consists of a housing (not shown) and a brazed subassembly of tubing shown in Fig. 8. The subassembly which is joined to the housing juts out from the housing flange into the test section where it makes a

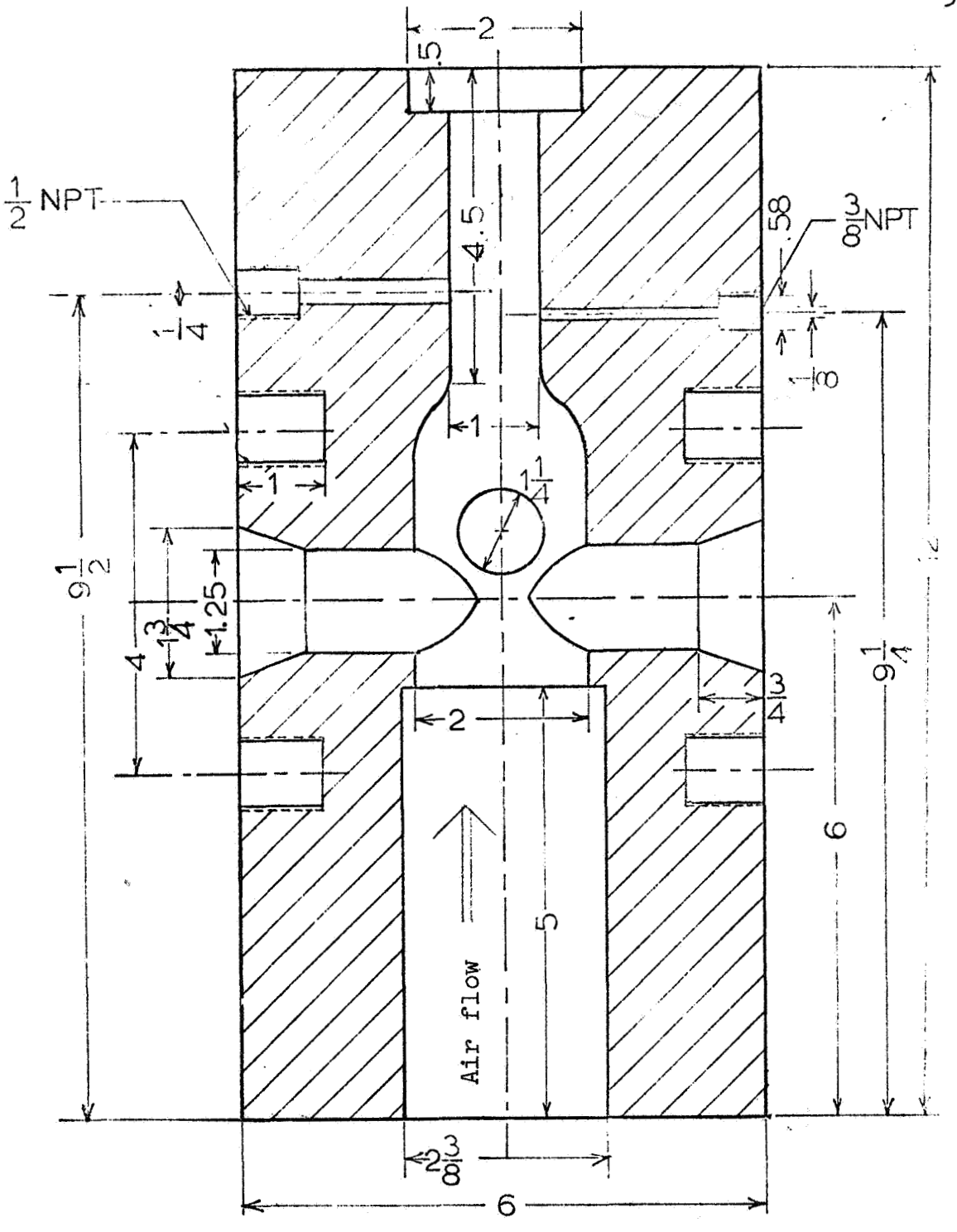

Fig. 7. Vertical Section of Test Section

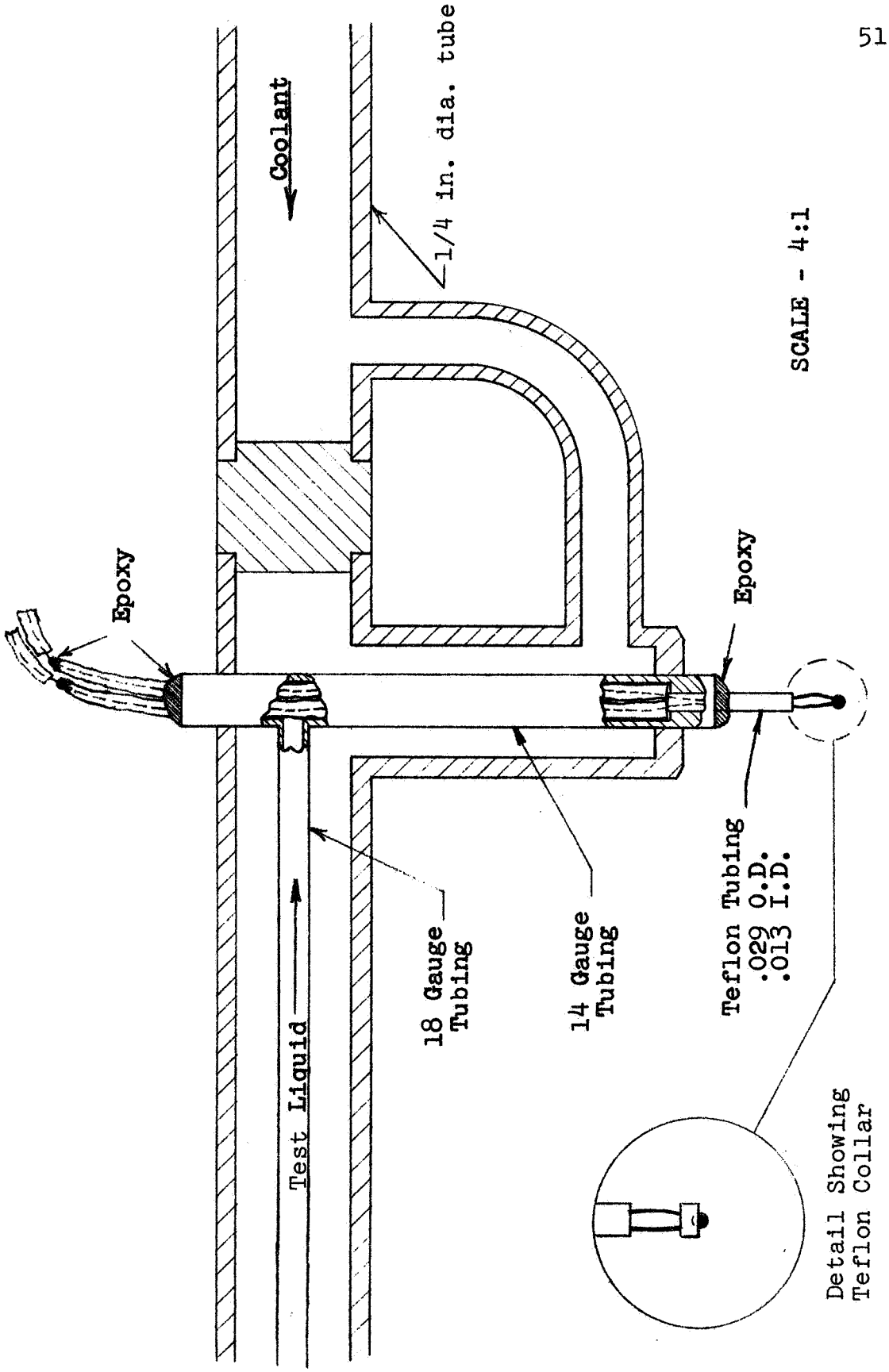

Fig. 8. Cross-Section of Probe Subassembly

connection with the inlet cooling water line.

The coolant enters the end of the 1/4 in. diameter tube of the probe subassembly where it is sealed by an O-ring to a fitting on the inside wall of the test section. The coolant flow through the tube around the probe tip and out the annular space between the 18 gauge test liquid supply line and the 1/4 in. tube.

The test liquid flows from the bottom of the condensor-reservoir through the activating valve (#1 on Fig. 9), through the 1/8 in. diameter stainless steel tubing to the probe housing where it passes through a pressure seal in the probe housing. The test liquid then leaves the probe housing and flows into an 18 gauge stainless steel hypodermic tubing part of which is shown on Fig. 8.

The test fluid passes down around the teflon insulated thermocouple lead wires to the 0.029 in. diameter teflon probe tip. The section of 14 gauge tubing is sealed at the top with epoxy glue. The probe tip is also joined to the tube with epoxy. The thermocouple lead wires are sealed by epoxy to their spaghetti insulation about an inch above their outlet from the tubing. The test liquid is forced out the teflon probe tip where it can flow down the lead wires and form droplets on the thermocouple bead.

A teflon collar was placed around the probe thermocouple leads immediately above the junction in the Fr-13

tests. This was found necessary in order to support the droplets for the tests. Alexander (2) gives a discussion of the probe details.

Flow Arrangement

The flow diagram, Fig. 9, shows the functional arrangement of the rig components. Paths of the vaporizing medium, water coolant and air are included in the diagram.

The vaporizing medium is introduced into the Fr-22 cooled condensor-reservoir through valve #2. It is fed into the probe by activating valve #1 and utilizing a difference in pressure between the test section and reservoir.

The regulating values, either high or low pressure, maintain the air pressure in the rig. Air acts as a pressurizing agent for the probe coolant and the condensor-reservoir as well as a heat transfer medium for droplet vaporization in the test section. Air is available from either a 2000 psi reservoir (dried by cooling to 32° F at 1800 psia) or a house air line at 75 psi. Air flow through the rig is regulated by choking the flow from the rig outlet at valve #6.

Water cools the probe supply line. The coolant is maintained at the system pressure by a wash bottle arrangement which has to be refilled about every 2 hours. Cooling coils in an ice bath cool the water as it flows from the bottle to the test section.

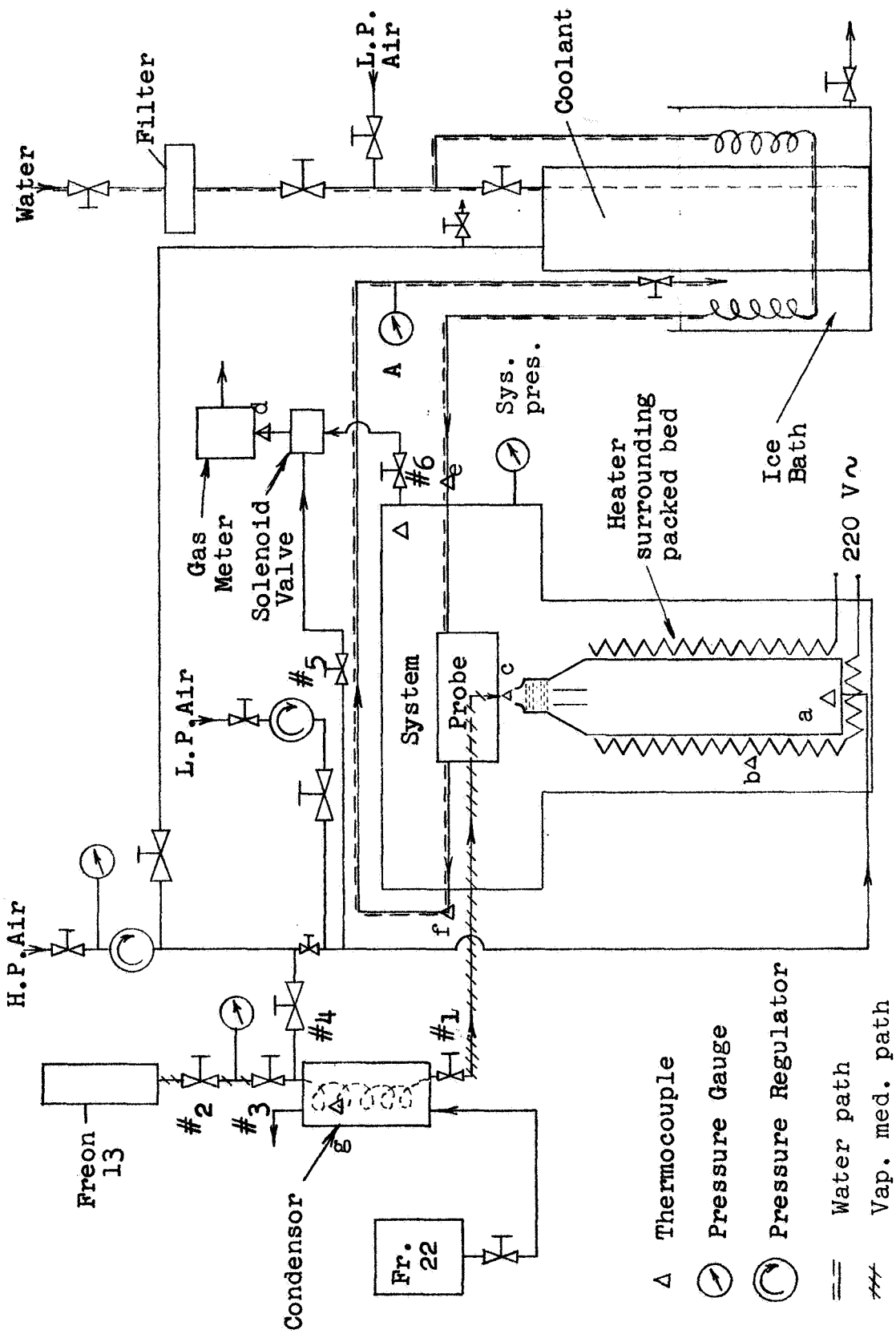

Fig. 9. Flow Diagram of High Pressure Suspended Droplet Vaporization Apparatus

Instrumentation

Instrumentation is provided to obtain droplet temperature and size histories, air flow rate, system pressure and various operating temperatures and pressures for performance maintenance, safety and control of the rig. The flow diagram, Fig. 9, shows the location of the temperature and pressure sensors.

The probe temperature and the gas meter inlet air temperatures are recorded continuously on a brush recorder. The other temperature signals are recorded on a multipoint chart recorder.

Either of two precision pressure gauges are used to determine system pressure. The ranges are 0-750 psia and 0-1500 psia, respectively; the accuracy is 0.1% of full scale reading for each.

The volumetric air flow through the test section is determined by the use of a 1800 ft^3/hr capacity gas meter and stop watch.

The optical system used to obtain droplet size histories is shown schematically in Fig. 10. This arrangement produces a shadowgraph of the probe tip on a ground glass screen. Light from a point source zirconium-arc lamp is focused about an inch in front of the thermocouple, and the shadow image is collimated by a single lens upon the ground glass. The magnification usually used is about six. Linear magnifica-

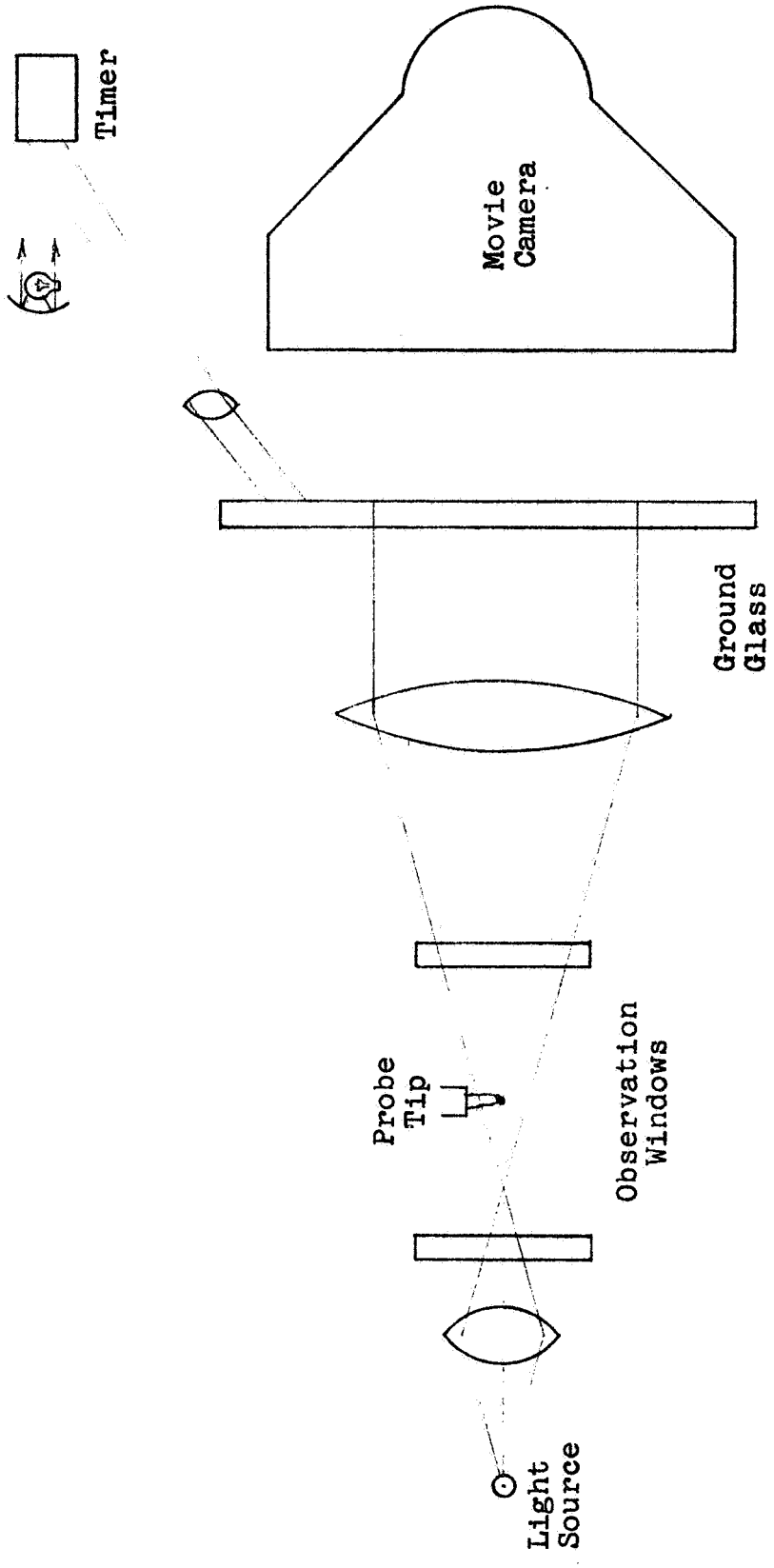

Fig. 10. Schematic Diagram of Optical System

tion of objects at the probe plane was established by two methods. Optical bench mock-ups of the setup using still photographs of a reticle grid as well as actual objects placed in the probe position of the rig demonstrated linearity. An image of a timer is projected on a mirror in the camera object plane.

16 mm movie films are taken of the ground glass with a Cine-Kodak Special II movie camera. A 50 mm f/1.6 lens which focusses to 13 in. distance is used. 4 X reversible film with normal development procedure, lens wide open, 13 in. object to film plane distance and 64 fps speed were found to give adequate size histories from which measurements could be taken.

A switching circuit was built to synchronize the temperature and size histories. When a switch is thrown, a timing mark is produced on a channel of the temperature recorder, and the timer which appears on the movie record is started.

Rig Operation

A description of the operating procedure for data gathering is given in this section.

The heater is turned on and house air is flowed through the rig until the entire assembly is warmed up. This takes about six hours. During the start up period the instrumentation is warmed up and calibrated, the coolant cylinder

and ice bath are filled, and the optical system is aligned.

The test fluid is placed into the coils of the condensor. After the rig has achieved steady state, the air fluid reservoir is pressurized to about 75 psi above the desired operating pressure. The probe coolant is started, and the system pressure and the air flow rate are adjusted to the test values.

At this stage the test is initiated as follows. The test liquid can be made to drip on the probe thermocouple by manipulating valve #1. The temperature recorder is started. When a stable drop is residing on the probe thermocouple, the camera is started and the "start" switch of the synchronization circuit is activated. The camera is stopped when the drop disappears and the temperature recorder remains on until the air temperature measured by the probe sensor recovers its initial value. Normally, the air flow is stopped to conserve air and a cursory analysis of the temperature history is made before proceeding to the next droplet history.

IV. EXPERIMENTAL UNCERTAINTIES AND DATA REDUCTION

In the opening section of this chapter experimental problems which introduce errors are discussed. The second section deals with the data reduction techniques which were employed. Uncertainties in the experimental results and their implications regarding the calculated results are treated in the final section.

Sources of Experimental Error

There are several problems which attend high pressure suspended droplet vaporization experiments. The combination of forced and free convection, reduced surface tension, and non-convection heat losses are among the problems; they are discussed below.

In mixed or combined convection problems, the important parameter is Gr/Re^2, the ratio of the Grashof number to Reynolds number squared (30). In the situation where the characteristic length, forced flow velocity, fluid temperature and temperature difference remain constant, Gr/Re^2 would be independent of pressure. If these conditions did indeed prevail for droplet vaporization, the importance of combined convection, which is measured by Gr/Re^2, would not increase as the pressure is increased.

Experimentally it was found that the air velocity in the test section had to be reduced as the pressure was

increased in order to maintain stable drops. Since the other parameters in Gr/Re^2 remained approximately constant, Gr/Re^2 increased with increasing pressure. A consideration of the critical Weber number criteria for drop stability explains this experimental fact.

$$We = \frac{u^2 D\rho}{\sigma} \tag{4.1}$$

As shown in Eq. (4.1) the square of the velocity, u, corresponding to the critical value of the Weber number is proportional to drop surface tension, σ, and inversely proportional to the gas density, ρ. Through the combined effect of gas density which increases with pressure and drop surface tension which decreases with pressure (47), the maximum velocity that results in a stable droplet decreases with increasing pressure.

In the region of combined free and forced convection heat transfer to spheres, $Gr/Re^2 > 0.3$, the heat transfer rates for opposed flow are lower than that predicted by pure forced convection (59). However, for the case of simultaneous heat and mass transfer to spheres in opposed flow, the opposite effect has been observed although the region of combined convection, approximately $0.001 < Gr/Re^2 < 200$ for $P_r = 1$, is different (38). Although velocity components arise from both temperature and concentration differences, both are in the same direction, i.e., downward for cool, dense vapors. In the case of Fr-13 data, both are important but neither

predominates. This rather remarkable result is another illustration of the danger inherent in indiscriminate application of heat-mass transfer analogies. Since Narasimhan and Gauvin's experiments (38) were carried out at turbulence intensity levels less than 1%, at Prandtl numbers of 1, at steady state and over a limited range of variables, their results were only used interpretatively and not quantitatively.

The upper limit on velocity at higher pressures also causes an increase in the free convection from the test section walls. This tends to disturb the uniform velocity distribution at the outlet of the nozzle. In the initial high pressure experiments fluctuations in air temperature at the probe tip led to two successive design changes in the apparatus. The first change was an enlargement of the flow nozzle from 1/2 to 1 in. diameter. The second, which finally eliminated the problem, was a lengthened nozzle.

A second source of experimental error relates to reduced droplet surface tension. Since the droplet surface tension decreases with increasing pressure, droplet stability becomes a problem. This stability phenomenon not only limits the velocity which enhances free convection as discussed above, but it also leads to troublesome droplet behavior, and it limits the droplet size obtainable.

Glasstone (20) gives the following formula for the

apparent weight, W, of a drop which drips from a fed tube of radius, r,

$$W = 2\pi r\sigma\phi \qquad (4.2)$$

where ϕ is an empirically determined correction factor. In applying this criterion to estimate drop size, r would correspond to the probe tube tip radius. An increase in ambient pressure would decrease σ which in turn would limit the drop weight or size obtainable.

At the onset of instability, the droplet oscillates in a vertical direction alternately taking the classical oblate and prolate shapes. When this problem occurs at high pressures, it either leads to loss of support (droplet falls) or damped droplet oscillations after sufficient size reduction due to rapid vaporization. Occasionally droplet spinning occurred at high pressures. The effects of this behavior on heat and mass transfer rates are difficult to assess, but it undoubtedly increased the average rates above what would be predicted by steady state correlations.

Analysis of the movie film histories from an initial series of Fr-13 experiments showed that frequently the droplet clung to the bottom half of the spherical thermocouple bead and did not envelop it as most liquids would at room temperature and atmospheric pressure. The exposure of the unwetted top portion of the bead provided an extraneous heat energy source to the droplet. The plateau temperatures

obtained in this series of tests were suspiciously high when compared to values predicted by film theory. This was later confirmed by Fr-13 data taken with a redesigned probe tip. The latter data are reported in Chapter V.

There are two non-convection sources of heat transfer to a suspended drop which may contribute to experimental error. One is radiation from the test section walls, and the other is the thermocouple lead wires. An estimate of the fraction of the total heat rate transferred to the drop by radiation was made for a typical experimental condition.

The radiative energy flux was considered to be composed of two components. The first from the test section walls which were assumed to be at 150° F (the outside wall is warm to the touch) was assumed to have emissivity and view factors of unity. A second component was due to the air calming section which can be seen through the nozzle from the drop location. It was assumed that the calming section was at 300° F, the apparatus maximum air temperature. A view factor was estimated by assuming that the geometry corresponded to two parallel disks (33), and that the effective emissivity was unity.

The computed radiative heat flux was found to be less than 4% of the convective heat flux for an 0.033 in. diameter drop with a computed Nusselt number of 16.4 and air-drop temperature difference of 100° F.

An estimate of the heat loss from the thermocouple lead

wires was also made. It was assumed that the 0.005 in. diameter lead wires acted as infinitely long one-dimensional fins. An average wire thermal conductivity of 10 BTU/hr-ft-^{o}F was assumed which corresponds to the chromel-constantan lead wires.

A temperature difference between the lead wire root and ambient gas of 180^{o} F and a convective heat transfer coefficient of 230 BTU/hr-ft^{2}-^{o}F were used in the calculation. The heat energy arriving from both lead wires computed in this manner was found to be less than 3% of the convective heat energy found for the previously outlined case. Although the model assumed is crude, it is believed that the assumptions are conservative. Furthermore, for the Fr-13 data, 0.003 in. diameter lead wires were substituted for the 0.005 in. wires assumed in this calculation.

Data Reduction Techniques

The important data from a drop vaporization run are droplet temperature history, size history, air temperature, air pressure and gas flow rate through the test section. In comparing the results of transient calculations with experimental droplet histories, the calculated dependent variables are droplet temperature and size histories. Representative experimental histories for a Fr-13 drop run are illustrated below, and then the data reduction technique is described.

The droplet size histories were obtained on 16 mm movie film. Prints of a Fr-13 film history are shown on Fig. 11. A photograph of the corresponding temperature history record for the Brush recorder is shown on Fig. 12. The conditions of the run were pressure = 47.8 atm (P_r = 1.25), air temperature = 171.5° F, and air velocity 3.37 in./sec. The timer started about 32 frames before frame 0. The voltage step shown on the channel 1 of the temperature record coincides with the timer commencement. The marks at the top edge of the temperature record are second marks; the chart speed was 125 mm/sec. The droplet was being fed until frame 2.

The temperature history is reduced by picking millivolt values off the data record at frequent intervals and translating them to temperatures by means of a conversion chart. Each channel of the recorder was calibrated with a potentiometer over the entire range being used, and this procedure was repeated each time the range was changed.

A rather elaborate procedure of droplet size data reduction was necessary because of the drop shape distortions. The data shown in Fig. 11 illustrate the non-spherical drop silhouettes. After a particular frame of the film record was selected for size determination, it was projected on a large white piece of cardboard at a range of about 15 ft. The drop outline was traced on a piece of paper. Next, the paper was put on a glass-topped tracing table, and the drop

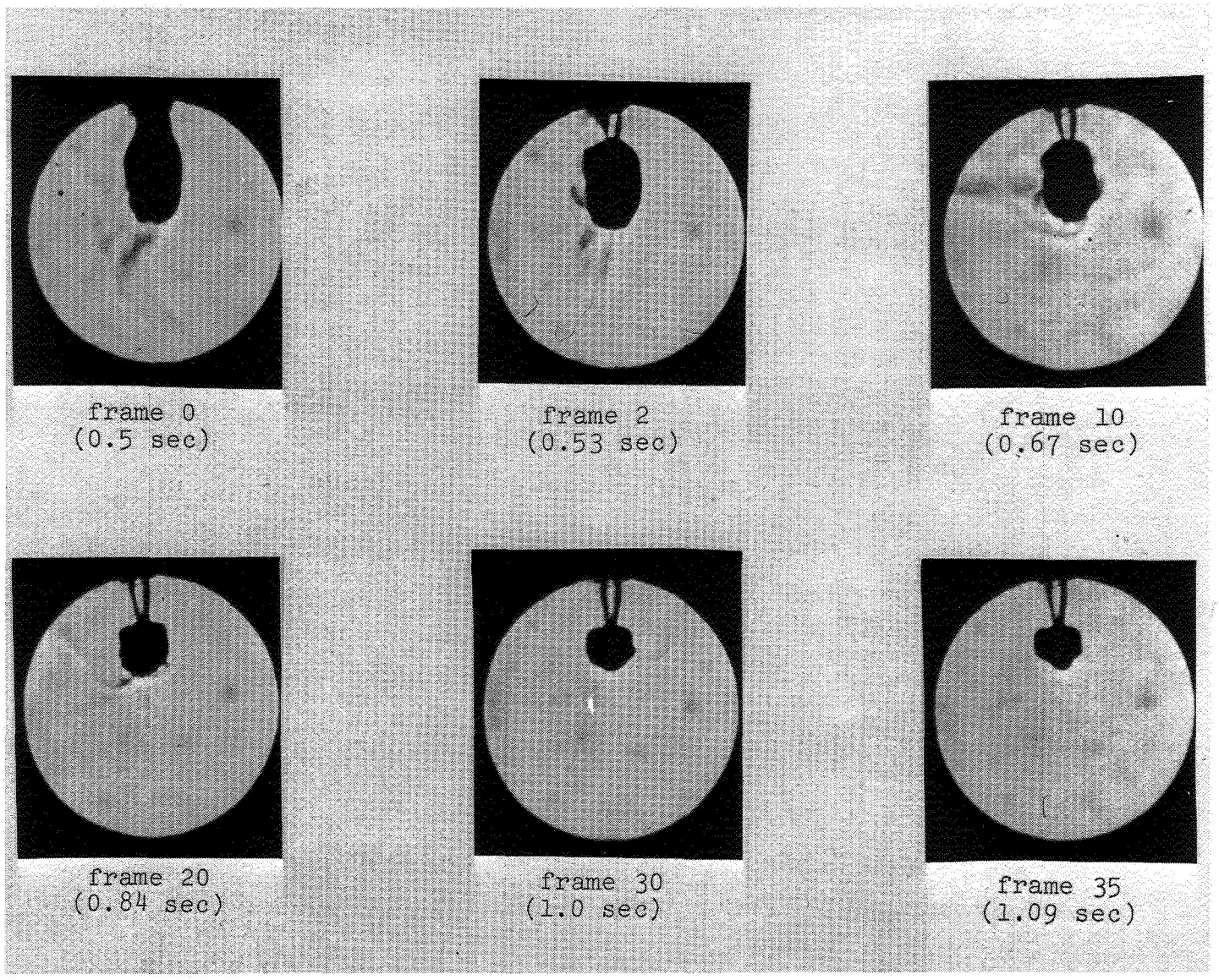

Fig. 11. Photographic Drop History of Fr-13 Drop Vaporizing in Air at 47.8 atm abs

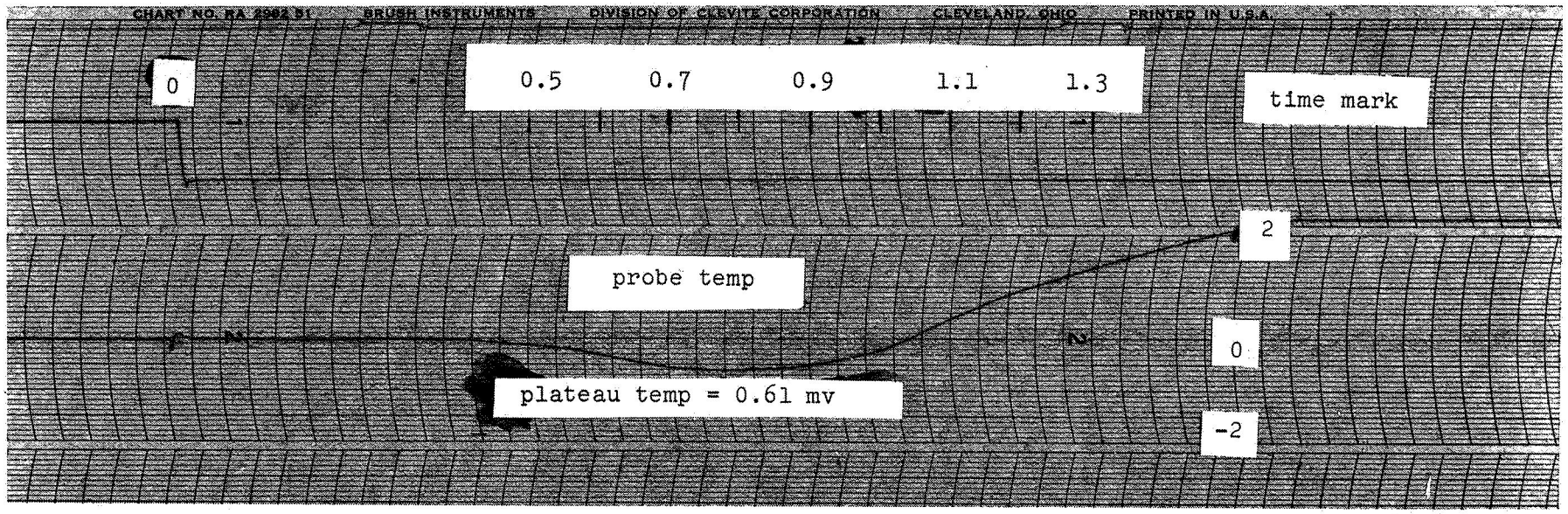

Fig. 12. Drop Temperature History of Fr-13 Drop Vaporizing in Air at 47.8 atm abs The time is with respect to the timing mark. The actual droplet history began at 0.53 sec. The temperature prior to 0.53 sec is a feed temperature.

outline was traced on vellum paper.

An axis of symmetry of the drop was found by folding the vellum sheet, so that it split the drop profile in half. This step required judgment since the drop half outlines were not always coincident. For the drop profile shown on Fig. 13 about 12% of the measured drop volume is contained in the region between the overlapping boundaries. 8% is positive and 4% is negative. One half of the drop profile was divided into a number of segments the same height as shown on Fig. 13. Then the drop volume and surface area were determined by assuming that the drop was composed of frustrum of a cone shaped segments with radii shown on Fig. 13. The drop volume, V, and surface area, A, were computed by Eqs. (4.3) and (4.4).

$$V = \frac{\pi h}{3} \sum_{n=2}^{N} \left(2r_n^{\,2} + r_n \, r_{n-1} \right) \tag{4.3}$$

$$A = \pi \sum_{n=2}^{N} \left[r_{n-1} + r_n \right] \left[h^2 + (r_n - r_{n-1})^2 \right]^{1/2} \tag{4.4}$$

n-1 is the number of increments, r_n are the radii, and h is the segment height. The mean chord length, D_{ch}, was calculated by Eq. (4.5)

$$D_{ch} = 6V/A \tag{4.5}$$

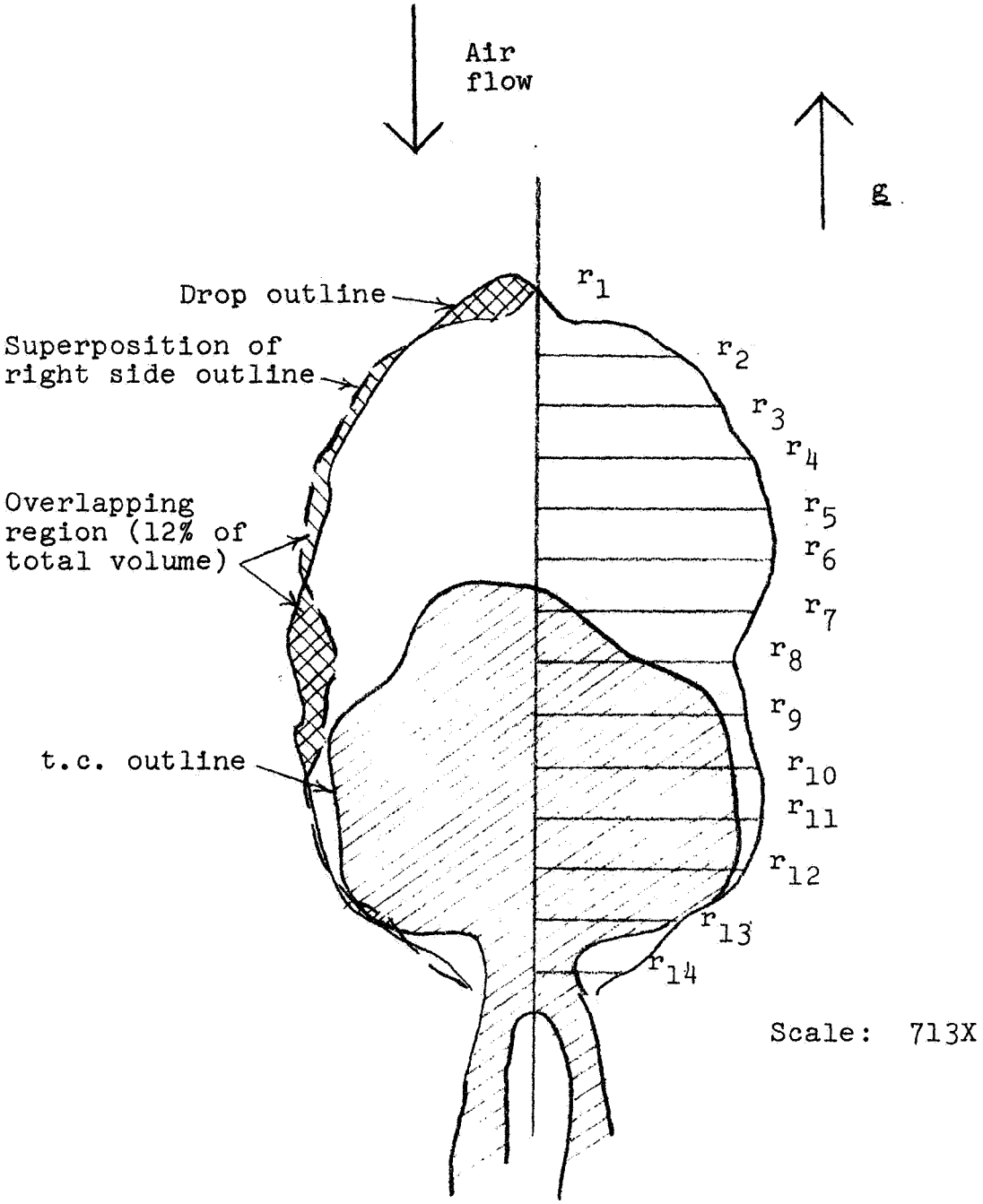

Fig. 13. Profile of Fr-13 Drop Vaporizing in Air at 47.8 atm abs

The mean chord length is used in the calculations as a characteristic length in the heat and mass transfer correlations and to relate the droplet mass to area with Eq. (4.5). However, a further relation is required to relate D_{ch} to droplet volume. This relationship is discussed in the following paragraphs.

Since the drops were not spherical, D_{ch} differed from the diameter of an equivalent volume sphere. The values computed from Eq. (4.5) were plotted versus volume, V, for a number of data points. This function which is shown on Fig. 14 is within a slight scatter, independent of temperature and pressure. The third order least squares fit to this function and the diameter for an equivalent volume sphere are shown on the figure. The derived relationship between D_{ch} and V was utilized in the droplet history calculations presented in Chapter V.

Droplet mass and temperature were the dependent variables in the transient calculations which are compared with measured droplet histories. At each time interval in the calculation, the droplet volume is determined from the mass, and then the $D_{ch}(V)$ derived relationship gives the diameter and surface area which are used to calculate instantaneous time derivatives of droplet mass and temperature. In this fashion the experimental surface to volume relationship is used in obtaining the calculated droplet histories.

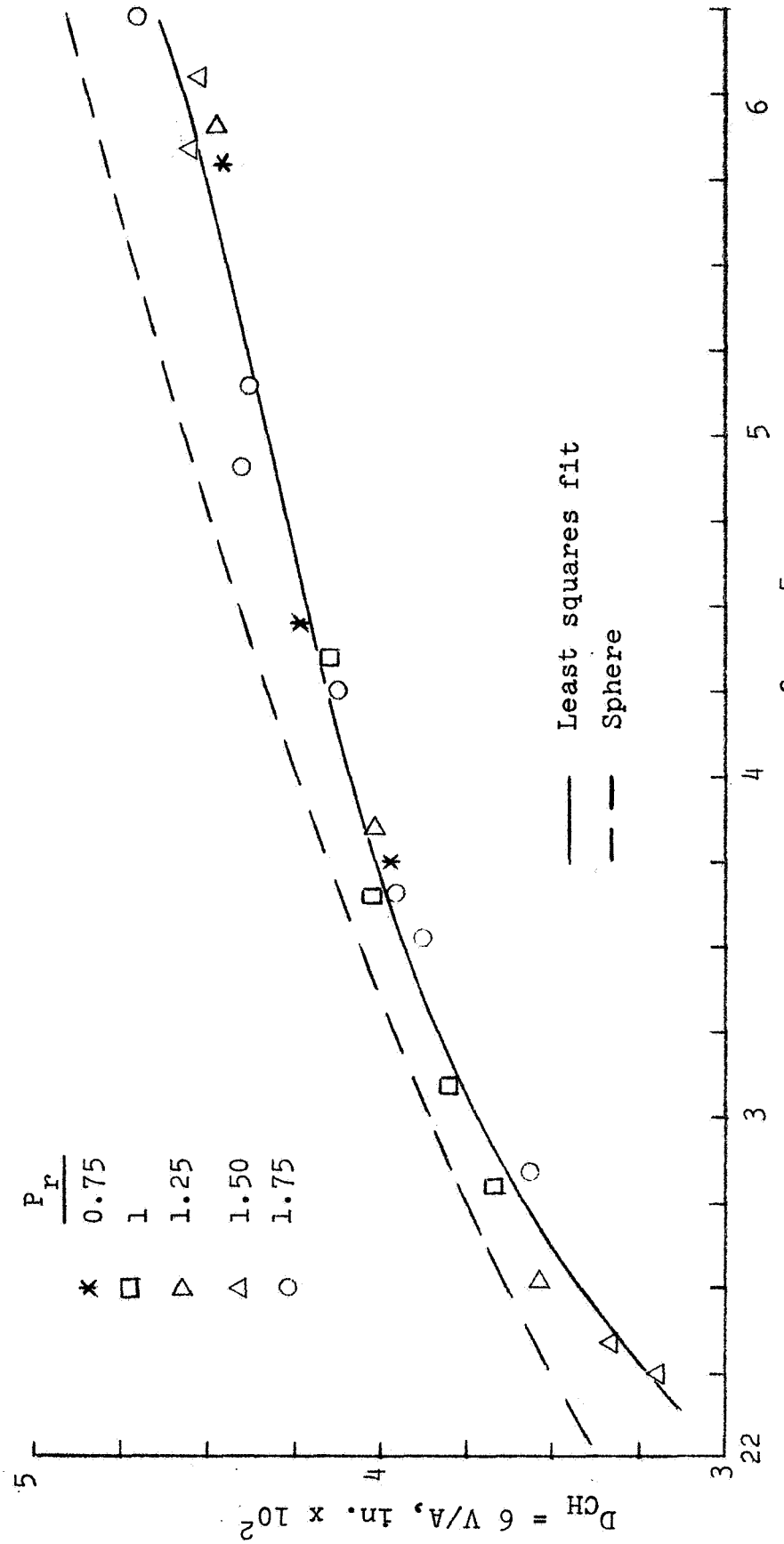

Fig. 14. Equivalent Diameter Variation With Drop Volume, Fr-13 Drops Vaporizing in Air

Estimated Experimental Errors

In the first section of this chapter sources of error which would be expected to introduce bias into the experimental results were discussed. Accurate predictions of these errors is very difficult, and about the only recourse available is to design the apparatus and experimental procedure to minimize these effects. In addition to such errors there are, of course, experimental uncertainties.

Experimental uncertainties include accuracy errors and precision errors. Accuracy errors are detected by calibration procedures, the results of which are applied when the data is processed. This was done for the pressure, temperature, gas flow rate and linear size measurements. Precision errors are due to random fluctuations of the instrument itself in conjunction with the data reading process. An accurate estimate of precision errors requires an experimental determination of measurement error which, since it involves subsidiary experiments, is expensive and time consuming.

In lieu of experimental determinations of precision errors, uncertainties can be readily estimated. Uncertainty is defined as "what we think the error would be if we could and did measure it by calibration" (51). An approximate value of uncertainty that is assumed is a plus or minus accuracy range which includes 95-99% of all readings of the instrument (51). If no accuracy range is given by the

instrument manufacturers, one-half the least count or scale reading is used. Thus, with these definitions and the major assumption that the individual deviation populations are normally distributed, standard procedures for combining independent errors can be applied to obtain precision indices of the experimental results. Furthermore, the implications of these errors regarding the calculated results compared with experimental results in Chapter V can be estimated.

Measurement Uncertainties

The following list of assumptions leads to a simple statistical technique (51) for estimating the uncertainty interval, $\bar{R}$, in a result, R, due to a combination of errors, $\bar{x}$, in variables, x.

1. Estimates of uncertainty intervals are valid for the various variables.
2. Measurement deviation populations are normally distributed.
3. Errors are independent.

The uncertainty interval for N variables is given by Eq. (4.6)

$$\bar{R}^2 = \sum_{x=1}^{N} \left(\frac{\partial R}{\partial x}\right)^2 \bar{x}^2 \qquad (4.6)$$

This technique is utilized to predict the uncertainty interval for the gas flow measurement, V, the velocity in the test section, u, the temperatures of the drop, T_L,

air, T_∞, and gas meter inlet, T_g, and the measured mass transfer rate, $\frac{dm}{d\theta}$. The gas flow is determined by timing the interval for a given quantity of gas to flow through the meter as given by Eq. (4.7)

$$V = \frac{V}{\theta} \tag{4.7}$$

where V is the total volume, typically 3 ft^3, and θ is the stopwatch time, typically 1 min. Applying Eq. (4.6)

$$\left(\frac{\overline{V}}{V}\right)^2 = \left(\frac{\overline{V}}{\overline{V}}\right)^2 + \left(\frac{\overline{\theta}}{\theta}\right)^2 \tag{4.8}$$

A measured temperature, T, consists of a thermocouple potential, v_{tc}, multiplied by scale factors, K_i, as given by Eq. (4.9)

$$T = v_{tc}\, K_1\, K_2\, K_3 \tag{4.9}$$

where the scale factors are the gain of the amplifier, the recorder scale factor, and the slope of the thermocouple calibration curve, respectively. Applying Eq. (4.6), the uncertainty interval for the temperature measurement is obtained as Eq. (4.10).

$$\left(\frac{\overline{T}}{\overline{T}}\right)^2 = \left(\frac{\overline{K}_1}{\overline{K}_1}\right)^2 + \left(\frac{\overline{K}_2}{\overline{K}_2}\right)^2 + \left(\frac{\overline{K}_3}{\overline{K}_3}\right)^2 \tag{4.10}$$

The test section velocity, u, is computed from Eq. (4.11)

$$u = \frac{C\ V\ T_\infty}{P\ T_g} \tag{4.11}$$

where C is a constant which depends on the barometric pressure and test section nozzle size which are assumed to be accurately known, and T_g is the gas meter inlet temperature. Similar manipulations to Eq. (4.11) give the uncertainty interval for u.

$$\left(\frac{\overline{u}}{u}\right)^2 = \left(\frac{\overline{T}_\infty}{\overline{T}_\infty}\right)^2 + \left(\frac{\overline{V}}{V}\right)^2 + \left(\frac{\overline{P}}{P}\right)^2 + \left(\frac{\overline{T}_g}{\overline{T}_g}\right)^2 \tag{4.12}$$

The slope of the drop mass versus time gives the drop mass transfer rate, $dm/d\theta$. The liquid density, of course, has to be used to convert from drop volume to mass. In order to obtain an estimate of measured mass transfer rate uncertainty interval, $\overline{dm/d\theta}$, it is assumed that the measured drop mass transfer rate is proportional to the cube of the drop diameter, D, and inversely proportional to drop lifetime, $\Delta\theta$.

$$\left(\frac{dm}{d\theta}\right)_{exp} = \frac{C\ D^3}{\Delta\theta} \tag{4.13}$$

where C is a constant which includes the liquid density. Operating on Eq. (4.13) with Eq. (4.6), Eq. (4.14) results.

$$\left(\frac{\overline{dm/d\theta}}{dm/d\theta}\right)^2 = \left(\frac{3\overline{D}}{D}\right)^2 + \left(\frac{\overline{\Delta\theta}}{\Delta\theta}\right)^2 \tag{4.14}$$

The uncertainty interval in droplet diameter, $\bar{D}$, is treated in a subsequent paragraph and its calculation is given in Eqs. (4.15) and (4.16).

A summary of the uncertainty intervals for the fundamental components of the experimental measured quantities along with their sources are contained in Table II. Table III contains a summary of the calculated uncertainty intervals for a typical Fr-13-air experimental test run. The typical values selected were P = 38.2 atm (P_r = 1), u = u = 3 in./sec, T = 220° F, T_g = 70° F, D = 0.04 in., and T_L = -13° F.

Table II

Summary of Measurement Component Uncertainty Intervals

Quantity, x	Uncertainty, $\bar{x}$ (absolute)	Source
V	0.05 ft^3	1/2 of minimum scale division
θ	0.005 min	1/2 of minimum scale division
K_1	1 mv/v	Manufacturer's specifications
K_2	0.025 div/full range	1/2 of minimum scale division
K_3	1.5° R/v	Slope of t.c. cal. curve for probe
K_3	2.5° R/v	Slope of t.c. cal. curve for g.m. temp.
$\Delta\theta$	0.01 sec	1/2 of minimum readable timer scale division

Table III

Summary of Uncertainty Intervals Calculated for a Fr-13 Test

Quantity	Uncertainty absolute	Interval %	Comments
P	0.1 atm	0.3	Gauge mfg. spec.
V	0.05 ft^3/min	1.7	Calculated by Eq. (4.8)
u	0.2 in./sec	4.4	Calculated by Eq. (4.12)
T_L	1.5° R	3	Calculated by Eq. (4.10)
T_g	1° R	2.7	Calculated by Eq. (4.10)
T_∞	5.6° R	3	Calculated by Eq. (4.10)
D	0.00082 in.	2	Calculated by Eq. (4.16)
$dm/d\theta$	1.3×10^{-7} lb_m/sec	6.5	Calculated by Eq. (4.14)

The determination of the mean chord length of a droplet from film data was described in the previous section. The experimentally derived relationship between the droplet mean chord length and volume was shown on Fig. 14. The function was smoothed and fitted by a third order least squares fit through the 20 data points. The scatter in these data about the fitted function gives the deviation of the data from a mean value if the deviations are approximately normally distributed.

A test of the normality of the data is shown on Fig. 15 where the data is plotted on probability coordinates. Since the data falls in approximately a straight line which passes through the center, the distribution is symmetrical

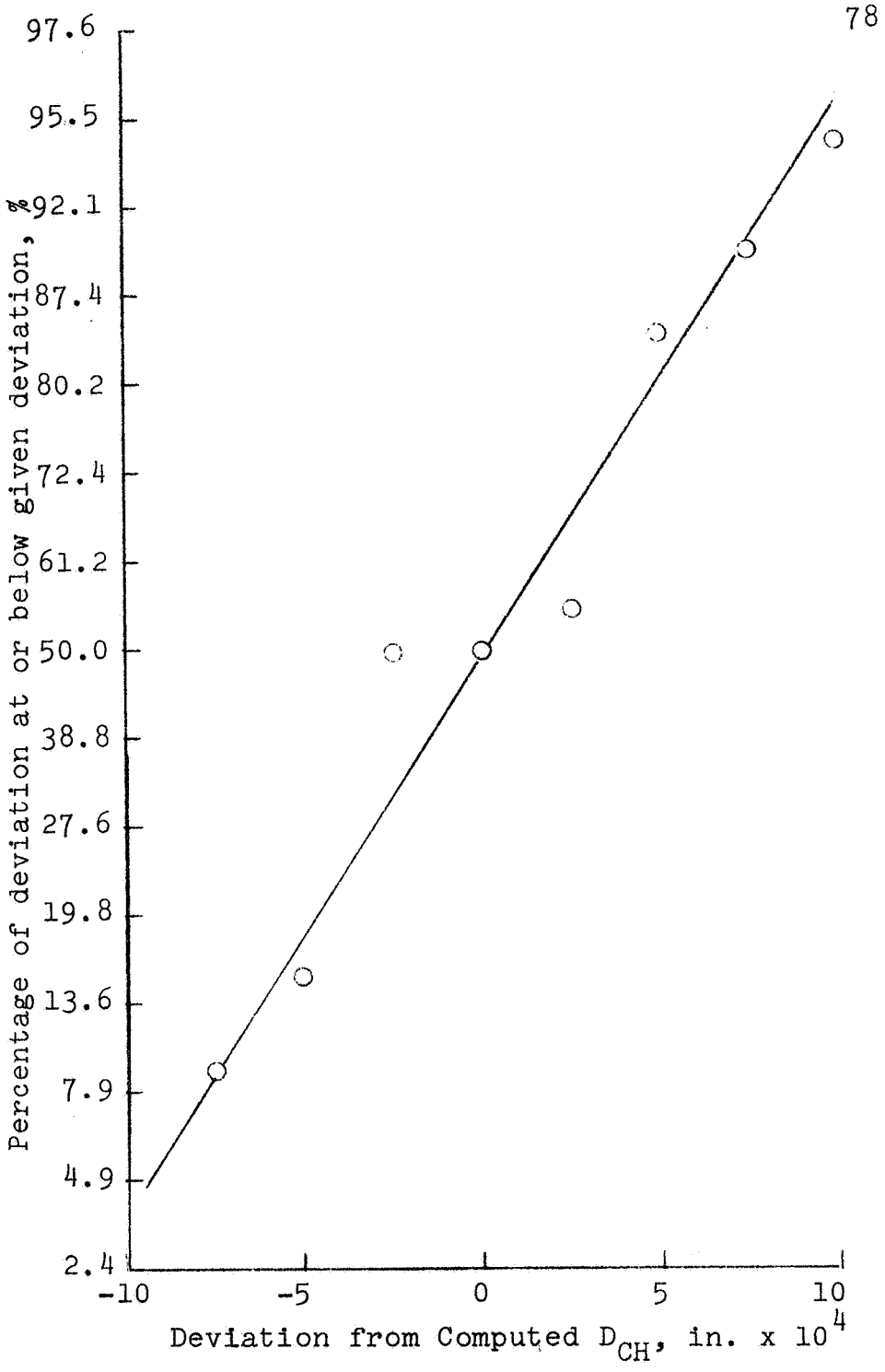

Fig. 15. Distribution of Measured Mean Chord Lengths From Least Square Values, Fr-13 Drop Data

and approximately normal (51). As a result Eq. (4.15) can be utilized to compute the standard deviation of the diameter measurement, σ_D.

$$\sigma_D = \left[\frac{\sum_{i=1}^{N} (x_L - \bar{x})^2}{N - 1} \right]^{1/2} \tag{4.15}$$

σ_D was calculated from the data and the fit is shown in Fig. 14 and found to be 5.76×10^{-4} in. Eq. (4.16) gives the relationship between the uncertainty interval, $\bar{x}$, and σ_D for the normal distribution.

$$\sigma_D = \frac{P(\bar{x})}{P(\sigma)} \bar{x} \tag{4.16}$$

where $P(\bar{x})$ and $P(\sigma)$ are the probabilities that a given deviation will fall within the uncertainty interval, $\pm \bar{x}$, and $\pm \sigma$, respectively. The results for the diameter uncertainty are also given in Table III.

Reflected Uncertainties in Calculational Comparisons

Comparisons between droplet history data and calculated droplet histories are presented in the following chapter. The calculated histories require values of independent variables which correspond to the experimental conditions of the test. The major dependent values which are calculated are the air-droplet temperature difference and the

droplet mass transfer rate. Uncertainties in the values of these independent variables, u, D, T_∞, and P, lead to uncertainties in the major dependent variables, $T_\infty - T_L$ and $dm/d\theta$. It is possible to estimate uncertainty intervals in these calculated variables.

Eq. (4.6) was stated in the previous section. It can also be applied to the steady state droplet calculations developed in Chapter II. The partial derivatives in Eq. (4.6) in this case are non-linear and complicated with respect to their dependence on x. Consequently, the $\partial R/\partial x$ values for $R = (T_\infty - T_L)$ and $dm/d\theta$ were determined by performing computer calculations of the change in the dependent variable, R, for small changes in the independent variables, x, about a base value.

The base conditions which are typical of the Fr-13-air data are: P = 38.2 atm (P_r = 1), u = 3 in./sec, $T_\infty = 220^\circ$ F, D = 0.04 in., and $T_L = -13^\circ$ F. The uncertainty intervals, $\pm \bar{x}$, for u, D, T, and P were given in Table III. A summary of the partial derivatives and the components of the computed dependent variable uncertainty intervals is given in Table IV.

The final total values of the uncertainty intervals are:

$$\overline{T_\infty - T_L} = 4.85^\circ \text{ R}$$

$$= 2.1\% \text{ of base case values and}$$

Table IV

Summary of Computed Uncertainty Intervals for
Air-Droplet Temperature Difference and Mass Transfer Rates

Independent Variable x	$\frac{\partial(T_\infty - T_L)}{\partial x}$	$\frac{\partial\left[\frac{dm}{d\theta}\right]}{\partial x}$	$\left[\bar{x}\ \frac{\partial(T_\infty - T_L)}{\partial x}\right]^2$ $^\circ R$	$\left[\bar{x}\ \frac{\partial \frac{dm}{d\theta}}{\partial x}\right]^2$ $lb_m/sec \times 10^{15}$
u	0.5°R-sec/in.	2.24×10^{-7} lb_m/in.	0.01	4.55
D	40° R/in.	8.28×10^{-5} lb_m/in.-sec	0.03	4.63
T_∞	0.865° R/$^\circ$R	6.17×10^{-9} $lb_m/^\circ$R-sec	23.5	1.18
P	-0.421° R/atm	1.97×10^{-8} lb_m/atm-sec	0.002	0.004
TOTAL UNCERTAINTY SQUARED			23.54	10.4

$$\overline{\frac{dm}{d\theta}} = 1.02 \times 10^{-7} \text{ lb}_m/\text{sec}$$

$$= 5.2\% \text{ of base case value.}$$

What these results mean is that for a typical case uncertainties in the measured values of the independent variables introduce uncertainties of $\pm 5^{\circ}$ R and $\pm 10^{-7}$ lb_m/sec, respectively, into the calculated temperature difference and mass transfer rates. These values can be translated to probable error which is the conventional method of reporting results. Probable error here is defined as the range in which one half of the reported values would be expected to lie. The probable error interval would be approximately 50% of the uncertainty interval, $\bar{x}$, and the computed results would be reported as $T_{\infty} - T_L \pm 2.5^{\circ}$ R and $dm/d\theta \pm 5 \times 10^{-8}$ lb_m/sec.

The other significant result of this analysis is that a good test of theoretical model would be to see if it consistently predicted results which agreed within the sum of the experimental and calculated uncertainty intervals. This would mean drop temperatures which agreed to within 13° R and mass transfer rates to within 23%.

V. EXPERIMENTAL RESULTS AND COMPARISONS WITH THEORY

This chapter contains a presentation of drop vaporization data for water, n-heptane and Freon-13 (Fr-13). The data are compared with film theory calculated results for plateau temperatures and vaporization rates. The Fr-13 temperature histories which exhibited non-classical behavior are correlated with the critical point of the gas mixture at the drop interface.

Water Drops Vaporizing in Air

A few temperature data points were obtained for water drops vaporizing in air at pressures of 20,40 and 60 atm abs. The water drop experimentation was undertaken for the purpose of testing the rig performance, and the data were previously reported by Alexander (2).

An initial series of tests was performed utilizing a copper-constantan probe thermocouple which had a 0.0185 in. diameter spherical bead and 0.005 in. diameter lead wires. For this series of tests the probe tip consisted of 22 gauge stainless steel hypodermic tubing instead of the teflon sleeve (described in Chapter III) which was installed later.

The copper-constantan probe thermocouple was replaced with an iron-constantan one of the same dimensions and the stainless probe tip was replaced with the teflon tube.

After these alterations were made, a second series of tests were made. The results of both tests are shown on Figs. 16, 17 and 18 for the test pressures of 20, 40 and 60 atm abs, respectively. The results of low pressure film theory calculations of plateau temperatures are also shown in the figures for comparison purposes.

Because of the relatively high surface tension of water, the drops clung to the probe tip instead of the thermocouple junction as was the case for n-heptane and Fr-13 drops. Initially, the drops were approximately 0.1 in. diameter, and they completely enveloped the thermocouple. Although the drop lifetimes were long, on the order of minutes, no mass transfer data were obtained. The plateau temperatures which were measured with a potentiometer were steady. No air flow conditions were recorded.

The 20 and 40 atm pressure results show that the probe alterations reduced the indicated wet bulb temperatures by about 15° F, and the corresponding reduction was 20° F for the 60 atm data. Since the lead wires were immersed in the drop for both series of tests, it is surmised that the substitution of the teflon for the stainless probe tip reduced the drop heat gain by conduction sufficiently to account for the difference.

The better data, which were obtained with the iron-constantan thermocouple arrangement, agree with the calculated plateau temperatures to within 10° F for all points.

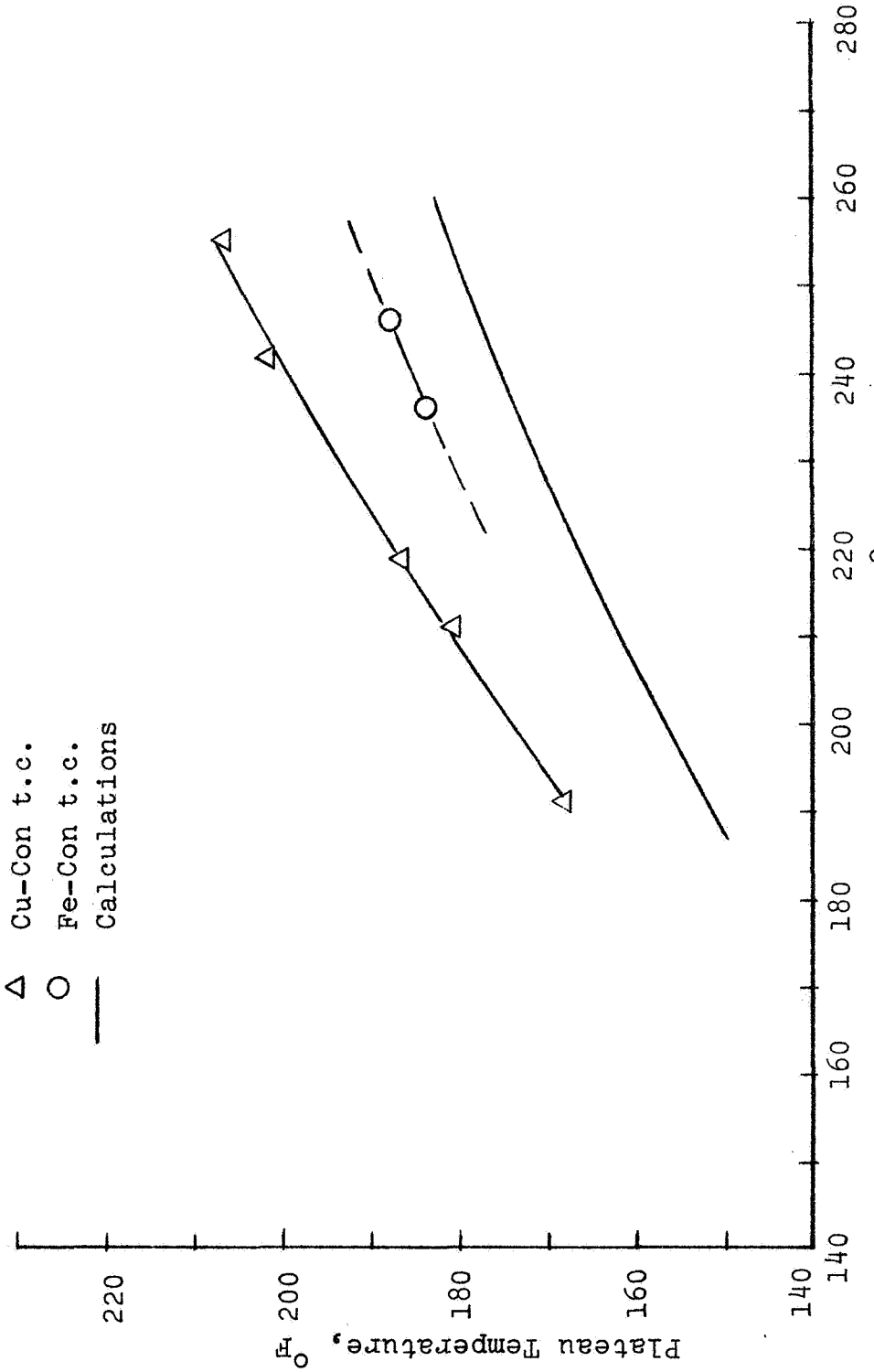

Fig. 16. Plateau vs Air Temperatures for Water Drops Vaporizing in Air at 20 atm abs

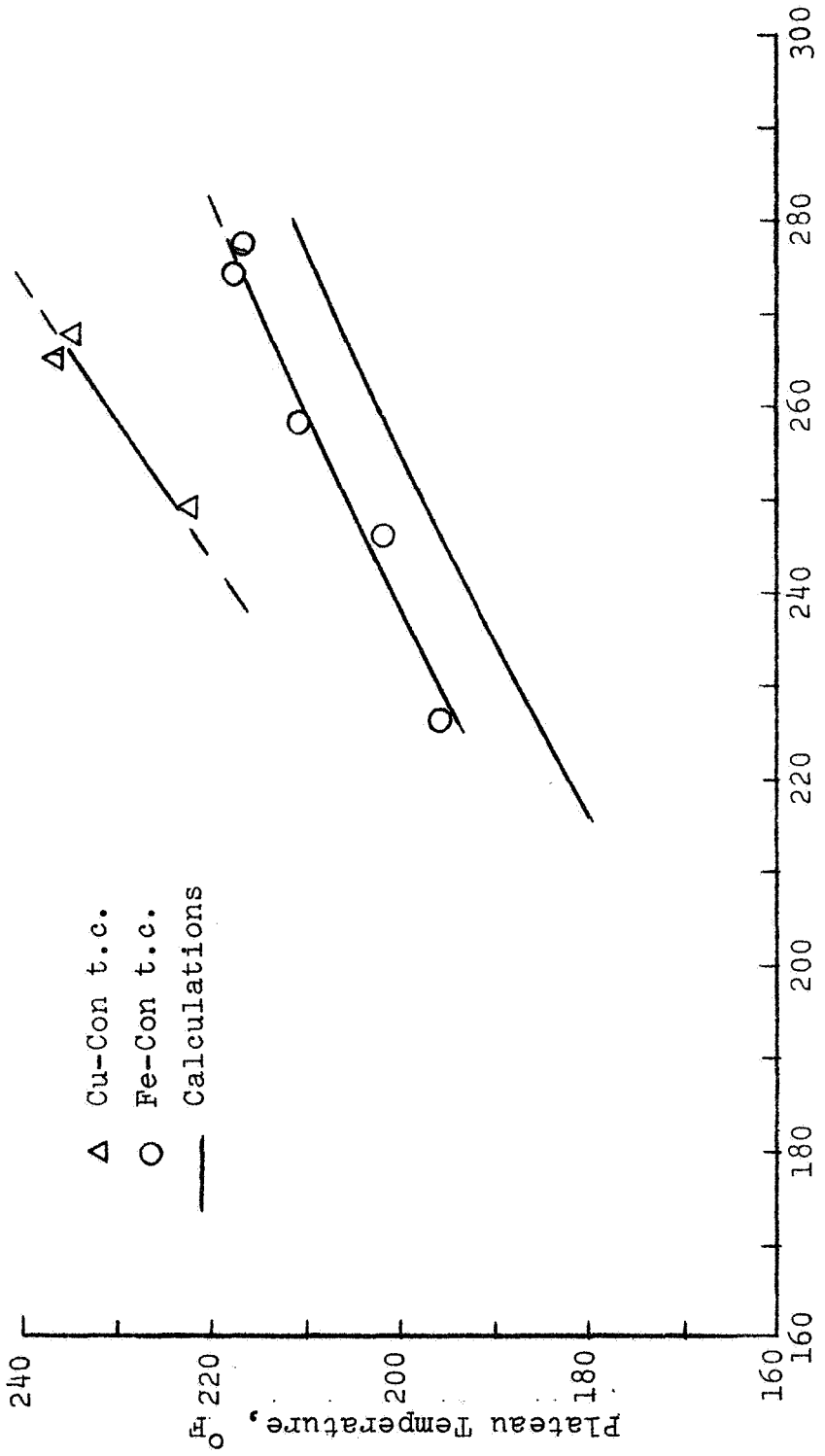

Fig. 17. Plateau vs Air Temperatures for Water Drops Vaporizing in Air at 40 atm abs

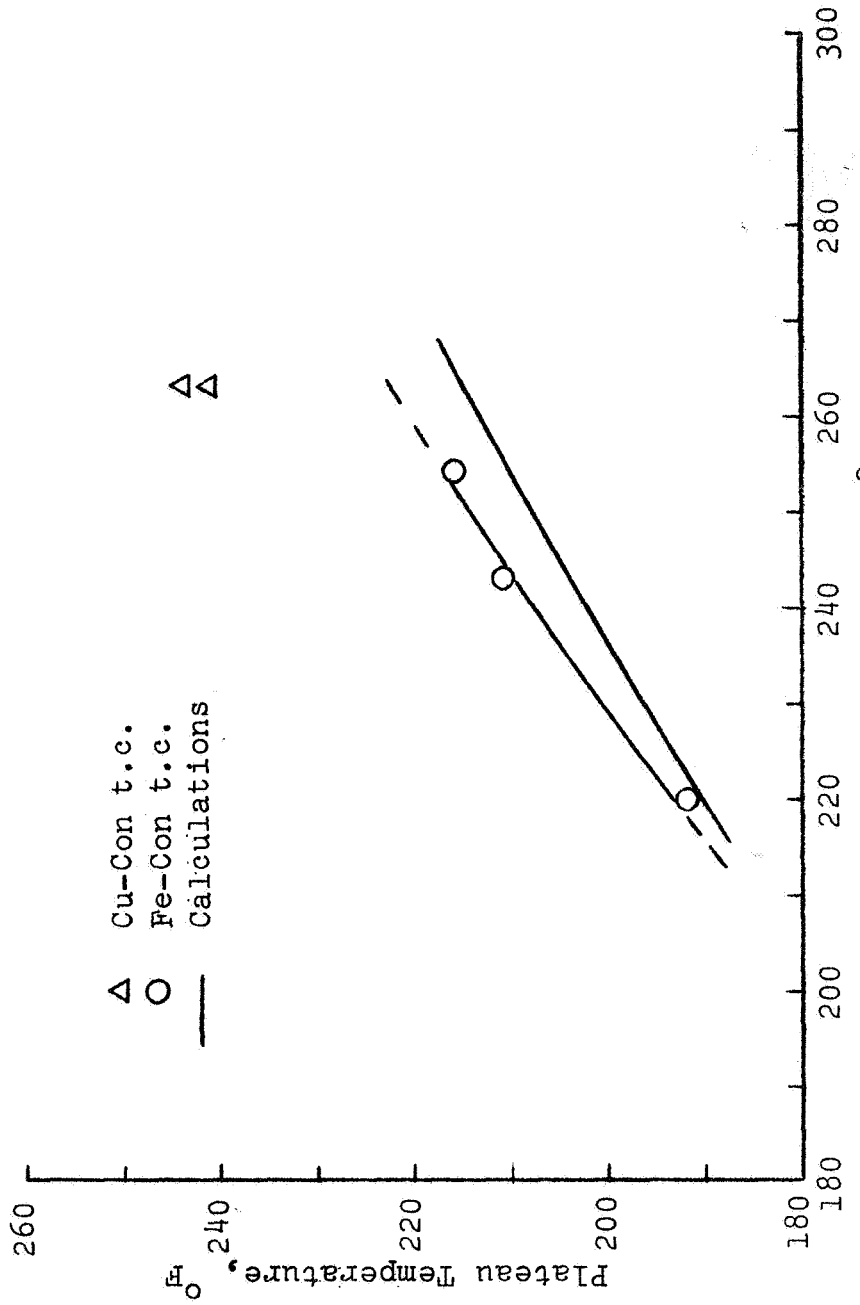

Fig. 18. Plateau vs Air Temperatures for Water Drops Vaporizing in Air at 60 atm abs

However, the calculated values are consistently lower. The agreement between the data and calculations seems to improve as the test pressure is increased although the data are too meager for a conclusive statement about the application of low pressure film theory to the data. The generally good agreement between the calculated and measured drop temperature was considered to be adequate for attesting satisfactory rig performance at high pressures.

N-Heptane Drops Vaporizing in Air

About 90 histories were recorded for n-heptane drops vaporizing in air at pressures of 1.5, 5, 10, 50 and 100 atm abs. The data covered a range of reduced pressures of 0.056 to 3.71 and reduced drop temperatures of 0.57 to 0.69 with respect to the critical properties of pure n-heptane. A chromal-constantan probe thermocouple with a bead diameter of 0.018 in. diameter and 0.005 in. diameter lead wires was used to obtain all n-heptane temperature data. All of the drop temperature histories displayed the typical behavior where the temperature initially sharply approaches the plateau or wet bulb temperature, levels out at the plateau value and slightly before the thermocouple is dry, begins to rise exponentially to the air temperature.

The minimum test section pressure which would produce adequate air velocities was about 1.5 atm abs. Consequently, it was not possible to make an exact comparison with

published vaporization data for n-heptane drops in air at atmospheric pressure. However, calculated plateau temperatures were compared with both calculated and measured values reported by Priem (44). The results of this comparison of atmospheric data and calculations are shown on Fig. 19. The agreement between the two calculated values is excellent both in magnitude and trend. The values calculated by the steady state technique outlined in Chapter II are consistently about 5° F higher than the experimental points of Priem. This agreement is within the experimental accuracy reported by Priem for 1 atm data.

A comparison between calculated plateau temperatures and measured values at the lowest system pressure investigated, 1.5 atm abs, is shown on Fig. 20. An air temperature range of 110-250° F is covered by the data. The agreement between calculated and measured values is within 10° F with a maximum scatter about a mean experimental fit of $\pm 5^{\circ}$ F. Calculated and measured plateau temperatures agree better at the higher air temperatures. A few data points taken on a different day from the bulk of the data shown on Fig. 20 are indicated by the triangles. The fact that these points fall generally in the range of the other data demonstrates self consistency of the data and experimental technique.

The difference between plateau temperatures calculated

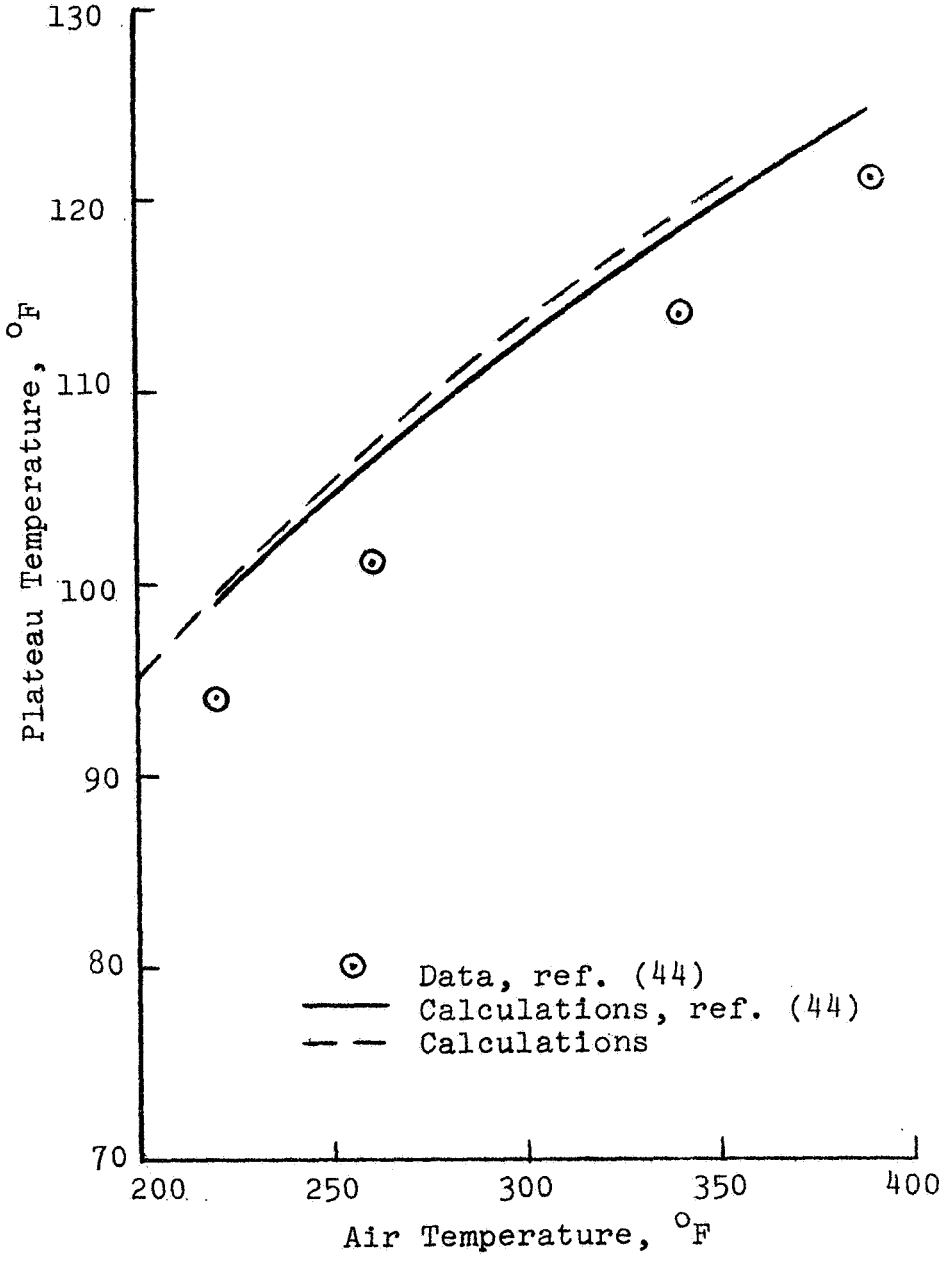

Fig. 19. Comparison Between Calculated Plateau Temperatures and Data of Priem, n-heptane Drops in Air at 1 atm abs

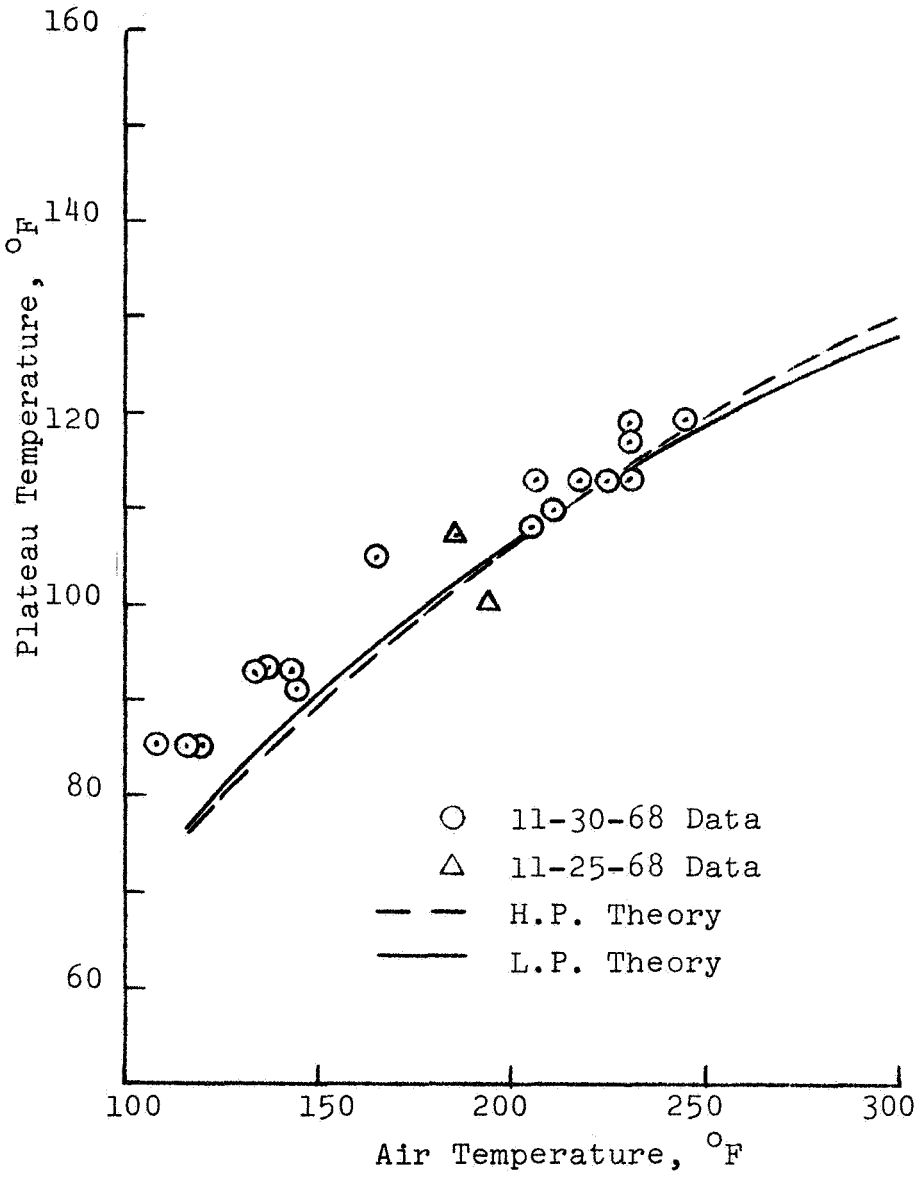

Fig. 20. Plateau vs Air Temperatures for N-Heptane Drops Vaporizing in Air at 1.5 atm abs

by low pressure film theory and film theory with the interface mole fraction and heat of vaporization corrected for pressure is almost indistinguishable at 1.5 atm. The high pressure film theory utilized in calculating n-heptane drop steady state temperatures and mass transfer rates included no corrections for surface regression or gas film thermal conductivity as in the case of the Fr-13 analysis.

Fig. 21 shows a comparison between calculated and measured plateau temperatures for n-heptane drops vaporizing in air at 5 atm abs. In the range of data shown, both the high and low pressure models agree with the data to within 5° F except at air temperatures above 250° F where both models predict plateau temperatures 8-10° F higher. The film theory calculations corrected for high pressure are 2-3° F closer to the measured values than the uncorrected theory for air temperatures above 250° F.

10 atm abs data is compared with high and low pressure film theory results on Fig. 22. The high and low pressure film theory results agree within 5° F over the range of the comparison. The lower plateau temperatures predicted by the high pressure theory fit the data better than the low pressure theory, although both theoretical results are in good agreement with the data.

A comparison of calculated and measured plateau temperatures of n-heptane drops vaporizing in air at 50 atm abs is shown on Fig. 23. This pressure is almost twice the

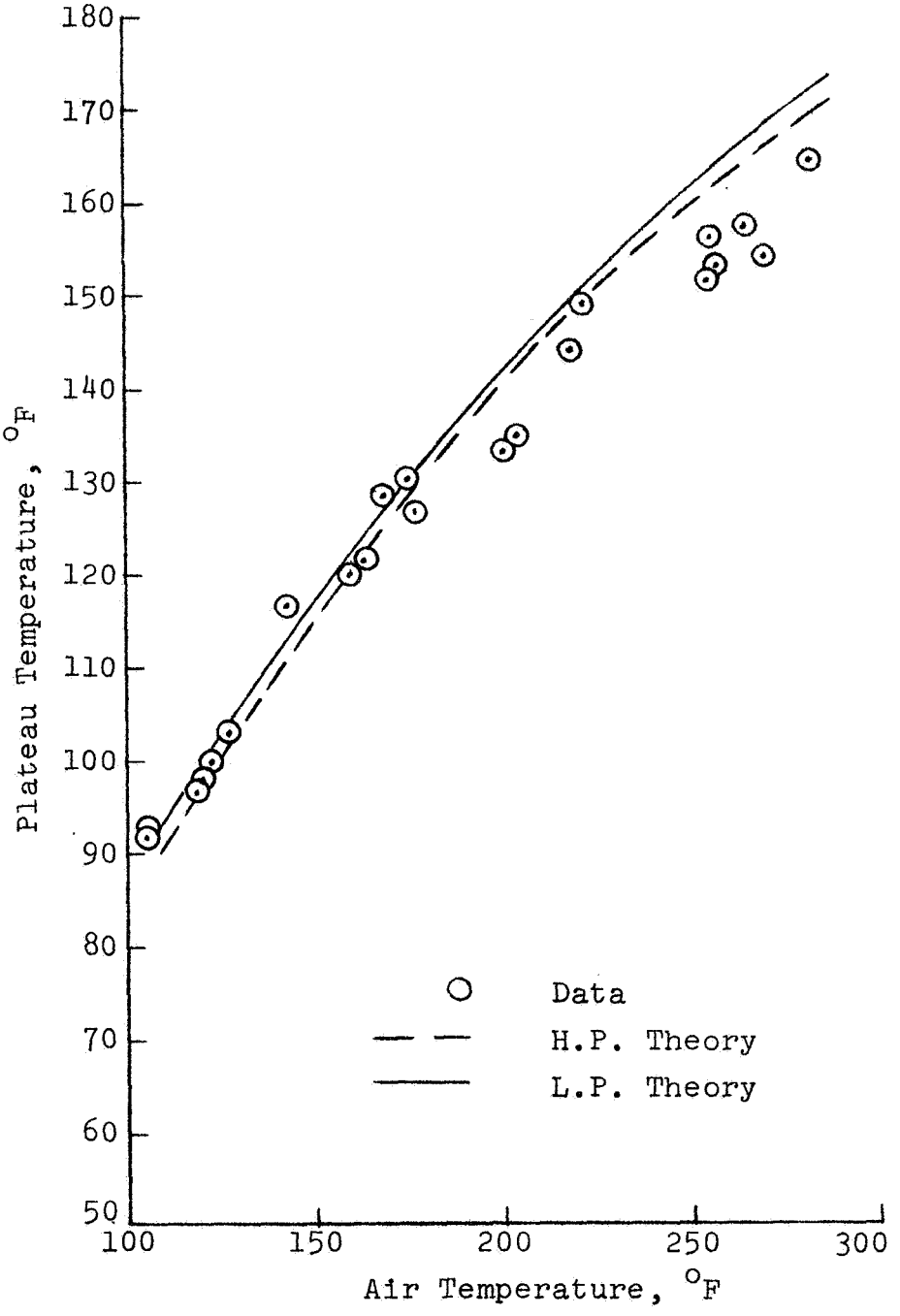

Fig. 21. Plateau vs Air Temperatures for N-Heptane Drops Vaporizing in Air at 5 atm abs

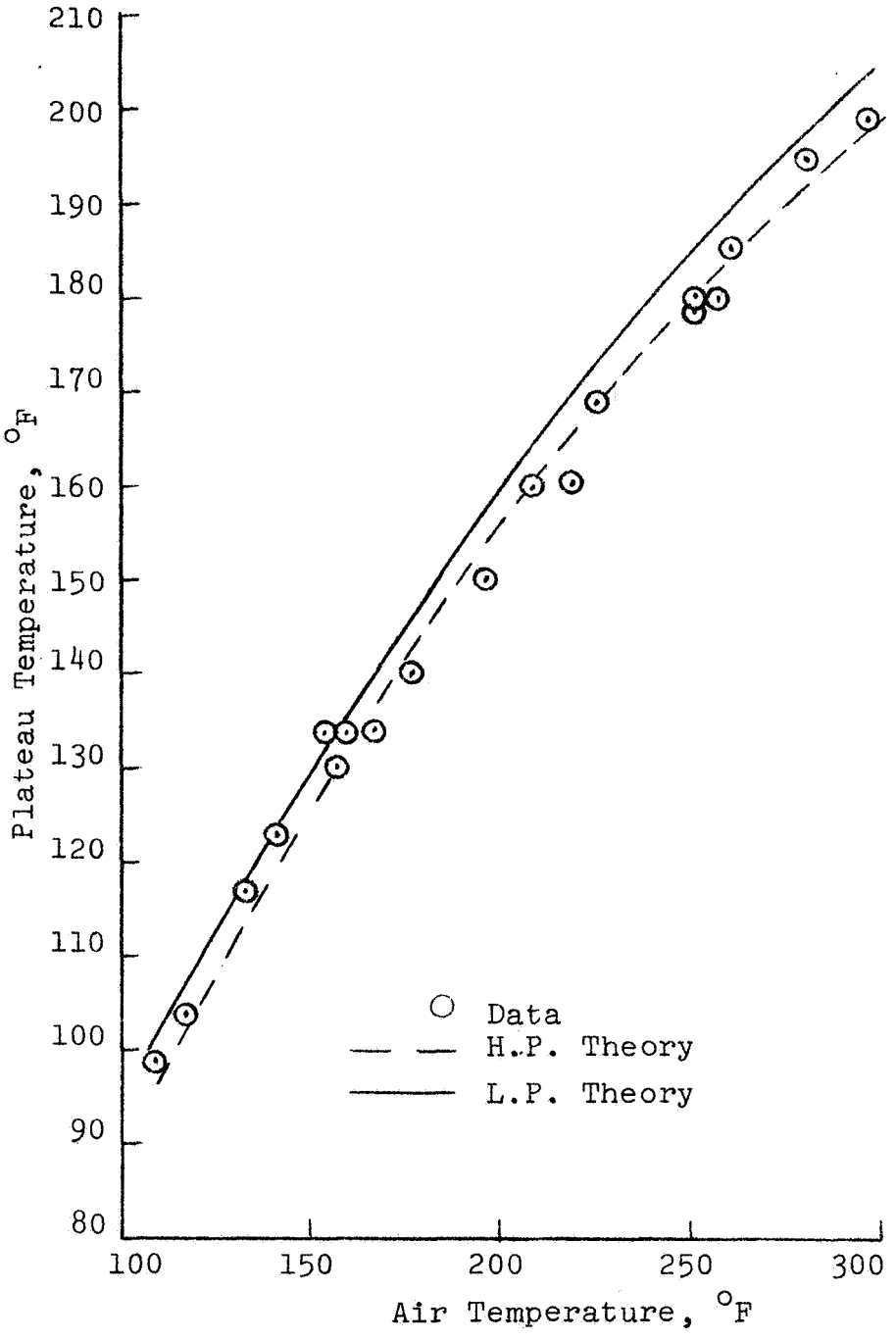

Fig. 22. Plateau vs Air Temperatures for N-Heptane Drops Vaporizing in Air at 10 atm abs

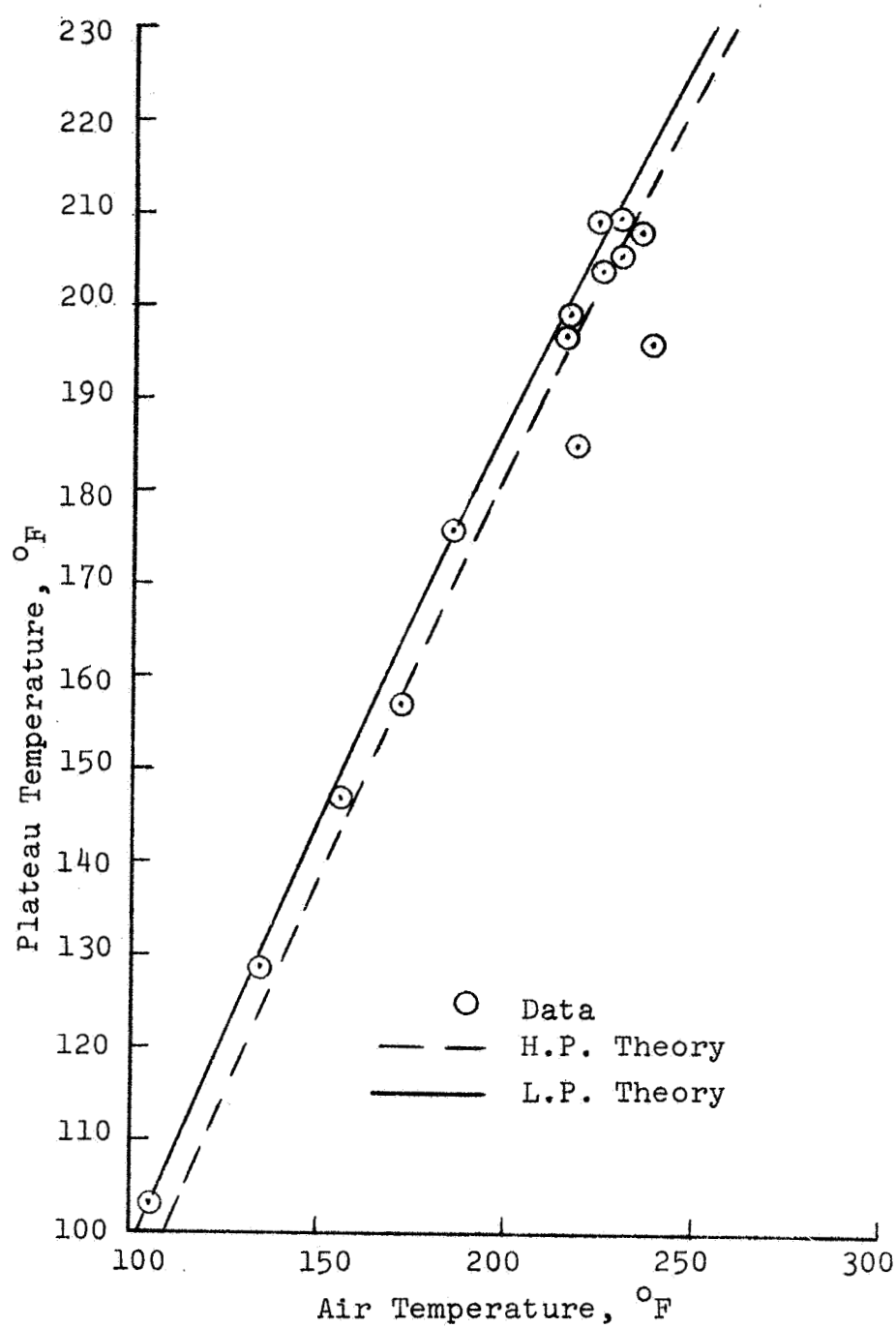

Fig. 23. Plateau vs Air Temperatures for N-Heptane Drops Vaporizing in Air at 50 atm abs

critical pressure of n-heptane. The shape of the droplet temperature histories at this supercritical pressure was similar to the data at the lower air pressures. The results calculated by either theory agree within 10° F of the measured values. The low pressure film theory calculated values show better agreement with the data.

Initially, all of the high pressure film theory calculations were based upon n-heptane interface mole fraction estimates obtained by the convergence pressure technique discussed in Chapter II. When the mass transfer rate comparisons were made, the high pressure film theory results consistently predicted mass transfer rates about 30% higher than the measured values for the 50 and 100 atm cases. This anomaly was subsequently traced to the high predicted n-heptane gas phase mole fraction at the drop-film interface. A comparison of the results of the convergence pressure calculation with measured values was shown on Fig. 2 for n-heptane-nitrogen mixtures at 100 atm. The predicted value of the n-heptane gas phase mole fraction was about 40% higher than the data for the highest temperature point (388° K = 240° F).

The problem of inaccurate calculated mole fractions was resolved by using the n-heptane-nitrogen vapor-liquid equilibrium data in lieu of calculated values for the film theory vaporization calculations at 50 and 100 atm. The mole fractions calculated by the convergence pressure

method at 100 atm were appoximately 20% higher than those calculated at 50 atm and the y_{Ao} values were equal at 260° F for 100 and 50 atm. Consequently, the 100 atm vapor-liquid equilibrium data were used unaltered in the 50 atm calculations. That this procedure is more satisfactory than using the calculated values for all pressures is borne out by the resulting mass transfer comparisons which are presented in the latter part of the section. The use of accurate values for the interface mole fraction at 50 atm, if they were available, would be expected to produce higher calculated plateau temperatures than those shown on Fig. 23 and hence, probably better agreement.

Calculated and measured plateau temperature results at 100 atm abs are compared on Fig. 24. The temperatures predicted by steady state film theory corrected for high pressure agree within 5° F for all data points except the highest which is about 10° F high. The low pressure theory results agree well with the data too, although they appear to be consistently a few degrees higher than the average data values.

Fig. 25 shows a summary of the plateau temperature data at all pressures. The lines representing the temperature data are least squares fits of the data points. The slopes of the plateau versus air temperature functions steepen as the pressure increases, and they approach the plateau equal to air temperature line as an asymptote as

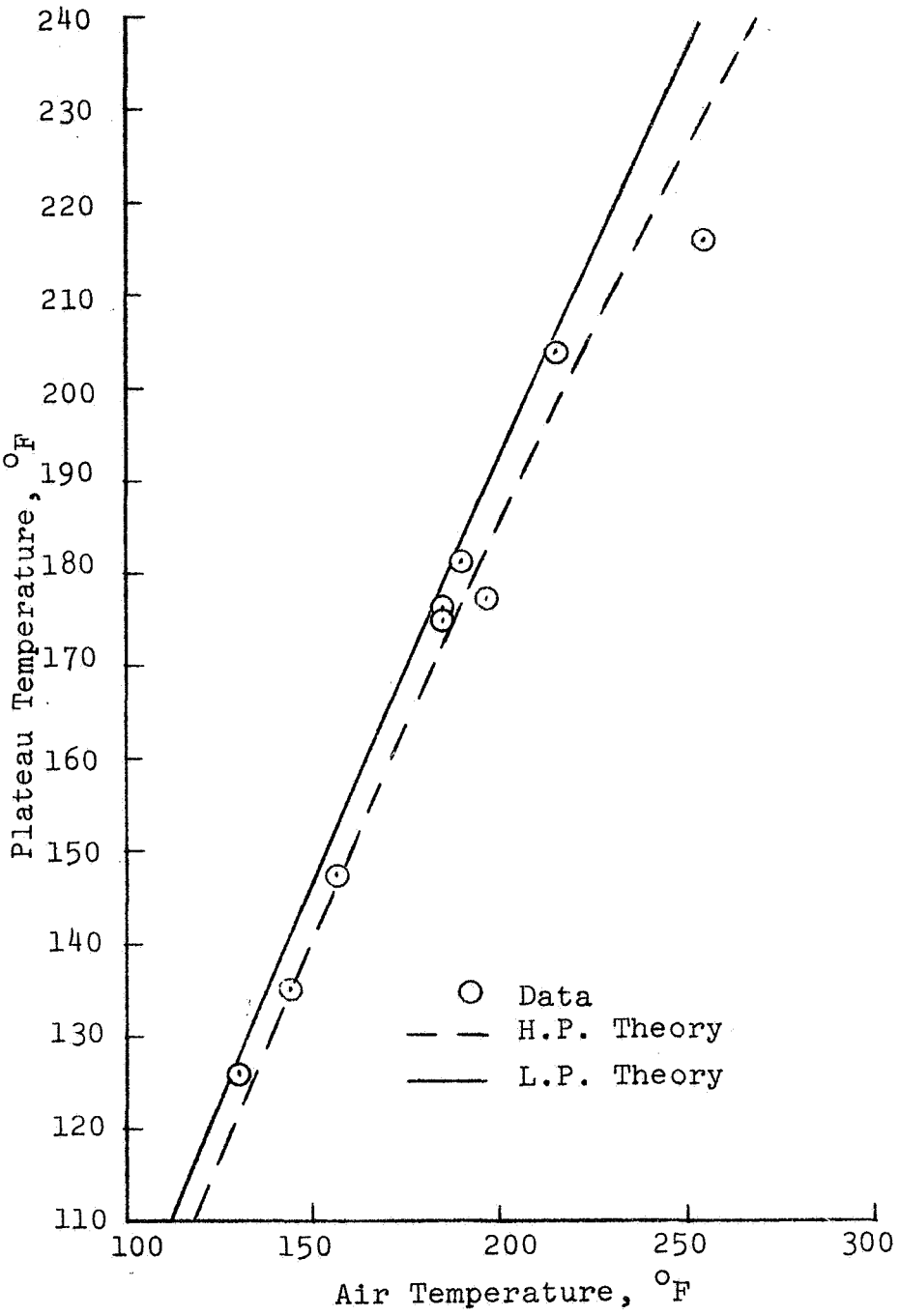

Fig. 24. Plateau vs Air Temperature for N-Heptane Drops Vaporizing in Air at 100 atm abs

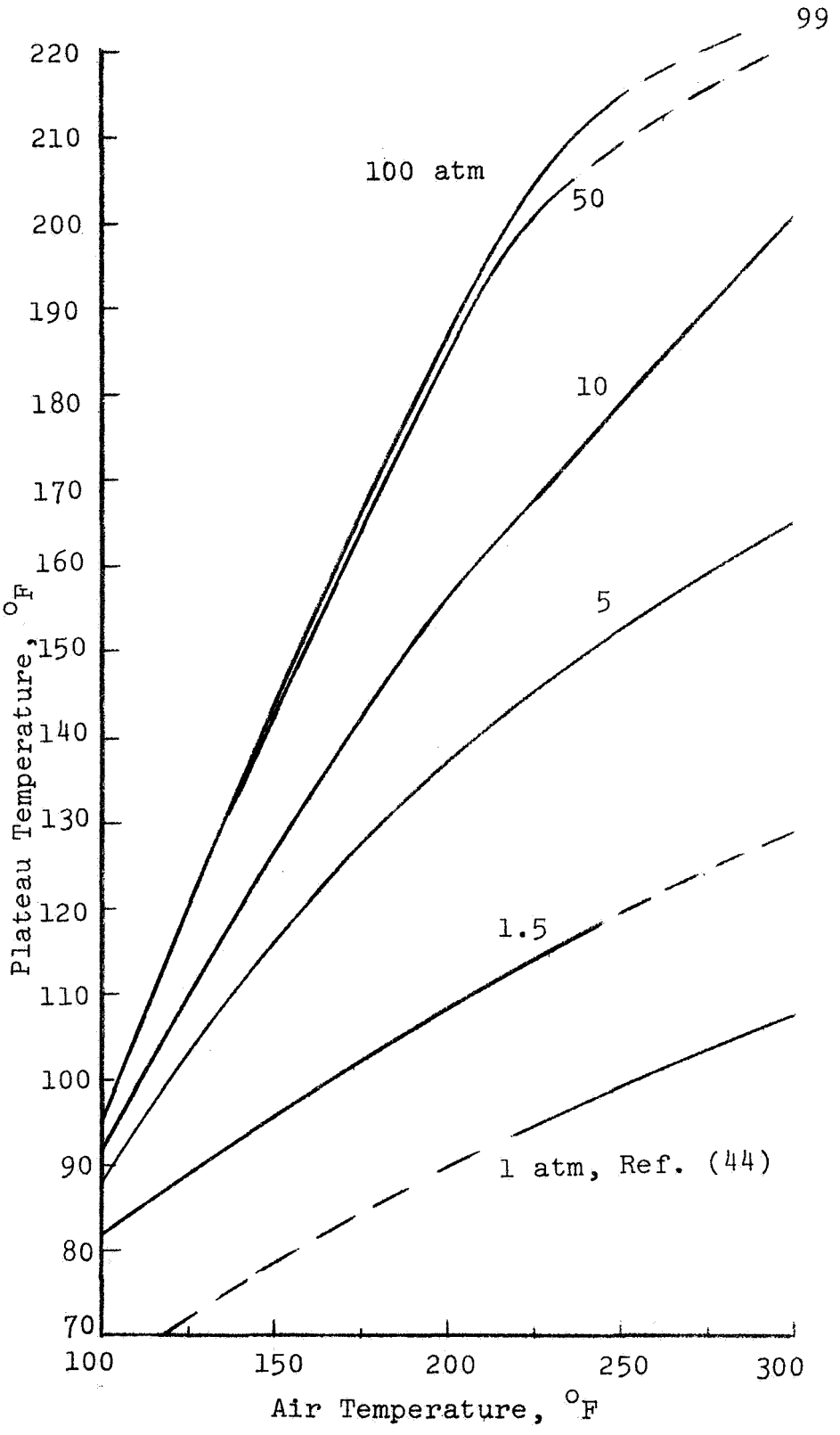

Fig. 25. Summary of N-Heptane Temperature Data

the pressure increases. The knee in the plateau versus air temperature curves shifts in the direction of higher air temperature as the system pressure is increased. This effect of pressure for a given fuel is analogous to the effect of going from less to more volatile fuels at a given pressure (44).

The data represented on Fig. 25 are shown cross plotted versus pressure on Fig. 26 for air temperatures of 100, 175 and 250° F, respectively. The slope increases with increasing air temperature although the lines appear to flatten at the highest pressures. They would most likely approach the air temperature as a limit at very high pressures.

The effect of pressure upon the two film theory predictions is represented on Fig. 27 where the predicted drop temperature minus the measured plateau temperature is plotted versus pressure for an air temperature of 175° F. The measured plateau temperatures are least square fitted values. Temperature errors are within $\pm$ 6° F for both theories at all pressures. The low pressure film theory error exhibits a tendency to increase with increasing pressure.

Several individual droplet histories were analyzed for mass transfer rates in the manner described in Chapter IV. In order to obtain instantaneous mass transfer rates, the drop volumes at several different times during the history were plotted versus time. A tangent to the volume time

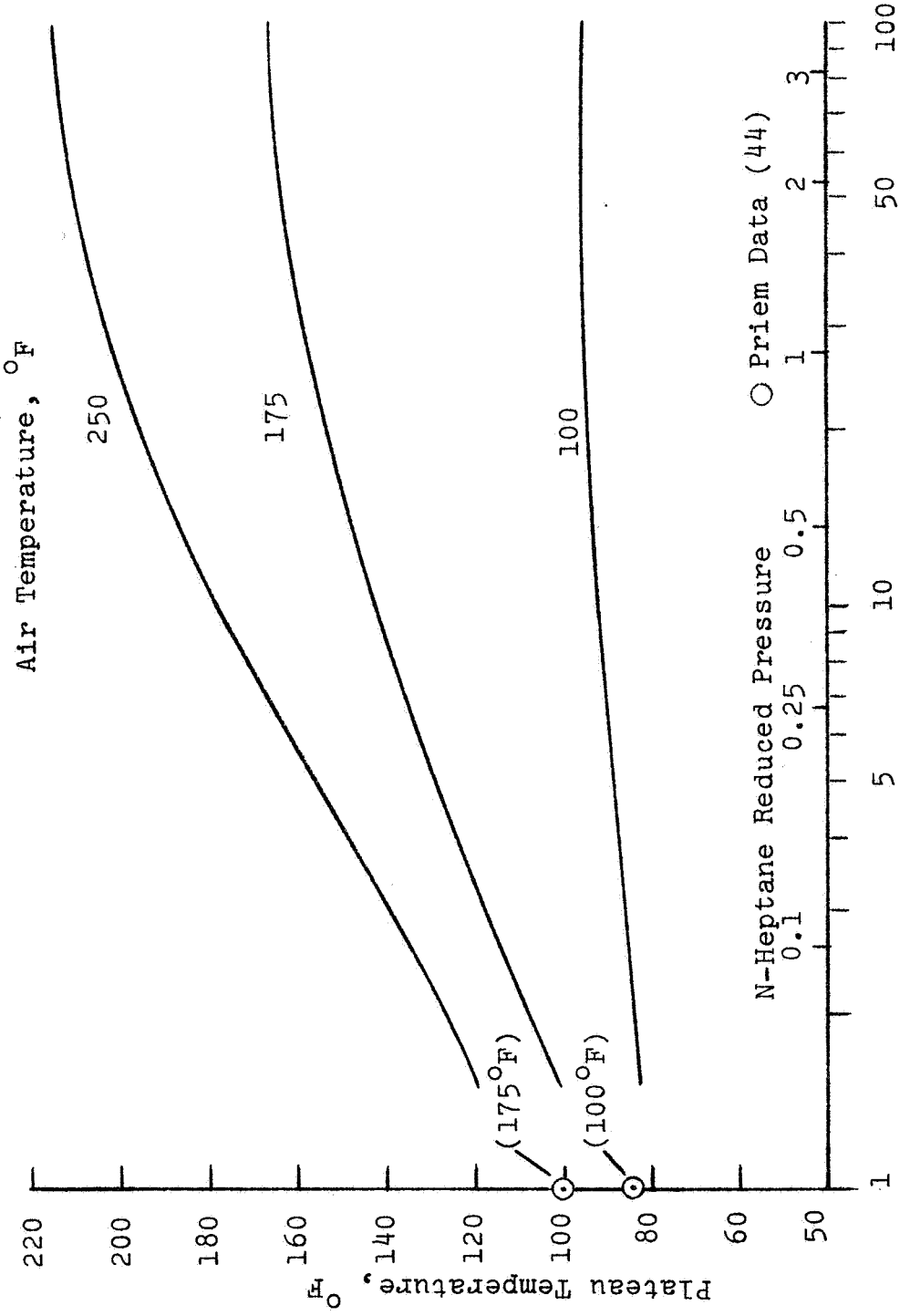

Fig. 26. Summary of N-Heptane Temperature Data, Shown vs Pressure for Air Temperatures of 100, 175 and 250°F

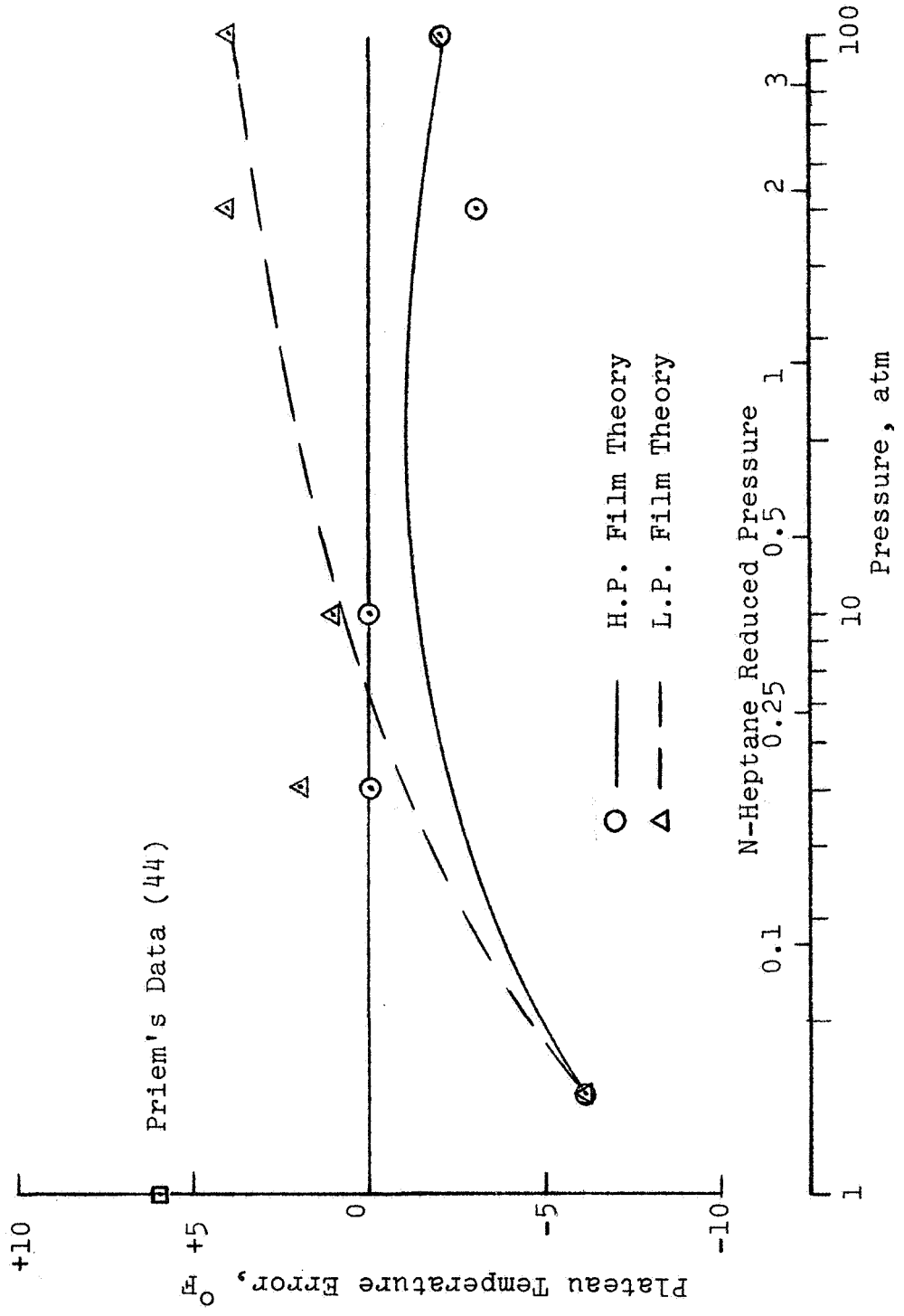

Fig. 27. Effect of Pressure on Calculated Plateau Temperature Error for N-Heptane Drops Vaporizing in Air at 175°F

curve was measured at the particular point desired. Care was taken to pick points which occurred during the distinct plateau region of the temperature history since comparisons were to be made with steady state calculations.

The data were subjected to the following criteria, and only data which met it were analyzed for mass transfer rates. A Nusselt number was computed using film properties based upon an average of the measured drop and air temperatures and the measured test section flow rate. This value of the Nusselt number, Nu_{calc}, computed from the Ranz-Marshall correlation was compared with an experimentally determined Nusselt number, Nu_{exp}. The experimentally determined Nusselt number is calculated from Eq. (5.1)

$$Nu_{exp} = \frac{\lambda \frac{dm}{d\theta}}{\pi D(T_\infty - T_L)\, k} \tag{5.1}$$

where

λ = the heat of vaporization of the liquid

D = drop diameter

$\frac{dm}{d\theta}$ = measured mass transfer rate

T_∞ = measured air temperature

T_L = measured drop temperature

k = average film thermal conductivity.

Eq. (5.1) is simply a rearrangement of the energy balance for the drop in which the heat transfer coefficient is given in terms of the Nusselt number. The criterion is that only

data which gives a ratio of Nu_{calc}/Nu_{exp} within the range 0.85-1.15 will be analyzed for mass transfer rates. This excluded about one half of the data analyzed.

Data points which met the criteria are shown on Fig. 28. They are plotted versus drop Reynolds number, and they appear to be randomly scattered about a value of unity.

Fig. 29 shows the calculated mass transfer rate error versus Reynolds number for the data points analyzed. The calculated values are the results of steady state film theory corrected for high pressure as discussed above in this section. The corresponding pressures are indicated for each point. All of the points fall within a 30% error band although the average error is -9.1%. There appears to be a systematic trend with Both Reynolds number and pressure. It is expected that the 50 atm calculated points may be high with respect to the 100 atm ones due to the use of 100 atm interface mole fraction data for both pressures.

Two explanations of these results are tendered. The first is the use of the Ranz-Marshall correlation for drop Reynolds numbers above 450. Hugmark (25) recommends a slightly different correlation for heat and mass transfer in the range of Reynolds number of $450 < Re < 10{,}000$ which he claims gives a better fit to the data he analyzed. The use of Hugmark's correlation would lower the three data points which have $Re > 450$ by about 5%. This would improve the consistency of the data somewhat, but it would also

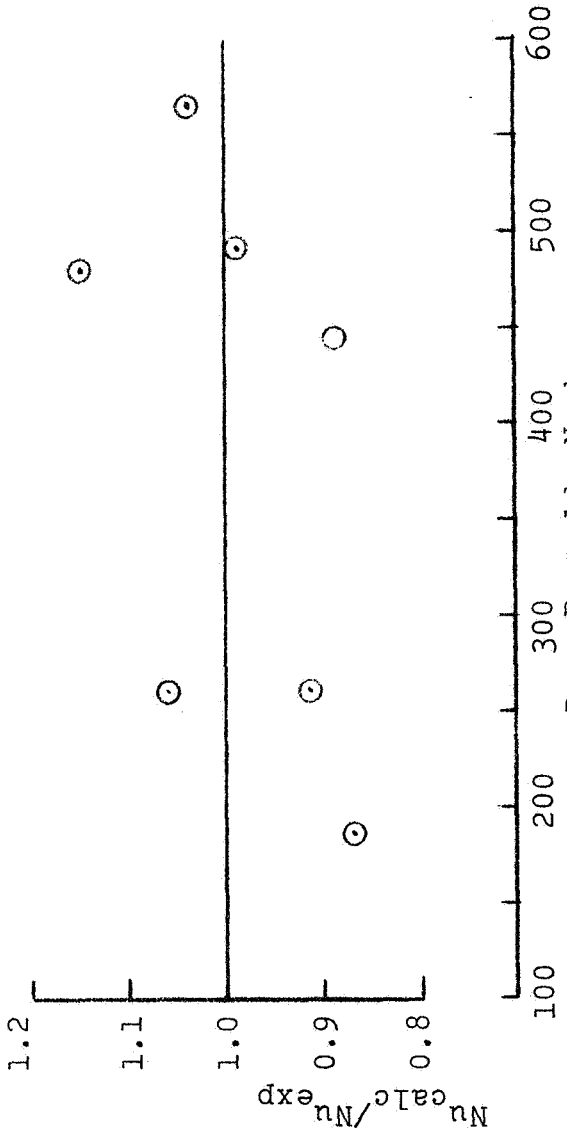

Fig. 28. Variation of Calculated to Measured Nusselt Number Ratio With Reynolds Number for N-Heptane Drop Data

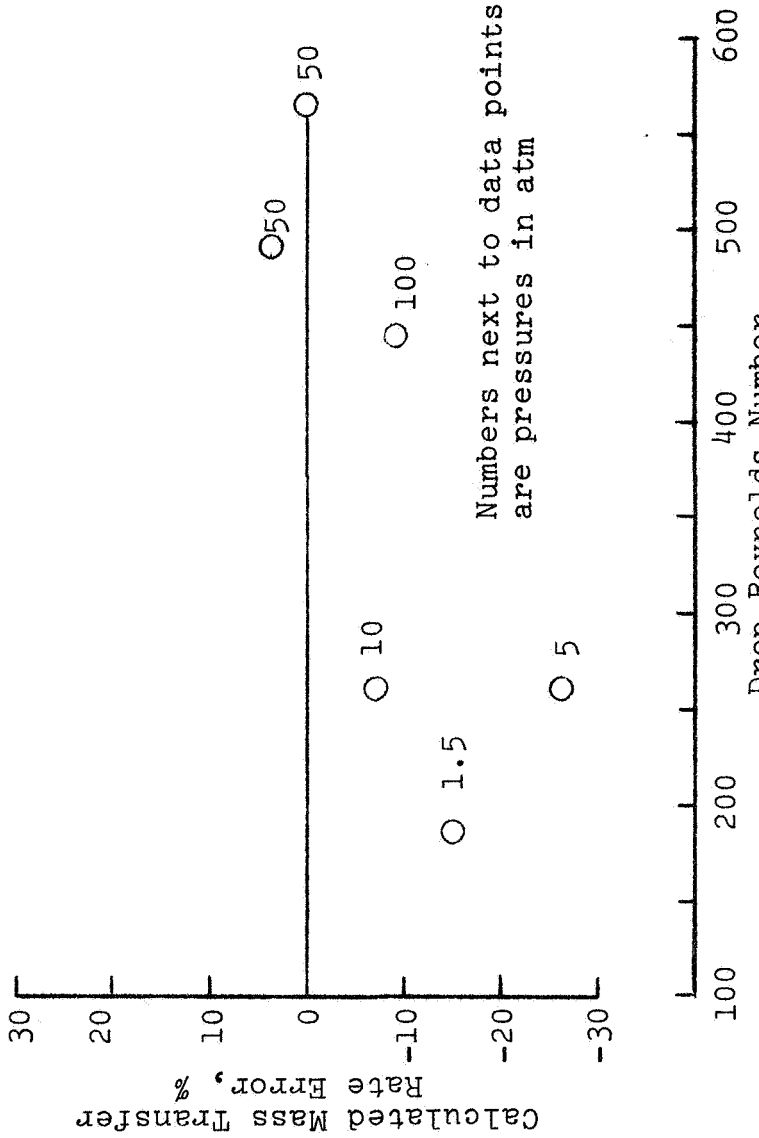

Fig. 29. Variation of Calculated Mass Transfer Error with Reynolds Number for N-Heptane Drop Data

increase the average error from -9.1% to about -11%.

The second explanation for the results shown on Fig. 29 is the influence of drop shape on mass transfer. The low Reynolds number drops are slightly more pendant shaped than the drops with higher Reynolds numbers. The higher drag force associated with higher Reynolds numbers tends to mitigate the deformational effects of gravity since the drag force opposes the gravitational force. Using the correlations of Hsu, Sato and Sage (24) for estimating the influence of drop shape on evaporation rates, two trends are evident. The first is that the calculated mass flow rates at all Reynolds numbers would be 5-10% higher using the Hsu, Sato and Sage results, and the second is that the corrections due to drop shape would be somewhat greater at the low Reynolds numbers due to greater drop deformation.

Considering the paucity of data on Fig. 29 and the lack of Reynolds number overlap of points at different pressures, the explanation given, although plausible, is considered provisional.

Once the mass transfer data was screened by the Nusselt number criteria, the effect of pressure was investigated. The results of a comparison of calculated mass transfer error versus pressure is shown on Fig. 30. This result is based upon the 7 data points shown on Fig. 29. There are two 100 atm histories, two 50 atm histories, and one each at pressures of 10, 5 and 1-1/2 atm abs. The film

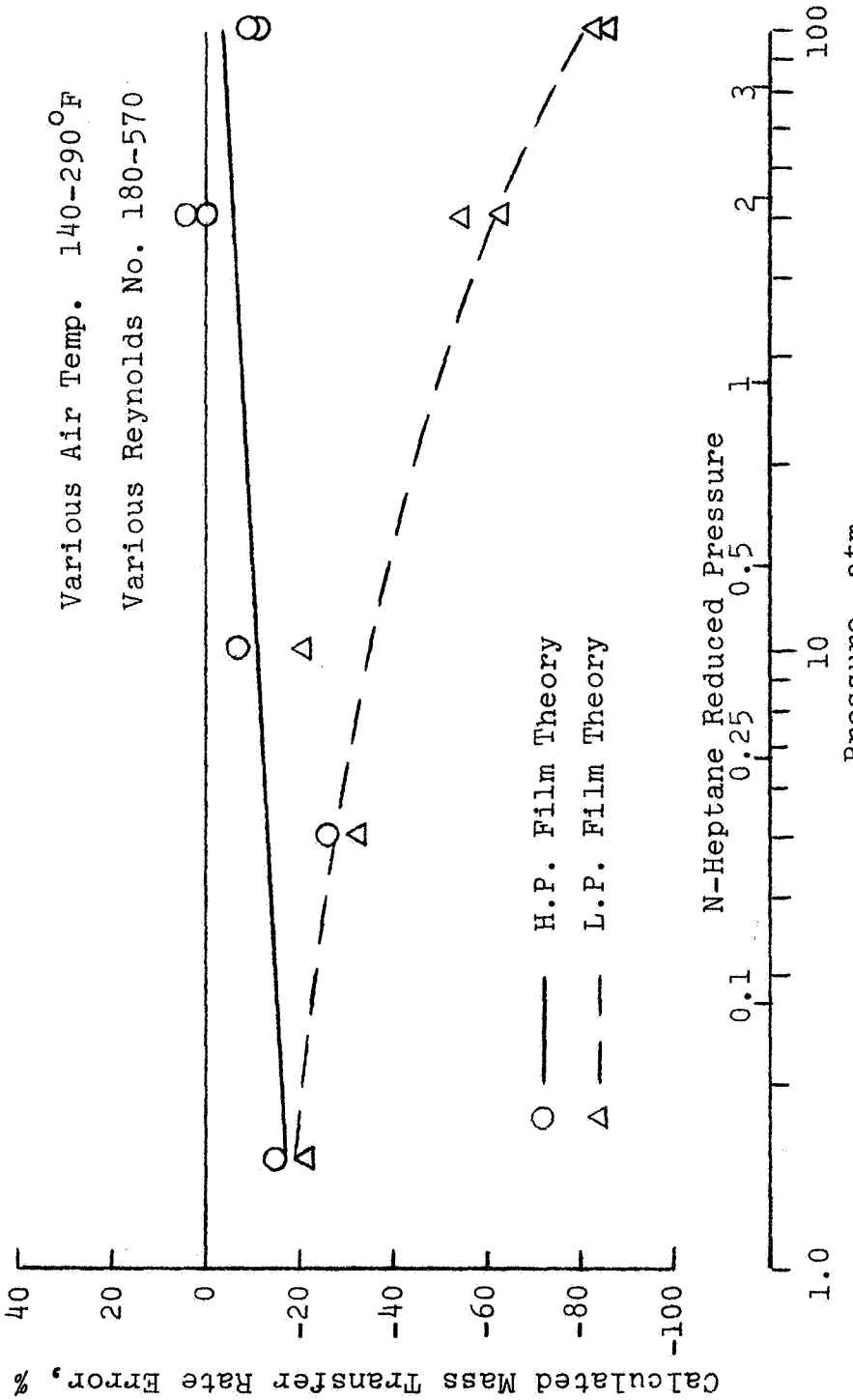

Fig. 30. Effect of Pressure on Calculated Mass Transfer Error for N-Heptane Drops Vaporizing in Air

theory with low pressure assumptions increasingly underestimates mass transfer rates as the pressure is increased. At a pressure of 100 atm (reduced pressure of 3.7), low pressure film theory underestimates the mass transfer rates by 80%. The high pressure film theory greatly improves the predicted mass transfer rates at high pressures showing an error of only -10% at 100 atm.

The high pressure film theory shows a small improvement with increasing pressure with all the results within 18% of the measured values. Over the range of data considered the high pressure film theory mass transfer predictions are about 10% low on the average.

Fr-13 Drops Vaporizing in Air

Approximately 50 individual histories of Fr-13 drops vaporizing in air at reduced pressures of 0.75, 1.0, 1.25, 1.5 and 1.75 were obtained experimentally. Most of the data exhibited the classical temperature behavior. The drop temperature initially passes from the feed to the plateau temperature, resides at the plateau temperature until the thermocouple becomes almost dry, and then rises exponentially to the air temperature. At the higher pressures a few non-classical temperature histories were recorded. All of the data reported here was obtained with a chromal-constantan probe thermocouple which had a junction diameter of 0.014 in. and 0.003 in. diameter lead wires.

Plateau temperatures as a function of air temperature are shown on Fig. 31 for a reduced pressure of 0.75 (28.65 atm abs). Calculated values are given for film theory corrected and uncorrected for high pressure. The calculated results were obtained by steady state calculations. The high pressure film theory contained corrections which are summarized in the following list:

1. Gas phase drop interface mole fractions were calculated by the phase equilibrium constant method.
2. Fr-13 heat of vaporization values were calculated by gas and liquid phase partial molal enthalpy deviations.
3. A first order surface regression correction was introduced in the form of the air to Fr-13 mass flux ratio.
4. Film thermal conductivity was corrected for high pressure by a correlation of Lenoir, Junk and Comings (34).

The high pressure film theory underestimates the plateau temperature by about 15° F while the uncorrected film theory produces only a -10° F error at the higher air temperature.

A series of steady state calculations which show the effects of the various corrections were performed for $P_r = 1$, $T_\infty = 200^{\circ}$ F, u = 3.7 in./sec and a diameter of 0.025 in. Table V contains the results of these calculations. The

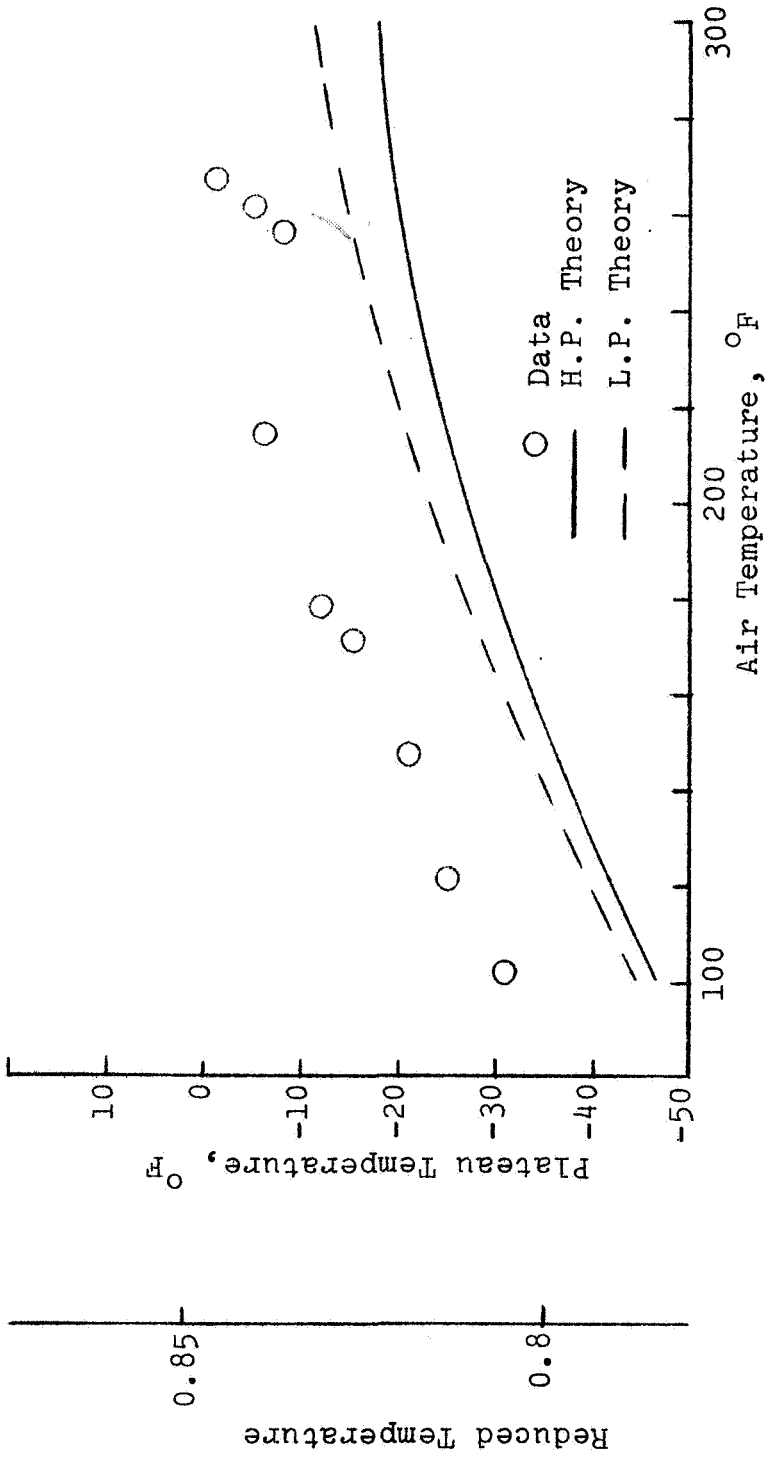

Fig. 31. Plateau vs Air Temperature for Fr-13 Drops Vaporizing in Air at $0.75P_c$

experimental plateau temperature resulting from a least square fit to the data is included for comparison. The major contributing correction to increasing the mass transfer rate is the one for surface regression. The thermal conductivity pressure correction is the second most important correction from the mass transfer point of view. It increases the mass transfer rate by half as much as the surface regression correction does. Following the low pressure results, the cases listed in the table correspond to the order of the list of corrections in the list above. At higher pressures the thermal conductivity correction becomes the major factor affecting the mass transfer.

Table V

Effect of Various High Pressure Corrections on Steady State Film Theory Calculated Results for Fr-13-Air

Description	Calculated Plateau Temp. (^{o}F)	Normalized Mass Trans. Rate
L. P. film theory	-9	0.820
Film theory (y_{Ao})	-28	0.736
Film theory (y_{Ao}, λ)	-22	0.601
Film theory (y_{Ao}, λ, N_R)	-20	0.885
H.P. film theory (y_{Ao},λ,N_R,$k^{\#}$)	-15	1.000

Fig. 32 shows similar results for a reduced pressure of 1 (28.2 atm abs);as in the case of P_r = 0.75, the low

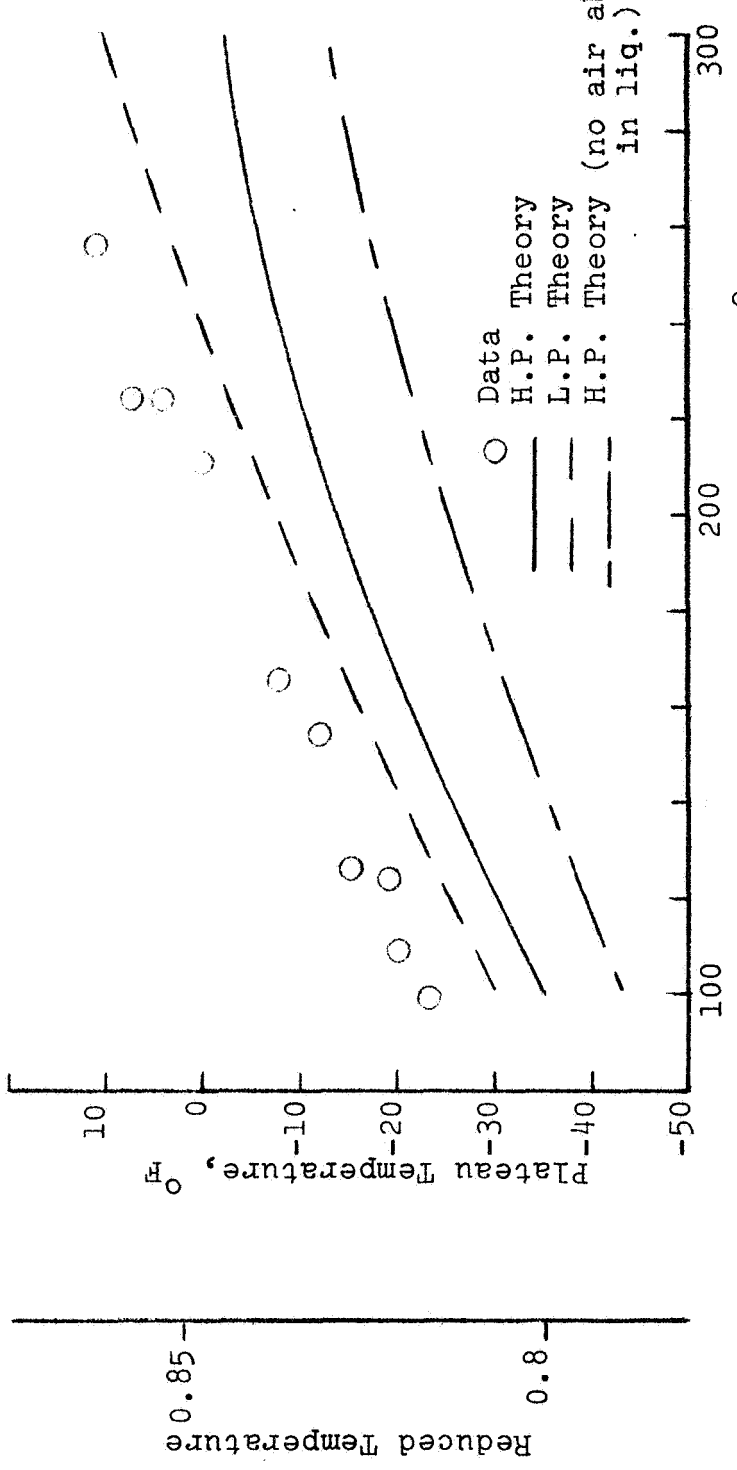

Fig. 32. Plateau vs Air Temperature for Fr-13 Drops Vaporizing in Air at P_c

pressure film theory gives the best results although typical plateau temperature predictions are 5° F low. High pressure film theory predicted plateau temperatures are about 10° F low. The results for a third calculation with all of the high pressure corrections enumerated above except for thermodynamic equilibrium at the interface are shown on Fig. 32. The phase mole fractions for this case were calculated by the phase equilibrium constant method, but no air absorption in the liquid phase was allowed. The Fr-13 gas phase mole fractions were found to be about 25% higher and the enthalpy of vaporization values 10% lower than the equilibrium values. This assumption gave predicted plateau temperatures generally 20° F too low compared with the measured values.

A comparison between high and low pressure theory and experimental plateau temperatures is shown on Fig. 33 for a reduced pressure of 1.25 (47.8 atm abs). Both calculations predict temperatures about 12° F low. However, the low pressure theory gives slightly better agreement with the measured values at the higher air temperatures.

Plateau temperature results of measurements and low and high pressure film theory calculations at a reduced pressure of 1.5 (57.4 atm abs) are compared on Fig. 34. There is very little difference between the plateau temperatures calculated by either theory. Both theories predict temperatures which are about 10° F low. At air temperatures

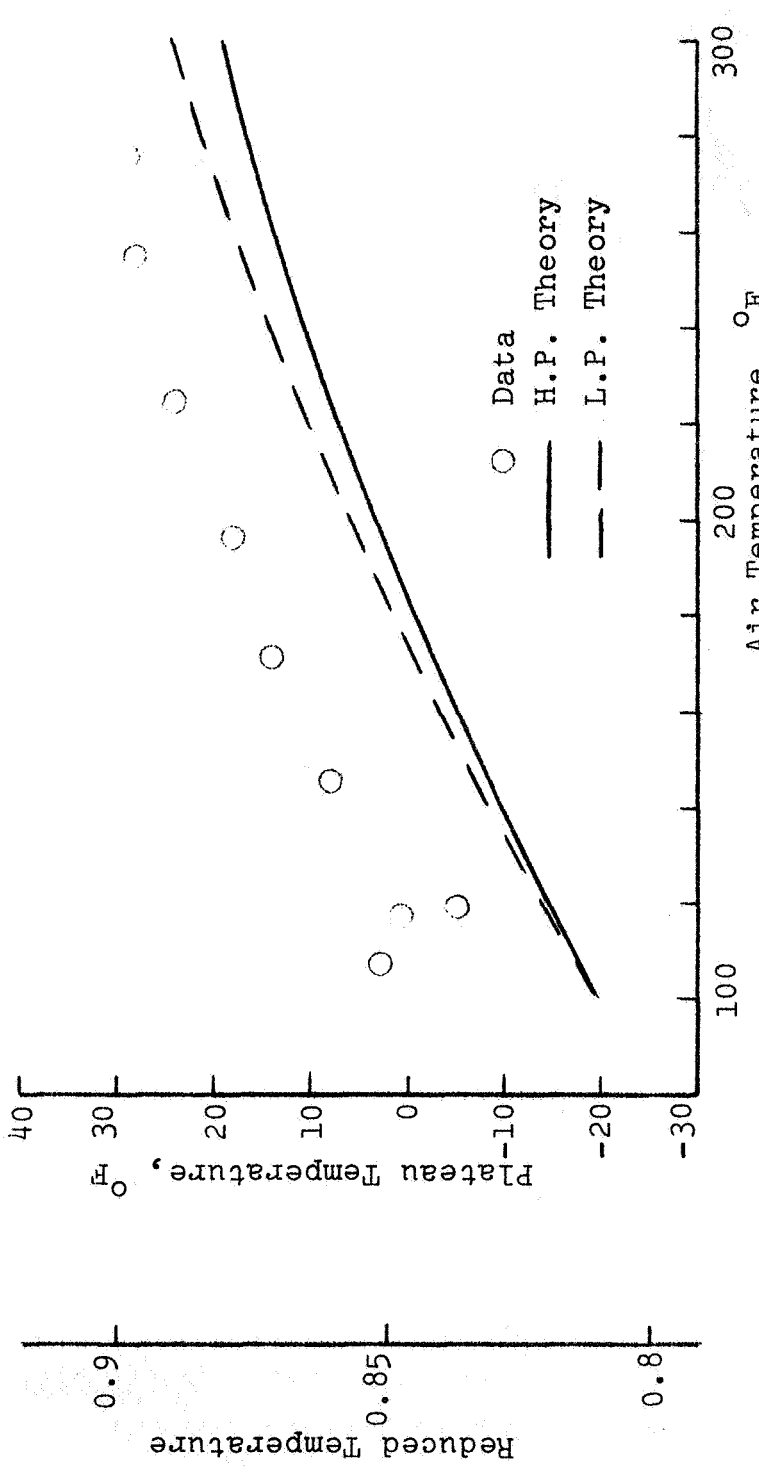

Fig. 33. Plateau vs Air Temperature for Fr-13 Drops Vaporizing in Air at 1.25 P_c

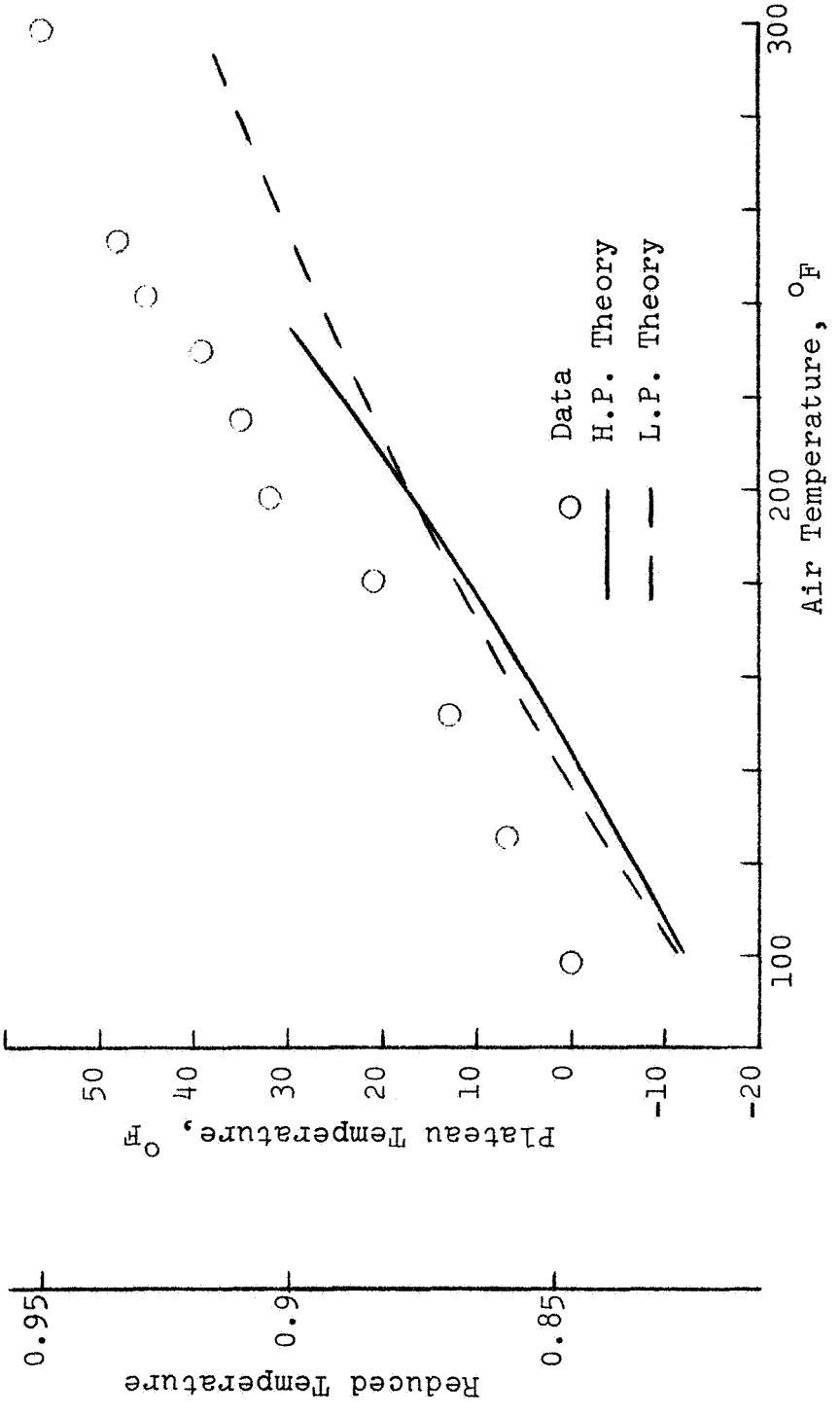

Fig. 34. Plateau vs Air Temperature for Fr-13 Drops Vaporizing in Air at $1.5P_c$

above 240° F no plateau temperatures satisfy the high pressure film theory. The highest recorded plateau temperature at any pressure is plotted on the figure. It corresponds to a reduced temperature of 0.95 with respect to the Fr-13.

Five data points at a reduced pressure of 1.75 (66.9 atm abs) were obtained. They are compared with calculated plateau temperatures on Fig. 35. There is very little difference between the two theoretical predictions except that the high pressure theory predicts no solution above an air temperature of 160° F. This result is a consequence of the property relations; it does not correspond to the mixture critical point, and it is believed to be physically unrealistic. The calculated values are about 20° F lower than the measured plateau temperatures.

The plateau versus air temperature data were fitted by a third order least squares routine and the results for all pressures are shown on Fig. 36. The results appear somewhat unsystematic. The curve for a reduced pressure of 1.75 is based upon few data, and it may not be representative. However, the non-linear behavior of the plateau temperature with pressure at low air temperatures is believed to be a reflection of the liquid-vapor equilibria characteristics.

The following figure, Fig. 37, shows this non-linear behavior. It is interesting to note that the high pressure film theory result has a similar shape to the data which

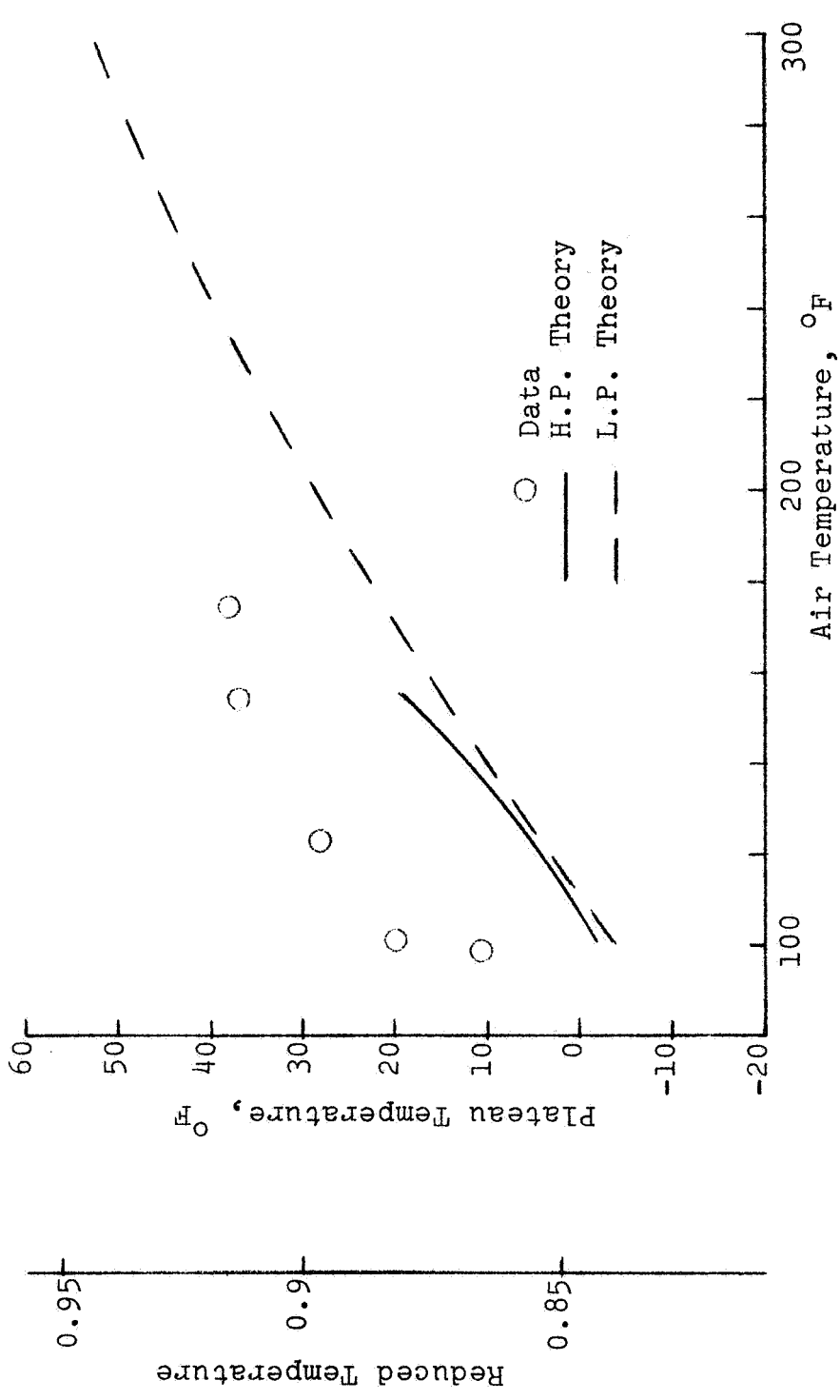

Fig. 35. Plateau vs Air Temperature for Fr-13 Drops Vaporizing in Air at 1.75 P_c

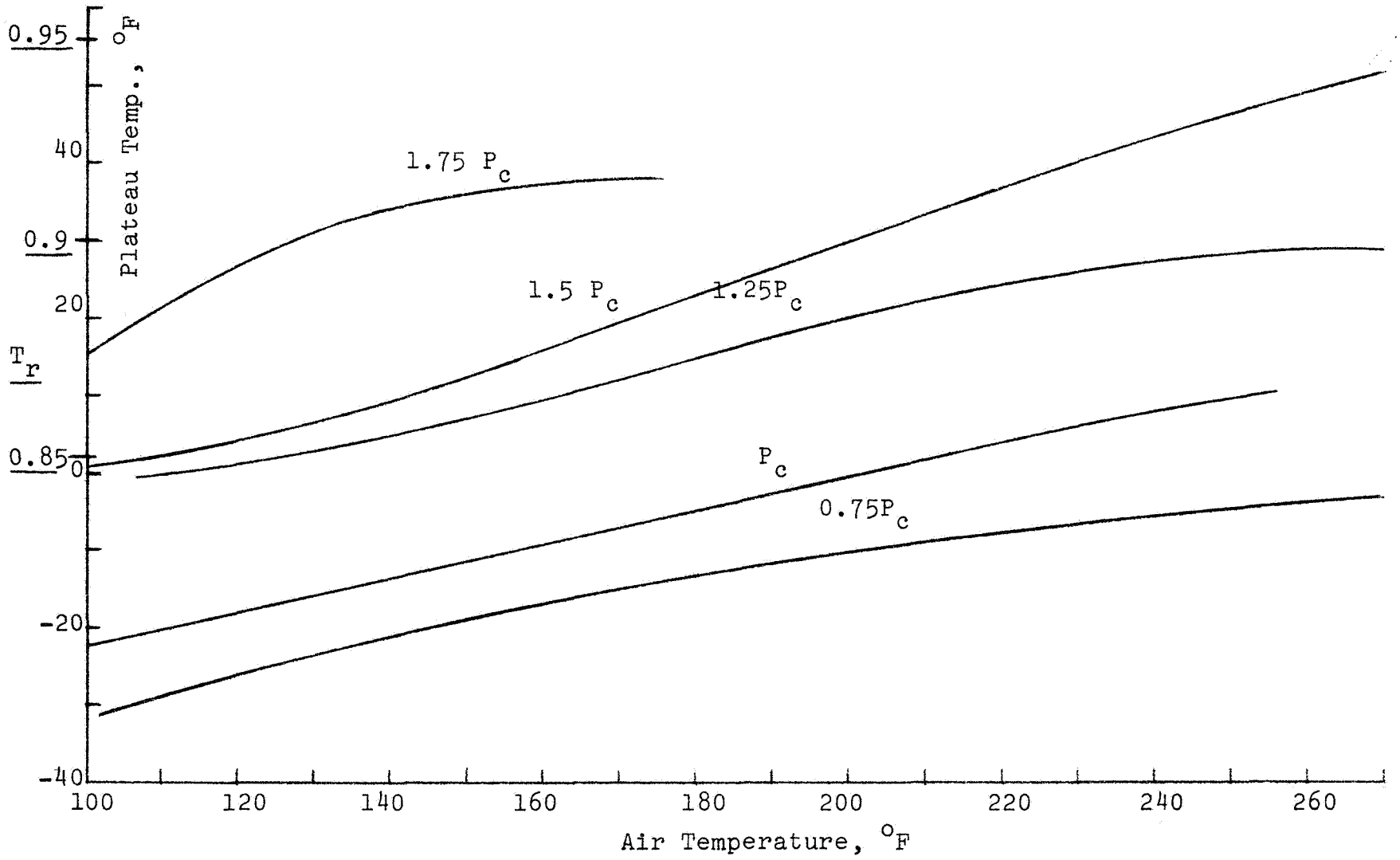

Fig. 36. Summary of Fr-13 Temperature Data

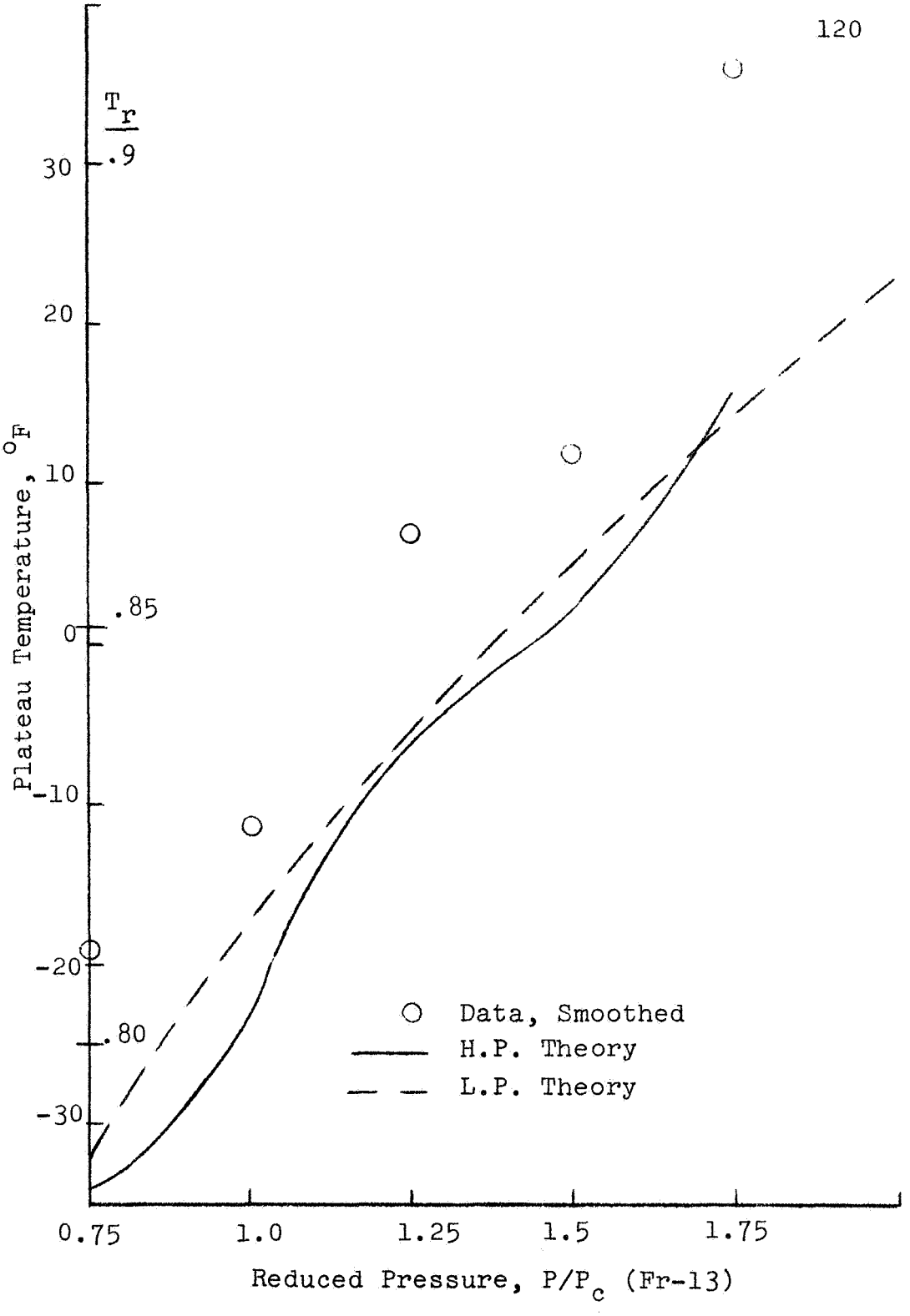

Fig. 37. Summary of Fr-13 Temperature Data, Shown vs Pressure for Air Temperature of 150°F

were cross-plotted from Fig. 36. The calculated results generally predict plateau temperatures 10° F low and become more in error at the highest pressure.

Fig. 38 shows a comparison between the variation of plateau temperature with pressure, air temperature fixed at 250° F, for calculated and measured results. The high pressure theory agrees better with the data at high pressures, and the low pressure theory gives better agreement at low pressures. The calculated results are typically 10-15° F low over the range of pressures investigated.

The Fr-13 data were analyzed for mass transfer rates and comparisons were made with calculations. The data reduction technique was described in Chapter IV. As in the case of the n-heptane drop data, experimentally determined Nusselt numbers were compared with ones calculated with the Ranz-Marshall correlation at the measured conditions. The results for 5 droplet histories at various pressures are shown on Fig. 39. The ratio of Nu_{calc}/Nu_{exp} are typically 0.7, and there is no systematic dependence on pressure. The range of drop Reynolds number for the points is 275-425, and there is no apparent dependence on it either.

There are four explanations for the consistently low values of Nu_{calc}/Nu_{exp}. The first is that drop motion including internal circulation, oscillation and rotation enhances the heat transfer rate with respect to the rigid sphere results of the Ranz-Marshall data. The second is that the

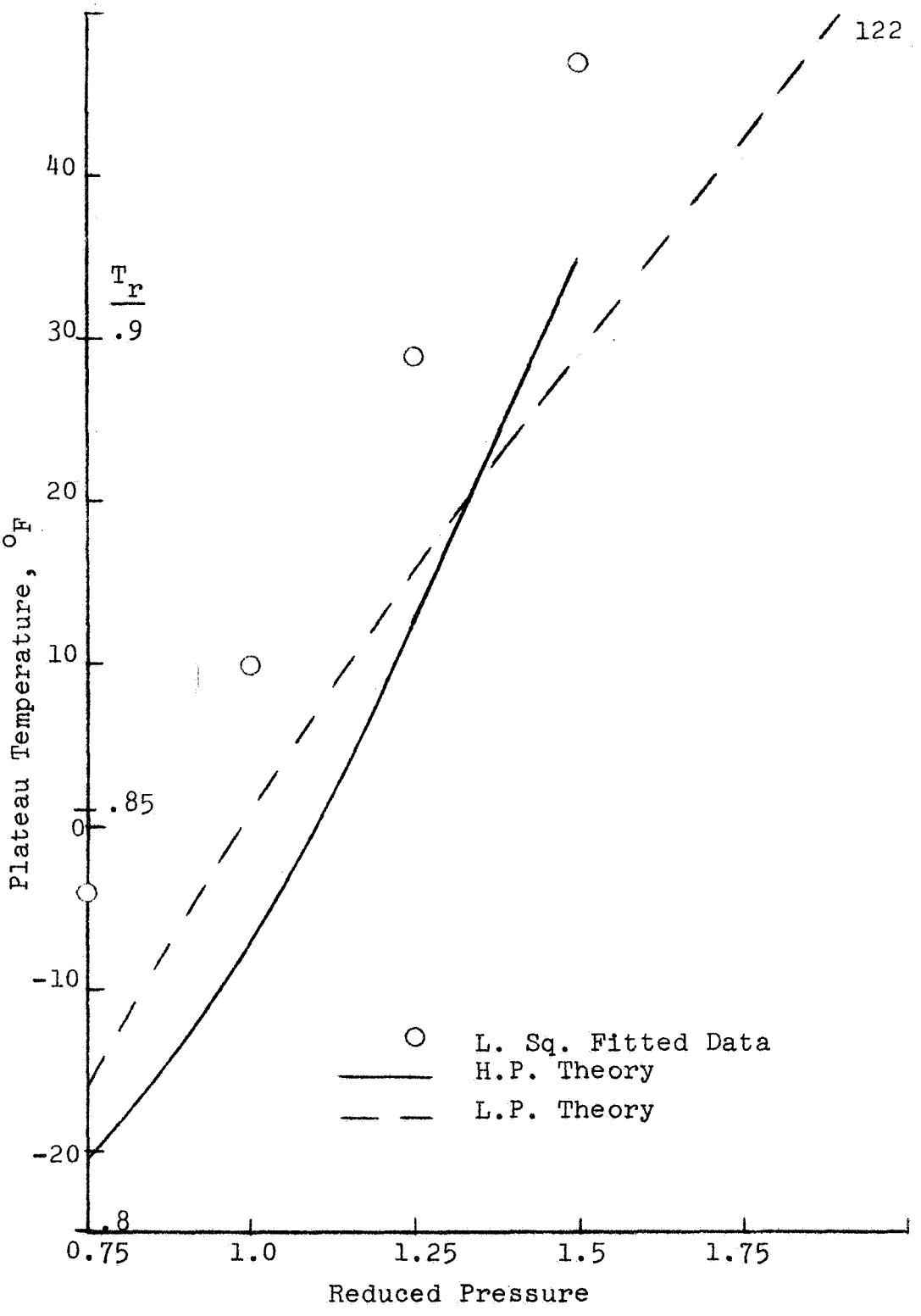

Fig. 38. Summary of Fr-13 Temperature Data, Shown vs Pressure for Air Temperature of 250°F

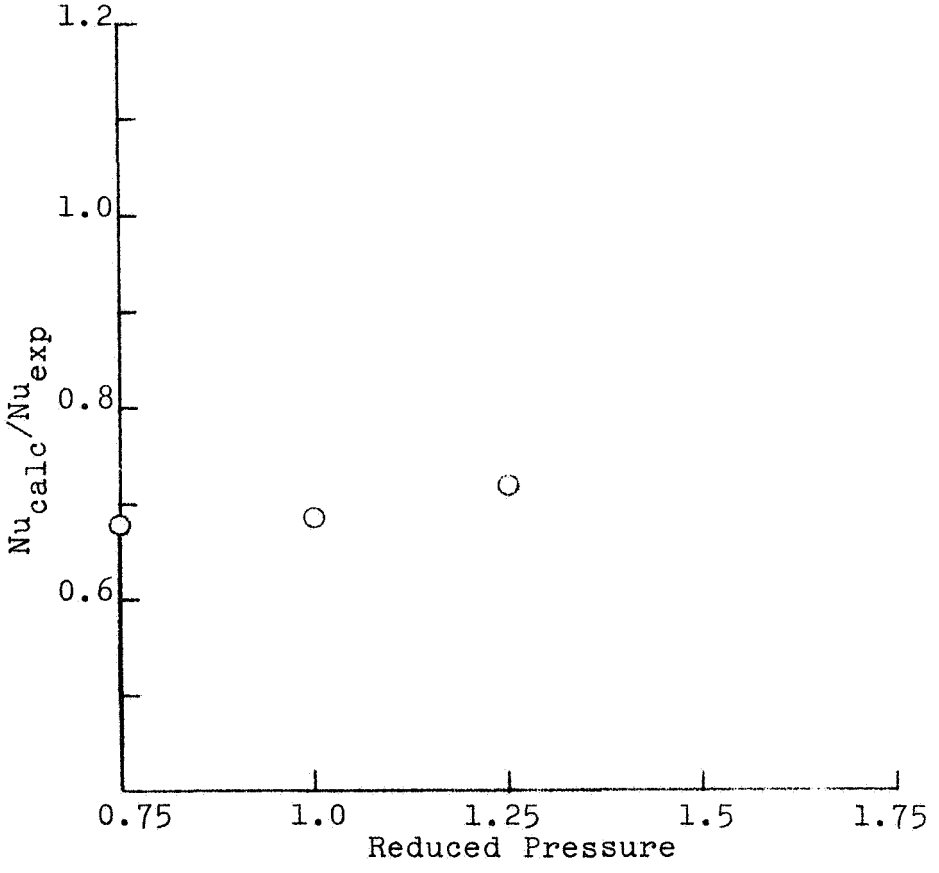

Fig. 39. Variation of Calculated to Measured Nusselt Number Ratio With Pressure for Fr-13 Drop Data

Ranz-Marshall correlation corrected for high mass transfer rates is inappropriate for vaporizing drops in the near critical region irrespective of drop shape and motion effects. The third explanation is that the results are primarily due to the non-spherical shape of the Fr-13 drops. As discussed in Chapter IV, in the region of opposed flow of combined convection, heat transfer rates are higher than those predicted by forced flow for the case of simultaneous heat and mass transfer; this is the fourth explanation.

The calculated Nusselt numbers contain a correction for high mass transfer rates upon heat transfer as discussed in Chapter II. The correction factors varied from 0.65-0.8 for the results shown on Fig. 39. The application of these calculated correction factors which are based upon film averaged properties is a source of error. Application of Hsu, Sato and Sage's results (24) for the influence of drop shape on mass transfer indicates that the heat transfer rates predicted by the Ranz-Marshall correlation could be 10-30% low. However, the Hsu, Sato and Sage correlations are for pendant shaped drops, not irregular ones like the Fr-13 data, and they are for mass transfer, although the heat-mass transfer analogy would support their application to heat transfer rates also. Fig. 40 shows the Nu_{exp} values for the data points normalized by $(Re^{1/2}Pr^{1/3})$ plotted versus Gr/Re^2, the combined convection parameter. The

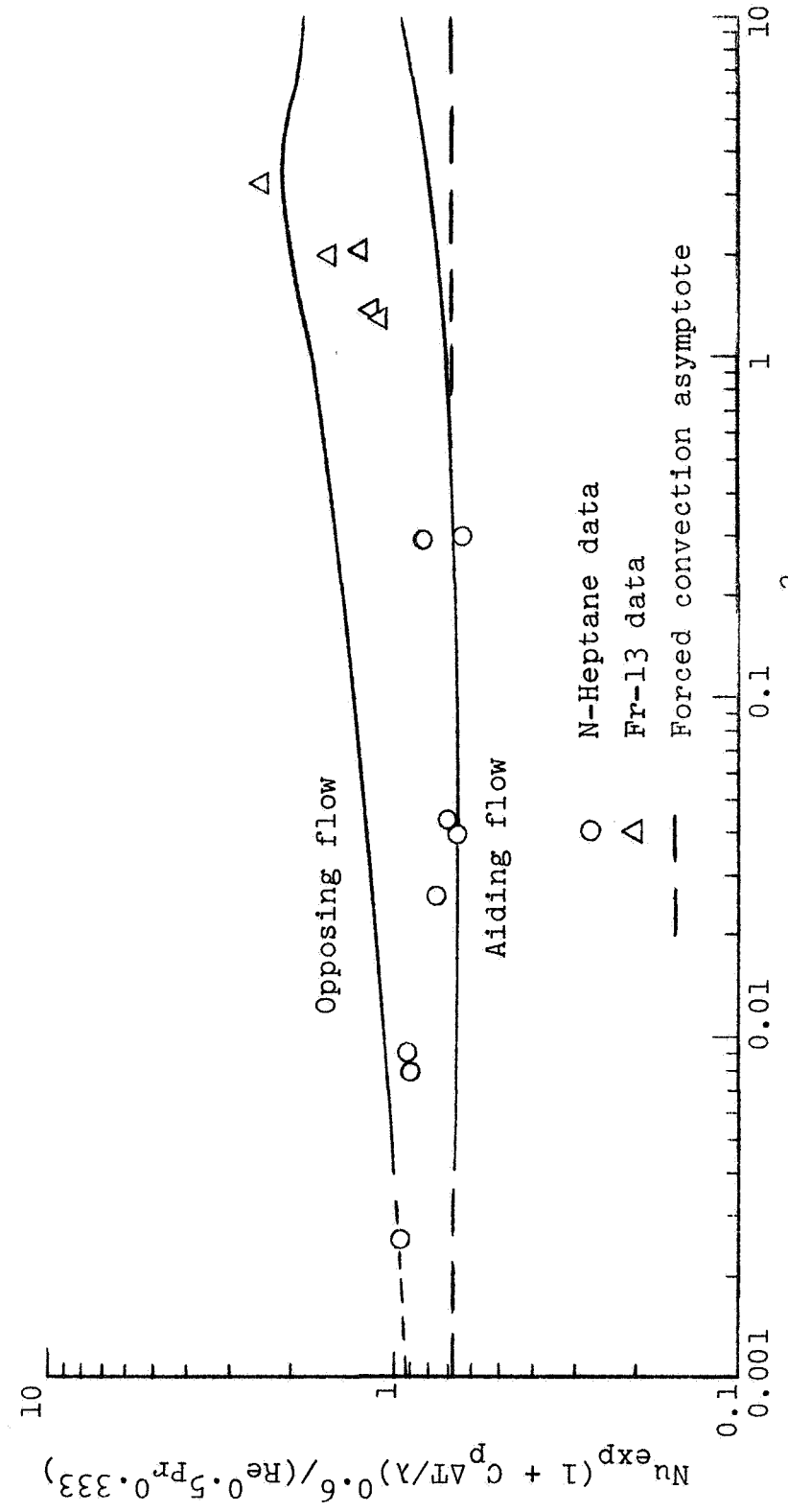

Fig. 40. Normalized Nusselt Numbers vs Gr/Re^2 for High Pressure Drop Data

results of Narasimhan and Gauvin (38) for aiding and opposing flow are shown also on the figure for comparison as well as the pure forced convection asymptote of $Nu_{exp}/(Re^{1/2}Pr^{1/3})=0.68$. The Fr-13 drop data fall generally between the forced flow limit and that for opposed flow supporting the hypothesis that the combined convection phenomenon is an important effect. The Fr-13 data may well be the result of a starting transient since the droplet lifetimes are less than 0.5 sec. Since the results shown on Fig. 40 are fairly consistent and there are several probable explanations for the low calculated values, the data were accepted and mass transfer comparisons were made.

Figs. 41, 42, 43, 44 and 45 show comparisons between quasi-steady film theory calculations and drop histories at reduced pressures of 0.75, 1.0, 1.25, 1.5 and 1.75, respectively. Drop temperature and mass transferred histories are compared for each drop. In every case but $P_r = 1$, both the low pressure and high pressure film theory calculated result is shown. On Fig. 42 the results for $P_r = 1$, calculated results for high pressure film theory with no absorption of air in the liquid phase, are included. In every case the calculated temperatures are lower than the measured ones although the calculated values are usually within 10° F of the measured. The temperature history calculated under the assumptions of high pressure film theory with no air absorption in the liquid phase is almost twice as low

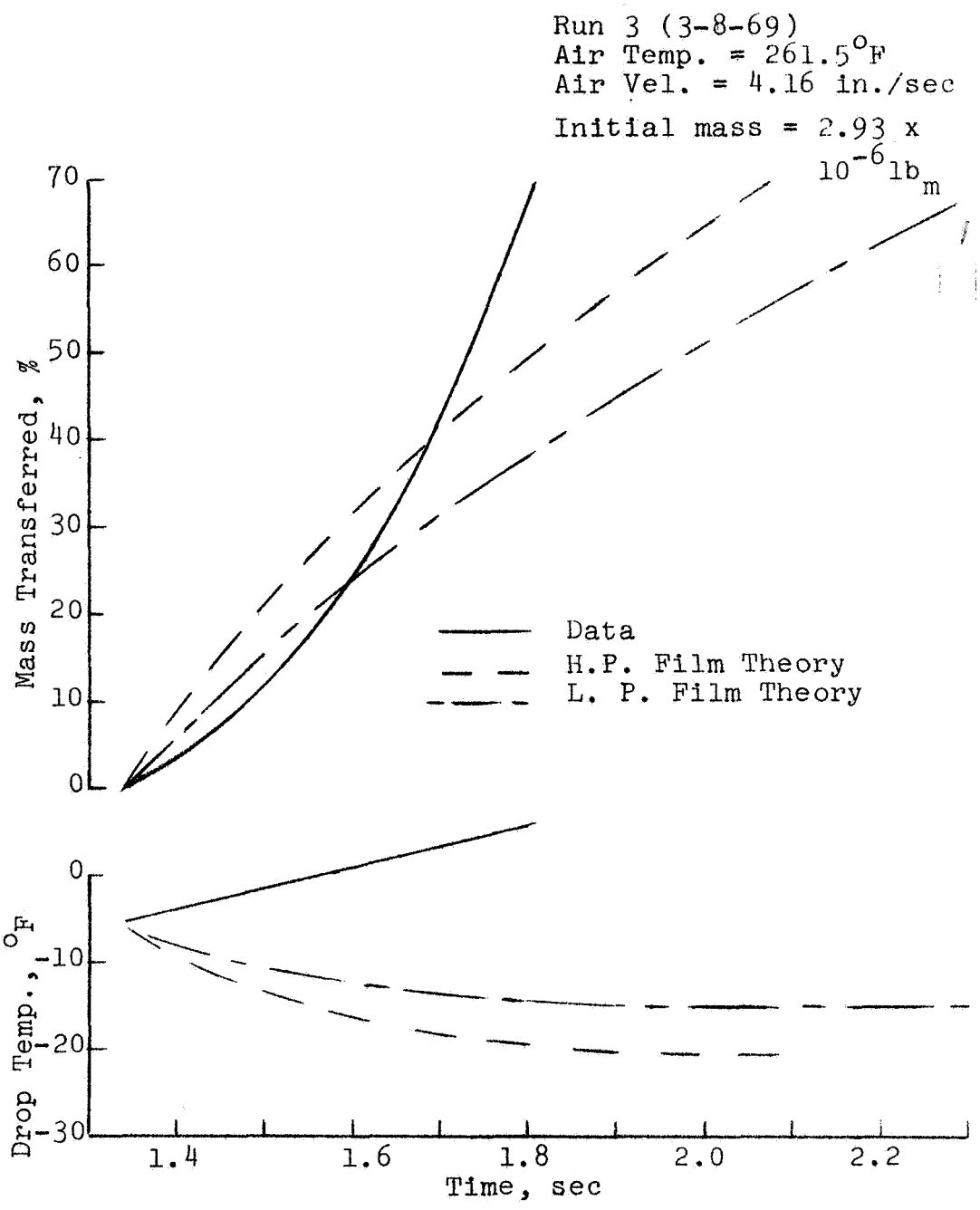

Fig. 41. History of Fr-13 Drop Vaporizing in Air at 0.75 P_c

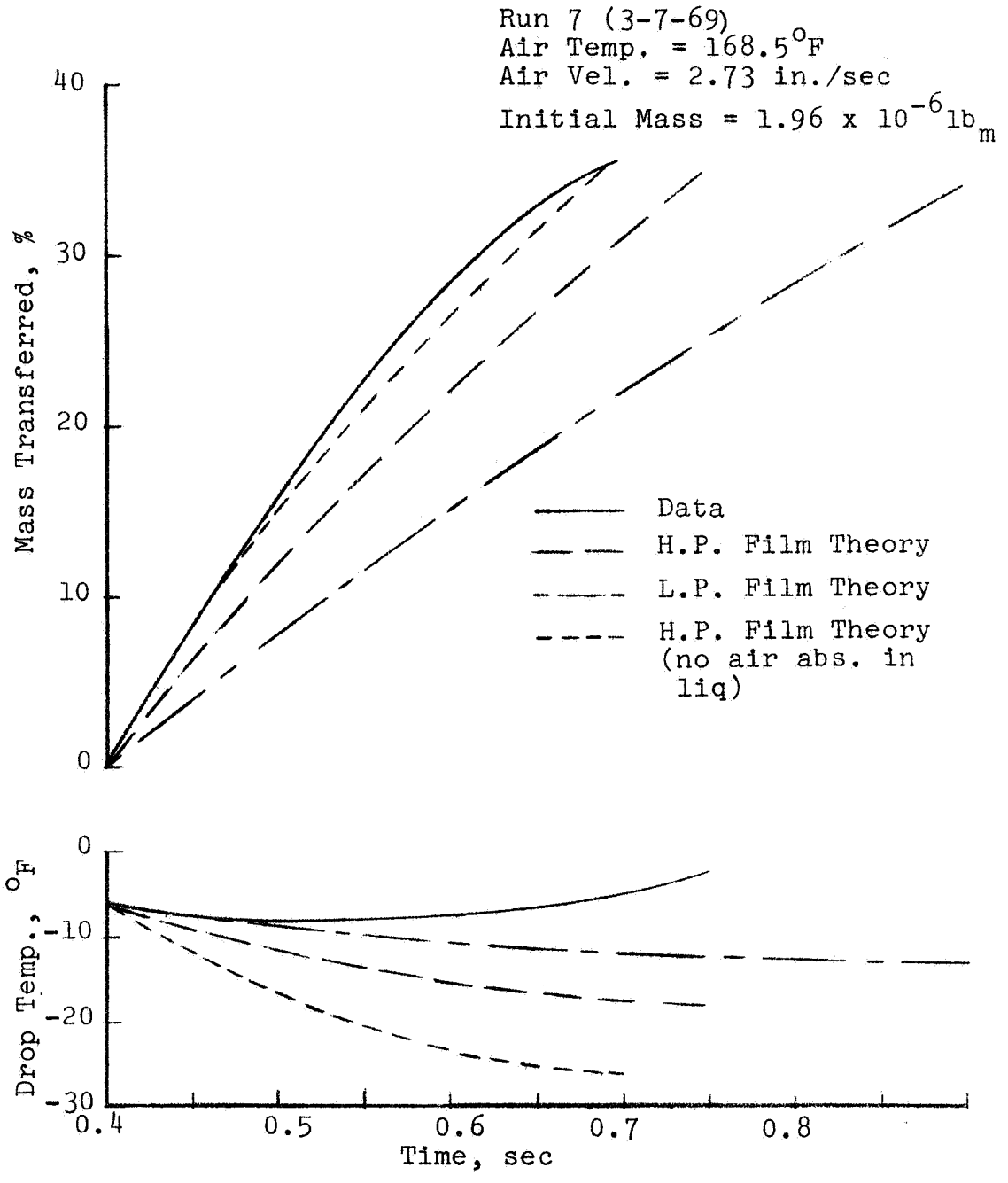

Fig. 42. History of Fr-13 Drop Vaporizing in Air at P_c

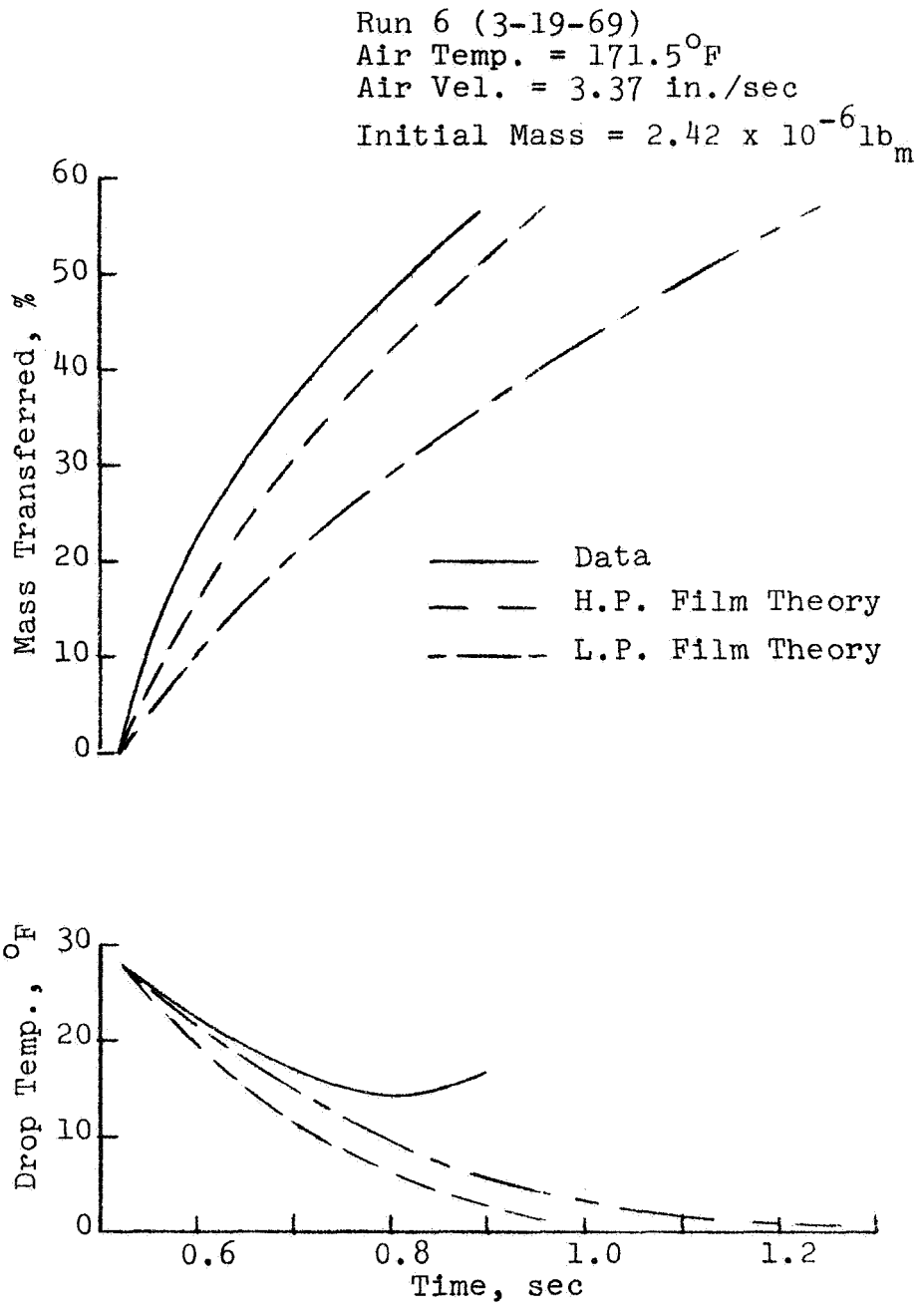

Fig. 43. History of Fr-13 Drop Vaporizing in Air at 1.25 P_c

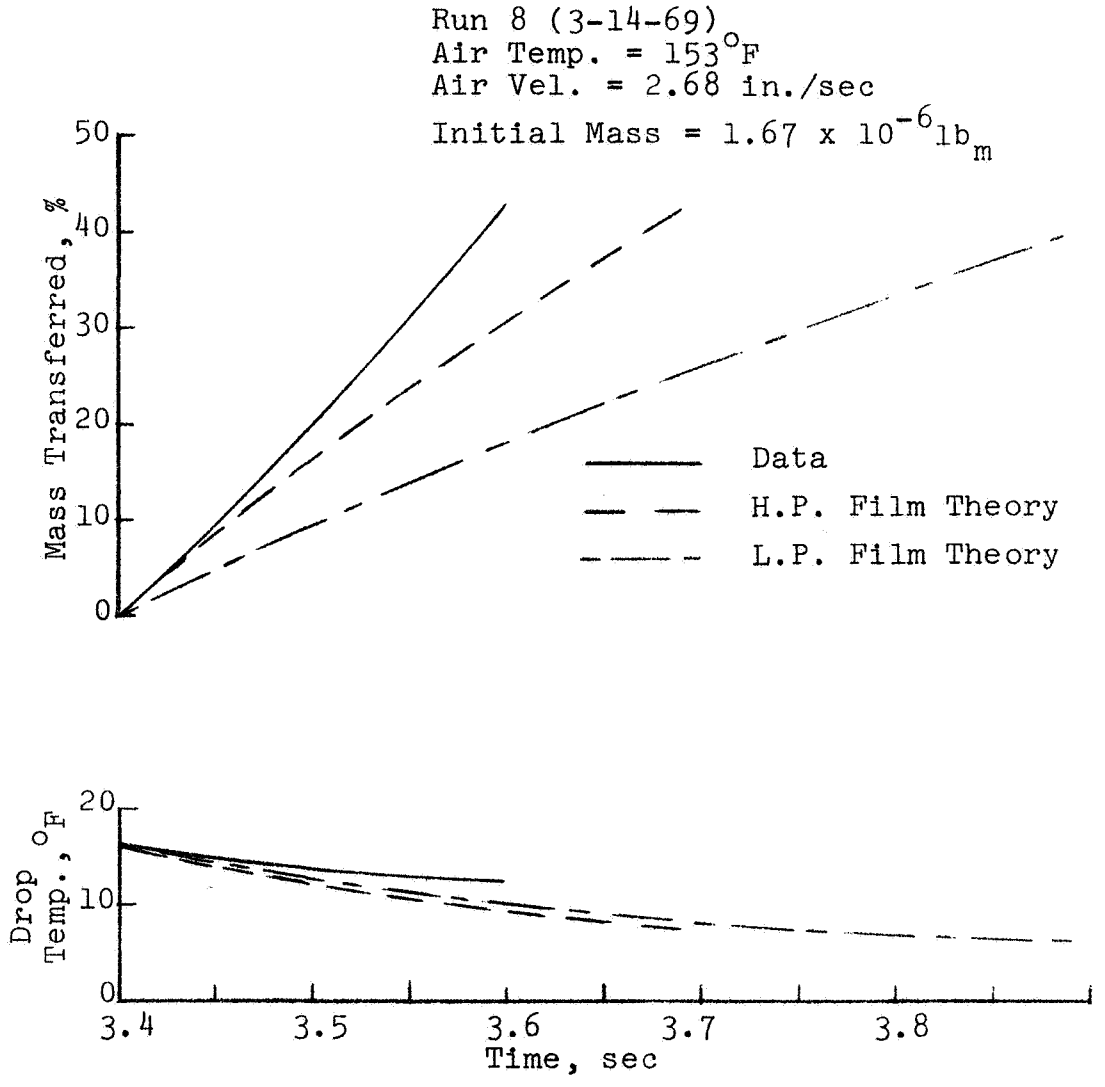

Fig. 44. History of Fr-13 Drop Vaporizing in Air at 1.5 P_c

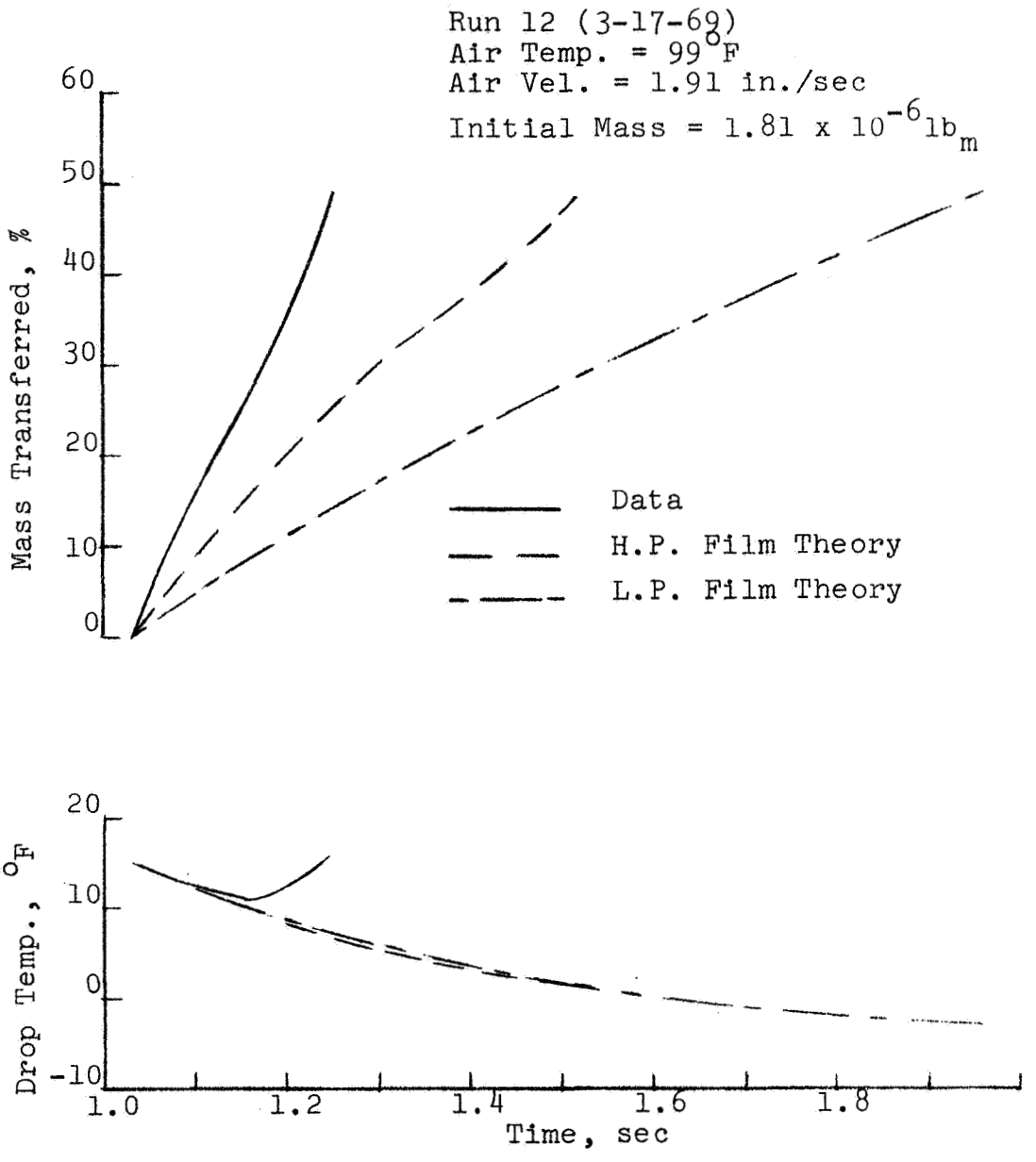

Fig. 45. History of Fr-13 Drop Vaporizing in Air at 1.75 P_c

compared to the measured value as the other calculated values are for the same $P_r = 1$ case.

The calculated mass transfer rates are lower than the measured rates with the low pressure film theory result usually twice as much in error as the high pressure result. At reduced pressures from 0.75-1.5 the high pressure film theory results are 0-30% low with the error increasing with increasing pressure. The mass transfer rate predicted by high pressure theory with no air absorption for the $P_r = 1$ case, shown on Fig. 42, corresponds closely to the measured rate although the high pressure theory result assuming equilibrium at the interface is only 10% below the measured rate.

The slopes of the calculated mass transferred curves on Figs. 41-45 were compared with the slopes of the corresponding measured rates for both high and low pressure film theory. These results are shown on Fig. 46. There is a distinct trend of underestimation with increasing pressure for both theories. Errors of 50% and 75% are noted for the highest pressure, $P_r = 1.75$, for high and low pressure film theories, respectively.

The calculation of the critical mixing line or gas mixture transition to a critical state was discussed in Chapter II. The solid line on Fig. 47 is a portion of the locus of critical states calculated for Fr-13-air mixtures. As previously discussed, the attainment of a critical state

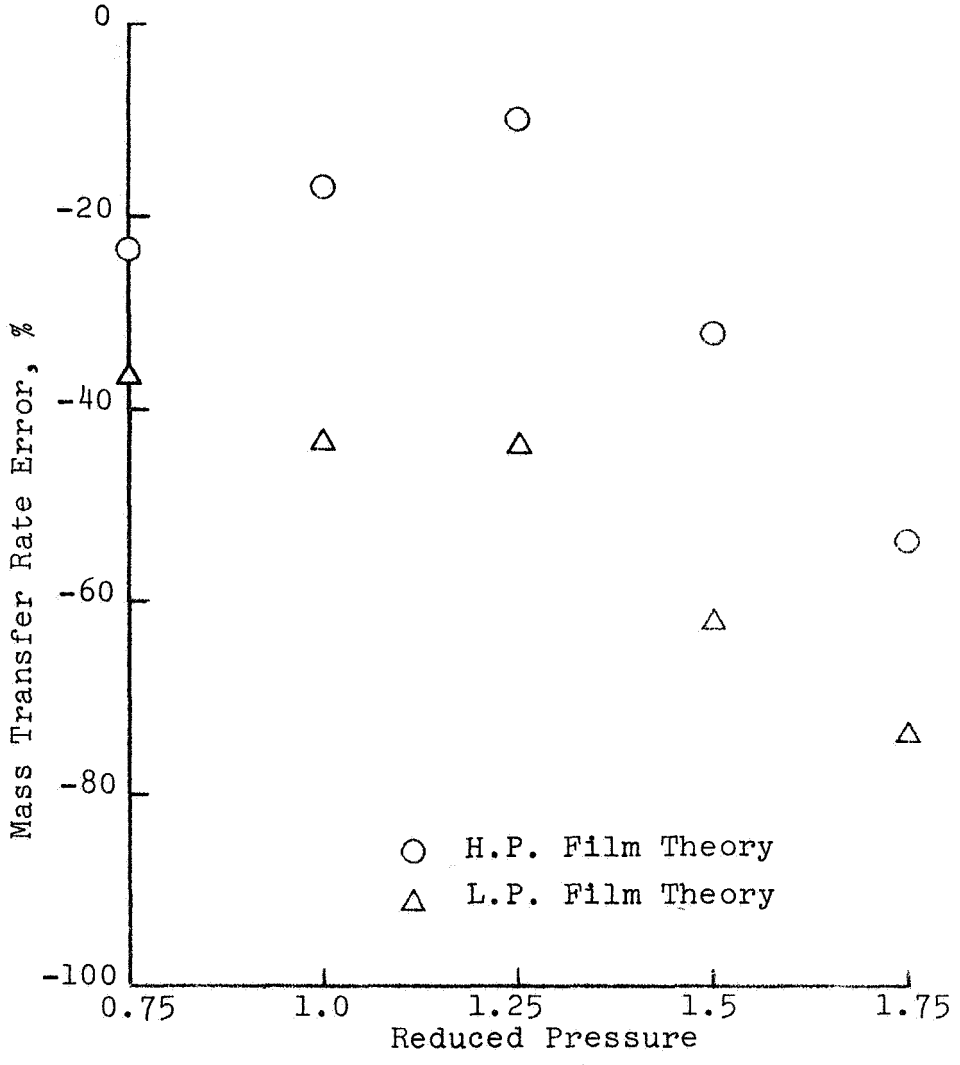

Fig. 46. Effect of Pressure on Calculated Mass Transfer Error for Fr-13 Drops Vaporizing in Air

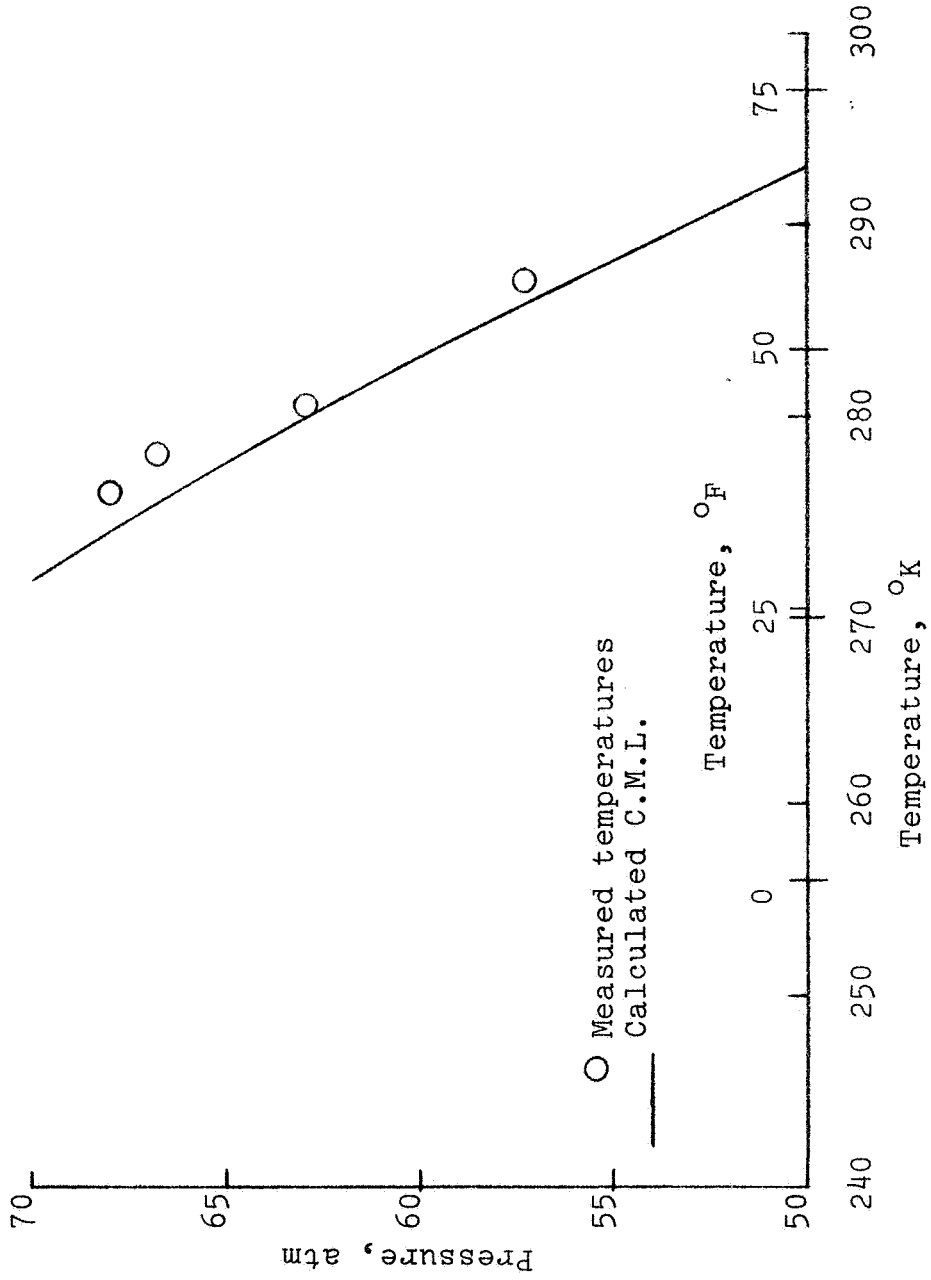

Fig. 47. Comparison of Highest Experimental Plateau Temperatures with Calculated Critical Mixing Line for Fr-13-Air Gas Mixtures

in the gas phase at the drop interface was expected to be the initiating condition for non-classical temperature history behavior. If this hypothesis is correct, the departure from plateau-like behavior should correlate with the critical mixing line. This correlation is confirmed by the maximum measured drop temperatures exhibiting a distinct plateau which are plotted for four pressures on Fig. 47. The temperature point corresponding to the three highest pressures each resulted from a series of drop temperature histories at successively lower air temperatures at a fixed pressure. The transition from non-classical to classical temperature histories is shown on Fig. 48 for reduced pressures of 1.65, 1.75 and 1.78.

The point on Fig. 47 corresponding to a pressure of 57.5 atm abs (P_r = 1.5) was the highest plateau temperature obtained at the pressure. No steadily increasing drop temperature histories were recorded since the higher air temperatures required would have exceeded the rig maximum design limit of 300° F air temperature.

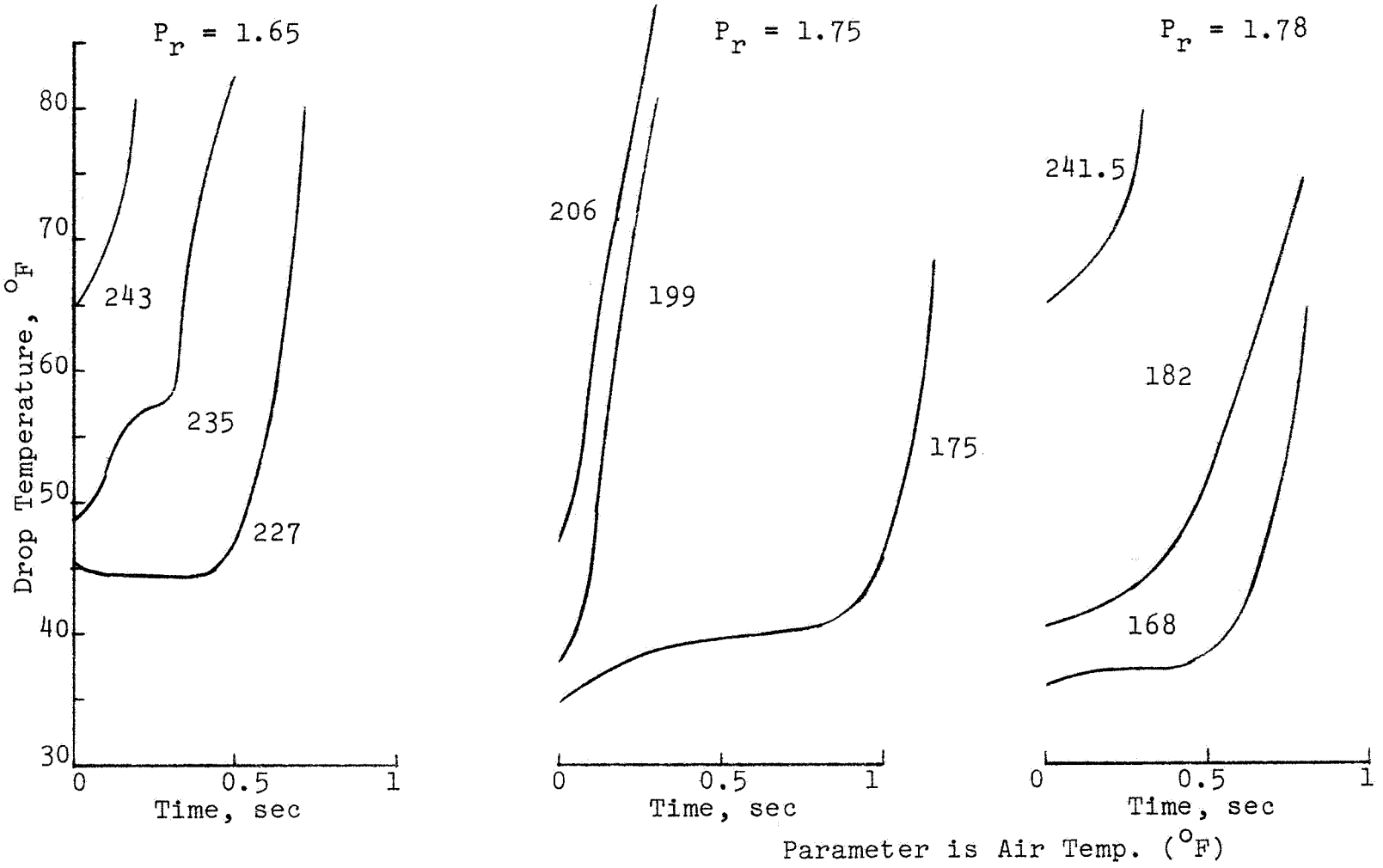

Fig. 48. Transition from Classical to Unclassical Behavior of Fr-13 Drop Temperature Histories

VI. CONCLUSIONS

The suspended droplet vaporization data obtained in this investigation are shown in relation to high pressure vaporization results of other investigations in Fig. 49. The present results are the first vaporization data known to the author that were obtained at reduced pressures above 0.75 where drop size and temperature histories were obtained under measured flow conditions. In addition, the n-heptane-air vaporization data are the first known data at reduced pressures above 2 under any flow conditions.

The conclusions which follow are based upon the n-heptane-air and the Fr-13-air data reported in Chapter V. The conditions of the n-heptane data are: air temperature 100-300° F, air pressure 1.5-100 atm abs, drop Reynolds number 150-600, and the initial drop diameter 1275-2025 microns. The Fr-13 drop data conditions are: air temperature 100-300° F, air pressure 29-68 atm abs, drop Reynolds number 250-450, and initial drop diameter 980-1200 microns. The seven main conclusions are given in the following list.

1. The ability to suspend vaporizing droplets in 1 g field on a temperature probe at measured liquid temperatures up to a reduced value of 0.95 (within 28° R of the liquid critical temperature) and at an air pressure of 56 atm was demonstrated.

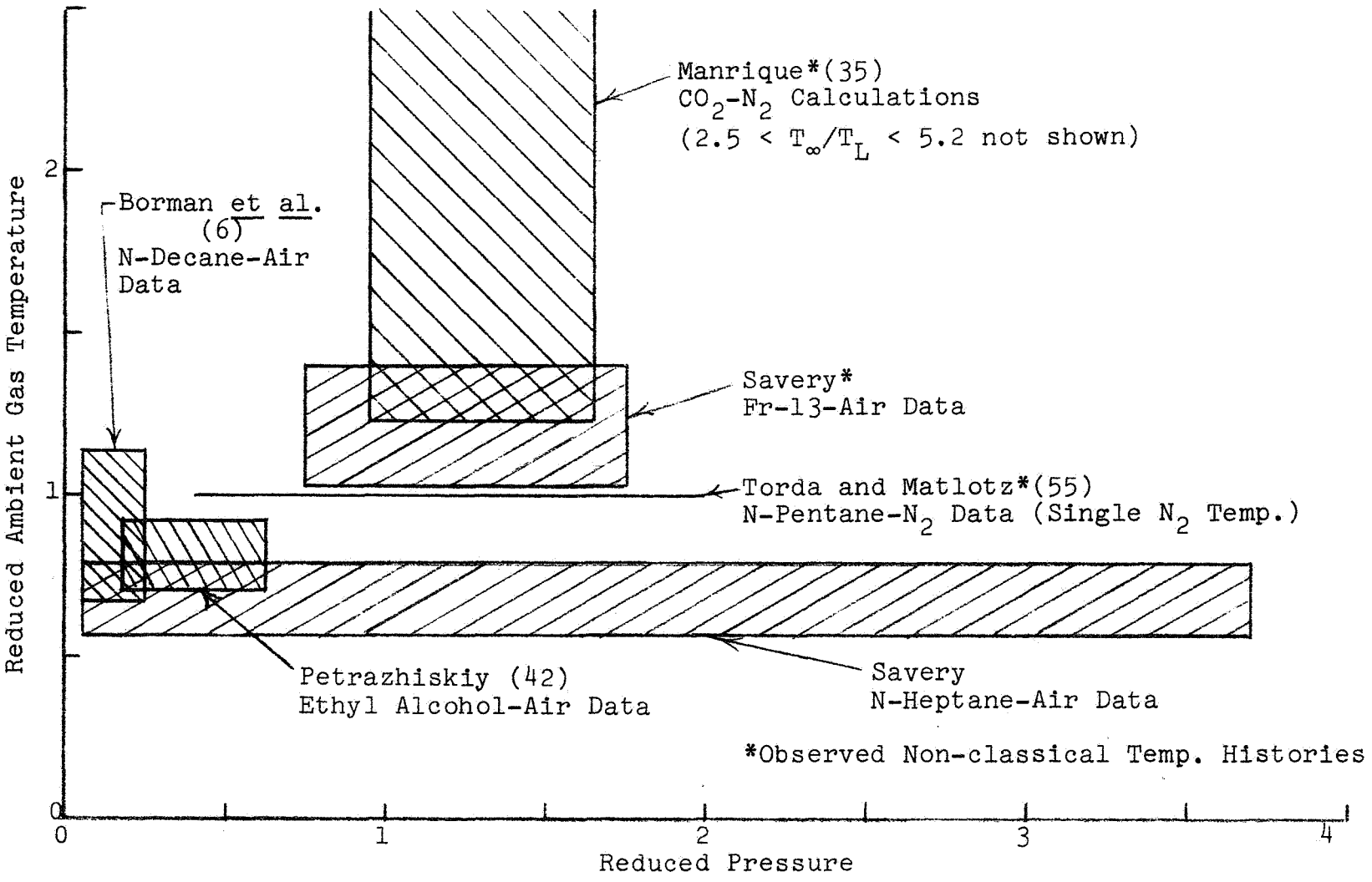

Fig. 49. Summary of High Pressure Drop Vaporization Results

2. Under conditions of low ambient gas temperature ($T_\infty/T_c < 0.8$) and high pressure ($0 < P/P_c < 3.7$) predictions by film theory corrected and uncorrected for high pressure properties both compared favorably (within 5° F) with measured plateau temperatures.
3. Under conditions of low ambient gas temperature ($T_\infty/T_c < 0.8$) and high pressure ($0 < P/P_c < 3.7$) predictions by film theory corrected for high pressure properties agreed to within $\pm$ 25% of measured mass transfer rates. Film theory uncorrected for high pressure yielded mass transfer results of similar accuracy up to about 5 atm abs air pressure ($P/P_c = 0.18$); at the highest pressure the predicted mass transfer rate was 80% low.
4. Under conditions of moderate ambient gas temperature ($1 < T_\infty/T_c < 1.5$) and high pressure ($0.75 < P/P_c < 1.75$) predictions by film theory corrected and uncorrected for high pressure properties were consistently $10\text{-}15^\circ$ F below the measured plateau temperatures. The low pressure theory gave slightly better plateau temperature predictions at reduced pressures below 1.25, and the results for both theories were the same at higher pressures.
5. Under conditions of moderate ambient gas temperature ($1 < T_\infty/T_c < 1.5$) and high pressure ($0.75 < P/P_c < 1.75$) predictions by film theory corrected

for high pressure properties agreed to within 35% of measured mass transfer rates at reduced pressures less than 1.5. The predicted mass transfer rates were low by about 50% at a reduced pressure of 1.75, and the predicted values exhibited a systematic trend to increasingly underestimate mass transfer rates as the pressure increased. The low pressure film theory mass transfer predictions showed similar trends although the errors were generally twice as great.

6. Under conditions of moderate ambient gas temperature ($1 < T_\infty/T_c < 1.5$) and high pressure ($0.75 < P/P_c < 1.75$) drop heat transfer Nusselt numbers calculated from the Ranz Marshall correlation were about 30% below Nusselt numbers derived from the measured vaporization rates and temperature differences.
7. A departure from classical drop temperature history behavior was observed at reduced pressures greater than 1.5, and this transition from behavior exhibiting a plateau to that with steadily increasing temperature was correlated with the drop interface gas mixture critical state.

In the range of data considered significant, nonidealities of thermodynamic and transport properties were encountered. There is scant data available and it was

usually necessary to resort to calculations using generalized equations of state and corresponding state type correlations of properties. These property non-idealities introduced uncertainties into the calculated results and indirectly into some of the measured results, e.g., experimental Nusselt numbers for heat transfer.

In Chapter IV the uncertainties in the measured quantities were estimated as well as their effects upon the calculated results. For the Fr-13-air case considered it was estimated that the calculated results should lie within 13° R for drop plateau temperature and 23% of mass transfer rate of the measured values if the theory itself and property values used within the theory are accurate. All of the high pressure film theory calculations agreed with the data within these tolerances over the entire range of data except with respect to mass transfer rates at reduced pressures greater than 1.25 and at moderate ambient gas temperatures. Thus, on this basis the application of film theory corrected for high pressure is vindicated for the entire range of data of the present investigation shown on Fig. 49 except for that associated with the Fr-13-air data above a reduced pressure of 1.25.

Corrections to the Nusselt and Sherwood numbers computed by the Ranz-Marshall correlations for high mass transfer rates of 0.65-0.8 were applied to the Fr-13 drop calculated histories. These relatively large corrections

raise doubts about the application of the Ranz-Marshall results to these data. The corrections to the n-heptane calculated results were much closer to unity due to the relatively low air temperatures covered.

There are several recommendations for future work in the area of high pressure droplet vaporization. They are primarily focused on the approach of suspended droplet experiments. The recommendations are as follows:

1. Additional data with other vaporizing media in the high pressure, moderate temperature range is desirable. This would allow confirmation of the data and film theory calculations developed for Fr-13-air. A paraffin fuel vaporizing in nitrogen would be a good choice. Another candidate liquid would be CO_2 vaporizing in a nitrogen environment since comparisons with Manrique's detailed calculations (35) would be possible. A paraffin fuel or CO_2 vaporizing in high pressure air, although more readily obtainable with the present experimental setup, would be less desirable but acceptable combinations.
2. It is desirable to have drop shape measurements of unsupported drops moving relative to a gas environment at supercritical pressures and temperatures in order to relate the results of suspended drop experiments to conditions in a combustion

chamber.

3. The corrections to heat and mass transfer coefficients due to high mass transfer rates require some attention, perhaps theoretical, since they become important at near critical conditions.
4. High pressure vapor-liquid equilibria data up to the mixture critical point is necessary to refine any theories and carefully test high pressure vaporization models with vaporization data.
5. In the range of low ambient gas temperature ($T_\infty/T_c < 0.8$) and high pressure ($0 < P/P_c < 3.7$) vaporization data over a greater range of droplet Reynolds number at each pressure are desirable to check on the Reynolds number dependence of mass transfer rate. This would give a greater variation in drop shape (independent of pressure) which may have a significant effect on the heat and mass transfer coefficients.

APPENDIX A. PROPERTY DATA

The property relations for air, water, n-heptane and Fr-13 (chlorotrifluoromethane) are summarized in this appendix. These equations were utilized in the steady-state and quasi-steady vaporization calculations. In most cases data from the source, indicated by the reference number following the property name, were fitted by a cubic least squares fit. In some cases property equation was taken directly from the data source. The signed number following "E" in a coefficient indicates the power of ten by which the preceding number should be multiplied.

Air Properties

1. Specific heat (22)

$$C_p = (6.2240836 - 9.892961E\text{-}03T + 1.2698753E\text{-}05T^2 - 5.476402E\text{-}09T^3)\ 0.068559$$

where $504 < T < 756^{\circ}$ R and C_p(BTU/lb_m-$^{\circ}$R)

2. Thermal conductivity (22)

$$k = (6.95252E\text{-}03 + 2.1973672E\text{-}03T - 3.3275553E\text{-}07T^2 - 6.0211273E\text{-}11T^3)\ 0.3225E\text{-}06$$

where $504 < T < 756^{\circ}$ R and k(BTU/in.-sec-$^{\circ}$R).

3. Dynamic viscosity (22)

$$\mu = (-4.2220761E\text{-}03 + 2.5743035E\text{-}03T - 1.2586084E\text{-}06T^2 + 3.621639E\text{-}10T^3)\ 0.960E\text{-}06$$

where $504 < T < 756^{\circ}$ R and $\mu(lb_m/in.\text{-}sec)$

4. Critical constants (47)

$$T_c = 132.4^{\circ} K$$

$$P_c = 37.25 \text{ atm}$$

Water Properties

1. Vapor Pressure (29)

$$P_{sat} = 218.167 \times 10^{-n}$$

For $T_L > 373.16$

$$n = \left[3.346313\ (647.27 - T_L) + 4.1413E\text{-}02(647.27 - T_L)^2 + 7.515484E\text{-}09(647.27 - T_L)^4 + 6.56444E\text{-}11(647.27 - T_L)^5\right] / \left[1.3794481E\text{-}02T_L (647.27 - T_L) + T_L\right]$$

For $T_L \leq 373.16$

$$n = \left[3.2437814(647.27 - T_L) + 5.86826E\text{-}03(647.27 - T_L)^2 + 1.1702379E\text{-}08(647.27 - T_L)^4\right] / \left[2.1878462E\text{-}03 \times T_L(647.27 - T_L) + T_L\right]$$

where $T_L(^{\circ}K)$ and $P_{sat}(atm)$

2. Enthalpy of vaporization (29)

For $T_L \leq 690^\circ$ R

$$\lambda = 1.5409974E+03 - 1.5304025 \times T_L + 1.701721E-03 \times T_L^2 - 1.0238529E-06T_L^3$$

For $T_L > 690^\circ$ R

$$\lambda = 408.35902 + 3.1484431T_L - 4.7181765E-03T_L^2 + 1.9004536E-06T_L^3$$

where $T_L(^\circ R)$ and $\lambda(BTU/lb_m)$

3. Vapor specific heat (37)

$$C_p = 0.5799577 - 2.9462E-06T - 1.4249794E-06T^2 + 1.81177E-09T^3$$

where $T(^\circ R)$ and $C_p(BTU/lb_m-^\circ R)$

4. Vapor thermal conductivity (22)

$$k = (-0.15603002 + 2.0814256E-03T + 5.862479E-07T^2 - 8.469343E-11T^3)\ 0.212E-06$$

where $T(^\circ R)$ and $k(BTU/in.-sec-^\circ R)$

5. Vapor dynamic viscosity (22)

$$\mu = (-3.7342072E-02 + 1.5360394E-02T + 7.3957384E-06T^2 - 3.8423677E-09T^3)\ 0.560E-07$$

where $T\ (^\circ R)$ and $\mu(lb_m/in.-sec)$

6. Binary diffusion coefficient for water-vapor-air (31)

$$\mathcal{D}_{AB} = \frac{2.4E\text{-}07T^{1.90}}{P}$$

where T (^{o}R), P (atm) and $\mathcal{D}_{AB}$ (in.^{2}/sec)

7. Liquid density (29)

$$\rho_L = (1.5877211E\text{-}02 + 1.870149E\text{-}06T_L - 1.030489E\text{-}08T_L^{2} + 1.393879E\text{-}11T_L^{3})\ 1728^{-1}$$

where T_L (^{o}R) and ρ_L(lb$_m$/in.^{3})

N-Heptane Properties

1. Vapor pressure (45)

$$\ln P_{sat} = 11.94763 - \frac{5255.89687}{(T_L - 101.58)}$$

where T_L (^{o}R)

2. Enthalpy of vaporization (45)

$$\lambda = 139.9 + 0.181T_L - 2.7875E\text{-}04T_L^{2}$$

where $500 < T_L < 900^{o}$ R and λ(BTU/lb$_m$)

3. Vapor specific heat (45)

$$C_p = 0.119376 + 5.394E\text{-}04T$$

where $560 < T < 960^{o}$ R and C_p(BTU/lb$_m$-^{o}R)

4. Vapor thermal conductivity (45)

$$k = -1.416E\text{-}07 + 6.2222E\text{-}10T$$

where $500 < T < 1400^{o}$ R and k(BTU/in.-sec-^{o}R)

5. Vapor dynamic viscosity (45)

$$\mu = 3.92E\text{-}08 + 5.88E\text{-}10T$$

where $510 < T < 1060^{\circ}$ R and $\mu(lb_m/in.\text{-}sec)$

6. Binary diffusion coefficient for n-heptane-air (45)

$$\mathcal{D}_{AB} = (-3.131E\text{-}03 + 1.2868E\text{-}05T + 2.3927E\text{-}08T^2)/P$$

where $540 < T < 830^{\circ}$ R, P (atm), and $\mathcal{D}_{AB}(in.^2/sec)$

7. Liquid density (45)

$$\rho_L = 3.1662E\text{-}02 - 9.5355E\text{-}06T_L - 6.945E\text{-}09T_L^2$$

where $510 < T_L < 650^{\circ}$ R and $\rho_L(lb_m/in.^3)$

8. Liquid specific heat (45)

$$C_{pL} = 0.231 + 5.62E\text{-}04T_L$$

where $500 < T_L < 700^{\circ}$ R and C_{pL} $(BTU/lb_m\text{-}^{\circ}R)$

9. Critical properties (47)

$$T_c = 540.3^{\circ} K$$

$$P_c = 27.0 \text{ atm}$$

Fr-13 Properties

1. Vapor pressure (16)

$$P_{sat} = \frac{10^n}{14.696}$$

for $T_L < 475^\circ$ R

$$n = 36.7613 - 2623.988T_L^{-1} - 11.80586 \ln(T_L)/2.302588 + 5.71495E\text{-}03T_L$$

for $T_L \geq 475^\circ$ R

$$n = 56.34405 - 3351.281T_L^{-1} - 19.1691 \ln(T_L)/2.302588 + 9.20366E\text{-}03T_L$$

where T_L ($^\circ$R) and P_{sat} (atm).

2. Enthalpy of vaporization (16)

for $T_L < 500^\circ$ R

$$\lambda = -165.41314 + 1.1028303T_L - 1.336731E\text{-}03T_L^2 - 1.23949E\text{-}07T_L^3$$

for $T_L \geq 500^\circ$ R

$$\lambda = -1251.5327 + 3.7661221T_L + 7.834936E\text{-}04T_L^2 - 6.329101E\text{-}06T_L^3$$

where T_L ($^\circ$R) and λ(BTU/lb_m)

3. Vapor specific heat (14)

$$C_p = 0.1166976 - 1.0678591E\text{-}04T + 4.9459767E\text{-}07T^2 - 3.1573555E\text{-}10T^3$$

where $460 < T < 760^\circ$ R and C_p (BTU/lb_m-$^\circ$R)

4. Vapor thermal conductivity (14)

$$k = \left[0.00564 + 1.955E\text{-}05(T-460) \right] /42300$$

where $410 < T < 685^{\circ}$ R and K(BTU/in.-sec-$^{\circ}$R)

5. Vapor dynamic viscosity (28)

$$\mu = (-0.017186351 + 1.0192673E\text{-}04T - 9.879982E\text{-}08T^2 + 3.7369087E\text{-}11T^3)\ 5.60E\text{-}05$$

where $540 < T < 680^{\circ}$ R and $\mu(lb_m/in.\text{-}sec)$

6. Binary diffusion coefficient for Fr-13-air (4)

$$\mathcal{D}_{AB} = \frac{T\ 10^{(n-10)}}{(1.8)\ (6.4516)\ P}$$

where

$$n = 7.0013417 + 1.5321532\ \mathrm{Log}_{10}\ T - 1.5288892\ (\mathrm{Log}_{10}T)^2 + 0.33510243\ (\mathrm{Log}_{10}T)^3$$

and $510 < T < 680^{\circ}$ R, P (atm), and $\mathcal{D}_{AB}$ $(in.^2/sec)$

7. Liquid density (16)

$$\rho_L = \left[36.07 + 0.01566\ (543.59 - T_L) + 3.245E\text{-}05(543.59 - T_L)^2 + 1.11\ (543.59 - T_L)^{0.5} + 6.665\ (543.59 - T_L)^{1/3} \right] /1728$$

where $460 < T_L < 540^{\circ}$ R and ρ_L $(lb_m/in.^3)$

8. Liquid specific heat (15)

$$C_{pL} = -3.8797818 + 3.4082899E\text{-}02T_L - 9.1990079E\text{-}05T_L^2 + 8.1380467E\text{-}08T_L^3$$

where $410 < T_L < 535$ and C_{PL} (BTU/lb_m-^oR)

9. Critical constants

$$T_c = 302^o \text{ K}$$

$$P_c = 38.2 \text{ atm}$$

N-Heptane-Air Mixture Properties

1. N-heptane interface gas phase mole fraction (Chapter II)

$$y_{Ao} = 9.31717 - 0.00219465T_L - 3.78041E\text{-}06T_L^2 + 8.90531E\text{-}09T_L^3$$

where $540 < T_L < 570^o$ R and P = 1.5 atm abs

$$y_{Ao} = \exp[-3.039819 - 0.0565159T_L + 1.571044E\text{-}04T_L^3 - 1.034703E\text{-}07T_L^3]$$

where $540 < T_L < 720^o$ R and P = 5 atm abs

$$y_{Ao} = \exp(4.86578 - 0.0885904T_L + 1.94609E\text{-}04T_L^2 - 1.16075E\text{-}07T_L^3)$$

where $540 < T_L < 720^o$ R and P = 10 atm abs

$$y_{Ao} = -0.829433 + 4.679168E\text{-}03T_L - 8.801203E\text{-}06T_L^2 + 5.59099E\text{-}09T_L^3$$

where $536 < T_L < 698^o$ R and P = 50, 100 atm abs

2. Enthalpy of vaporization (Chapter II)

$$\lambda = 561.331 - 0.603589T_L + 1.66334E\text{-}03T_L^2 + 2.49586E\text{-}06T_L^3$$

where $540 < T_L < 570$, P = 1.5 atm abs, and λ(BTU/lb$_m$)

$$\lambda = (10229.3 - 2.23207T_L - 4.12203E\text{-}03T_L^2 + 3.07419E\text{-}07)\ 0.017964$$

where $550 < T_L < 650$, P = 5 atm abs, and λ(BTU/lb$_m$)

$$\lambda = (8595.66 - 0.654233T_L + 2.59937E\text{-}03T_L^2 - 8.22705E\text{-}06T_L^3)\ 0.017964$$

where $550 < T_L < 670$, P = 10 atm abs, and λ(BTU/lb$_m$)

$$\lambda = 120.762 - 0.087718T_L + 2.918424E\text{-}04T_L^2 - 3.066951E\text{-}07T_L^3$$

where $536 < T_L < 698^\circ$ R, P = 50 atm abs and λ(BTU/lb$_m$)

$$\lambda = 159.652 - 0.5426141T_L + 1.261746E\text{-}03T_L^2 - 9.27936E\text{-}07T_L^3$$

where $536 < T_L < 698^\circ$ R, P = 100 atm abs and λ(BTU/lb$_m$)

Fr-13-Air Mixture Properties

1. Fr-13 interface gas phase mole fraction (Chapter II)

$$y_{Ao} = 3.404846 + 1.24854E\text{-}02T_L - 1.15057E\text{-}05T_L^2 + 6.49599E\text{-}09T_L^3$$

where $420 < T_L < 460^\circ$ R and P = 28.65 atm abs

$$y_{Ao} = -1.958613 + 0.002193246T_L + 1.047311E\text{-}05T_L^2 - 8.24939E\text{-}09T_L^3$$

where $430 < T_L < 490^\circ$ R and P = 38.2 atm abs

$$y_{Ao} = 2.45118 - 9.50644E\text{-}03T_L - 1.33890E\text{-}06T_L^2 + 2.64109E\text{-}08T_L^3$$

where $430 < T_L < 490^\circ$ R and P = 47.8 atm abs

$$y_{Ao} = 4.53226 - 0.0198138T_L - 1.49072E\text{-}05T_L^2 + 1.823183E\text{-}08T_L^3$$

where $450 < T_L < 515^\circ$ R and P = 57.3 atm abs

$$y_{Ao} = 15.2447 - 0.0413856T_L - 4.16087E\text{-}05T_L^2 + 1.32523E\text{-}07T_L^3$$

where $450 < T_L < 493^\circ$ R and P = 66.9 atm abs

2. Enthalpy of vaporization

$$\lambda = 16.7298 + 0.0453331T_L + 5.20392E\text{-}04T_L^2 - 1.10909E\text{-}06T_L^3$$

where $420 < T_L < 460^\circ$ R and P = 28.65 atm abs

$$\lambda = 76.0531 - 0.0651617T_L - 4.23595E\text{-}04T_L^2 + 2.03348E\text{-}07T_L^3$$

where $430 < T_L < 490^\circ$ R and P = 38.2 atm abs

$$\lambda = -104.036 + 0.516387T_L + 1.91283E\text{-}04T_L^2 - 1.43168E\text{-}06T_L^3$$

where $430 < T_L < 490^\circ$ R and P = 47.8 atm abs

$$\lambda = -856.017 + 3.30514T_L - 1.30937E\text{-}03T_L^2 - 3.65246E\text{-}06T_L^3$$

where $450 < T_L < 515^\circ$ R and P = 57.3 atm abs

$$\lambda = 583.061 - 6.47868T_L + 3.69395E\text{-}02T_L^2 - 4.33773E\text{-}05T_L^3$$

where $450 < T_L < 493^{\circ}$ R and P = 66.9 atm abs.

APPENDIX B. DATA SUMMARY

The water data presented in Chapter V is complete; no mass transfer, droplet size or size measurements were taken. The Fr-13 histories given in the form of figures in Chapter V are complete. However, the n-heptane drop mass transfer data in Chapter V are incomplete. A complete summary of the n-heptane mass transfer data is contained in Table VI.

Table VI

Summary of n-Heptane Mass Transfer Data

Run I.D.	P(atm)	T_A(°F)	u(in./sec)	D(in.)	T_L(°F)	Measured $\frac{dm}{d\theta}$ (lb_m/sec)
6 (11-30-68)	1.5	230	58.55	0.05236	120	4.90×10^{-7}
15 (11-27-68)	5	256	29.33	0.05148	153	5.91×10^{-7}
13 (12-2-68)	10	282	15.9	0.0495	195	4.58×10^{-7}
11 (12-18-68)	50	155	5.72	0.0554	142	1.13×10^{-7}
10 (12-18-68)	50	172	5.67	0.0511	158.5	1.10×10^{-7}
8 (12-20-68)	100	144	2.08	0.060	135.5	1.10×10^{-7}
7 (12-20-68)	100	160	2.29	0.061	146.5	1.39×10^{-7}

BIBLIOGRAPHY

1. Acrivos, A., "On the Solution of the Convection Equation in Laminar Boundary Layer Flows," Chem. Eng. Sci., Vol. 17, 1962, pp. 457-465.

2. Alexander, Lee D., "The Experimental Performance of an Apparatus Designed to Study the Vaporization of a Suspended Droplet in the Vicinity of Its Critical Point," M.S. Thesis, U. of Wisconsin, 1968.

3. Flowmeter Computation Handbook, ASME Research Committee on Fluid Meters, ASME, New York, 1961.

4. Bird, R. Byron, Stewart, Warren E. and Lightfoot, Edwin N., Transport Phenomena, Wiley, New York, 1960, pp. 257-258, 505-506, 639, 656-668.

5. Boomer, E. H. et al., Can J Research, Vol. 16, 1938, p. 328.

6. Borman, G. L. et al., "Graphs of Reduced Variables for Computing Histories of Vaporizing Fuel Drops and Drop Histories Under Pressure," NACA TN4338, Sept. 1958, NACA, Washington.

7. Brzustowski, T. A. and Natarajan, R., "Combustion of Aniline Droplets at High Pressures," Can J Chem. Eng., Vol. 44, No. 4, Aug. 1966, pp. 194-201.

8. Cavett, Robert H., "Physical Data for Distillation Calculations - Vapor-Liquid Equilibria," Proceedings American Petroleum Institute, Vol. 42, Sect. III, 1962, pp. 351-366.

9. Chao, B. T., "Transient Heat and Mass Transfer to a Translating Droplet," J. Heat Transfer, Vol. 91, No. 2, May 1969, pp. 273-281.

10. Chao, K. C. and Seader, J. D., "A General Correlation of Vapor-Liquid Equilibria in Hydrocarbon Mixtures," A.I.Ch.E. Journal, Vol. 7, No. 4, Dec. 1961, pp. 598-605.

11. Chu, Ju-Chin, Distillation Equilibrium Data, Reinhold, New York, 1950, p. 163.

12. Chu, Ju-Chin et al., Vapor-Liquid Equilibrium Data, J. W. Edwards, Publisher, Inc., Ann Arbor, Michigan, 1956.

13. Chueh, P. L. and Prausnitz, J. M., "Vapor-Liquid Equilibria at High Pressures: Calculation of Critical Temperatures, Volumes, and Pressures of Nonpolar Mixtures", A.I.Ch.E. Journal, Vol. 13, No. 6, Nov. 1967, pp. 1107-1113.

14. Downing, R. C., "Transport Properties of 'Freon' Fluorocarbons," Bulletin C-30, E. I. DuPont de Nemours & Co., Inc., Wilmington, Delaware, 1965.

15. Downing, R. C., "Transport Properties of 'Freon' Fluorocarbons and Other Fluorinated Compounds," Bulletin C-30A, E. I. du Pont de Nemours and Co., Inc., Wilmington, Delaware, 1966.

16. "Thermodynamic Properties of Freon-13," Bulletin T-13, E. I. duPont de Nemours & Co., Inc., Wilmington, Delaware, 1959.

17. El-Wakil, M. M., Uyehara, O. A., and Myers, P. S., "A Theoretical Investigation of the Heating-Up Period of Injected Fuel Droplets Vaporizing in Air," NACA TN 3179, May 1954, NACA, Washington.

18. Faeth, G. M., Dominicis, D. P., and Olson, D. R., "An Investigation of Near Critical and Super-Critical Burning of Fuel Droplets," NASA CR-72314, Sept. 1967, Pennsylvania State University, University Park, Pa.

19. Galloway, T. R. and Sage, B. H., "Thermal and Material Transport from Spheres," Intern. J. Heat Mass Transfer, Vol. 10, No. 9, Sept. 1967, pp. 1195-1210.

20. Glasstone, Samuel, Textbook of Physical Chemistry, D. Van Nostrand, New York, 1946, p. 489.

21. Hall, A. R. and Diederichsen, J., "An Experimental Study of the Burning of Single Drops of Fuel in Air at Pressures up to Twenty Atmospheres," Symp. Combust., 4th, Williams and Wilkins Co., 1953, pp. 837-846.

22. Hilsenrath, Joseph et al., Tables of Thermodynamic and Transport Properties of Air, Argon, Carbon Dioxide, Carbon Monoxide, Hydrogen, Nitrogen, Oxygen and Steam, Pergamon, New York, 1960.

23. Hougen, Olaf A., Watson, Kenneth M., and Ragatz, Roland A., Chemical Process Principles, Part II, 2nd edition, Wiley, New York, 1959, pp. 931, 947-948.

24. Hsu, N. T., Sato, K., and Sage, B. H., "Material Transfer in Turbulent Gas Streams - Influence of Shape on Evaporation of Drops in N-Heptane, Ind. Eng. Chem., Vol. 46, No. 5, May 1954, pp. 870-876.

25. Hughmark, G. A., "Mass and Heat Transfer from Rigid Spheres," A.I.Ch.E. Journal, Vol. 13, No. 6, Nov. 1967, pp. 1219-1221.

26. Ingebo, Robert D., "Vaporization Rates and Heat-Transfer Coefficients for Pure Liquid Drops," NACA TN 2368, July 1951, NACA, Washington.

27. Ingebo, Robert D., "Study of Pressure Effects on Vaporization Rate of Drops in Gas Streams," NACA TN 2850, January 1953, NACA, Washington.

28. Johnson, John W., "A Correlation of the Viscosity of Fluorinated Hydrocarbon Compounds in the Liquid and Vapor Phases," Purdue University Thesis, Aug. 1962.

29. Keenan, J. H. and Keyes, F. G., Thermodynamic Properties of Steam, Wiley, New York, 1936.

30. Klyachko, L. A., "Heat Transfer Between a Gas and a Spherical Surface with the Combined Action of Free and Forced Convection," J. Heat Transfer, Vol. 85, No. 4, Nov. 1963, pp. 355-357.

31. Knsuda, T., Humidity and Moisture Measurement and Control in Science and Industry, Vol. 1, Reinhold, New York, 1965, p. 28.

32. Knuth, Eldon L., "Use of Reference States and Constant Property Solutions in Predicting Mass-, Momentum-, and Energy-Transfer Rates in High-Speed Laminar Flows," Intern. J. of Heat and Mass Transfer, Vol. 6, 1963, pp. 1-22.

33. Kreith, Frank, Principles of Heat Transfer, International, Scranton, Pennsylvania, 1965, p. 219.

34. Lenoir, J. M., Junk, W. A., and Comings, E. W., "Measurement and Correlation of Thermal Conductivities of Gases at High Pressure," Chem. Eng. Progr., Vol. 49, No. 10, Oct. 1953, pp. 539-542.

35. Manrique, Jose, "Theory of Droplet Vaporization in the Region of the Thermodynamic Critical Point," Ph.D. Thesis, U. of Wisconsin, 1969. NASA CR-72558.

36. Manrique, Jose A. and Borman, Gary L., "Calculation of Steady State Droplet Vaporization at High Ambient Pressures," Intern. J. Heat Mass Transfer, in press.

37. Meyer, C. A. et al., Thermodynamic and Transport Properties of Steam Comprising Tables and Charts for Steam and Water, ASME, New York, 1967.

38. Narasimhan, C. and Gauvin, W. H., "Heat and Mass Transfer to Spheres in High-Temperature Surroundings," Can. J. Chem. Eng., Vol. 45, No. 4, Aug. 1967, pp. 181-188.

39. Engineering Data Book, 7th edition, Natural Gasoline Supply Men's Association, Tulsa, Oklahoma, 1957.

40. Obert, Edward F., Concepts of Thermodynamics, McGraw-Hill, New York, 1960, pp. 362, 368.

41. Parmelee, H. M., "Solubility of Air in 'Freon-12' and 'Freon-22'," Refrig. Eng., Vol. 59, No. 6, June 1951, pp. 573-578.

42. Petrazhiskiy, G. B., "Experimental Investigation of Droplet Vaporization Under Conditions of High Temperatures and Pressures," (translation), NASA TT F-266, November 1964, NASA, Washington.

43. Prausnitz, J. M. et al., Computer Calculations for Multicomponent Vapor-Liquid Equilibria, Prentice-Hall, Englewood Cliffs, N. J., 1967, p. 73.

44. Priem, R. J. et al., "Experimental and Calculated Histories of Vaporizing Fuel Drops," NACA TN 3988, Aug. 1957, NACA, Washington.

45. Priem, Richard J., "Vaporization of Fuel Drops Including the Heating-Up Period," Ph.D. Thesis, U. of Wisconsin, 1955.

46. Ranz, W. E. and Marshall, Jr., W. R., "Evaporation from Drops," Chem. Eng. Progr., Part I, Vol. 48, No. 3, March 1952, pp. 141-146; Part II, Vol. 48, No. 4 April 1952, pp. 173-180.

47. Reid, Robert C. and Sherwood, Thomas K., The Properties of Gases and Liquids, Their Estimation and Correlation, 2nd edition, McGraw-Hill, New York, 1966, pp. 346-349, 379, 571-584, 596-603.

48. Ricart-Lowe, Jaime A., "Design of an Apparatus for Studying the Vaporization of Droplets in the Region of Their Critical Point," M.S. Thesis, U. of Wisconsin, 1966.

49. Rosner, D. E., "On Liquid Droplet Combustion at High Pressures," AIAA Journal, Vol. 5, No. 1, Jan. 1967, pp. 163-166.

50. Rowe, P. N., Claxton, K. T. and Lewis, J. B., "Heat and Mass Transfer from a Single Sphere in an Extensive Flowing Fluid," Trans. Inst. Chem. Eng. (London), Vol. 43, No. 1, 1965, pp. T14-T31.

51. Schenck, Hilbert, Theories of Engineering Experimentation, McGraw-Hill, New York, 1961, pp. 7, 27, 46, 56.

52. Schuh, H., "The Solution of the Laminar-Boundary-Layer Equation for the Flat Plate for Velocity and Temperature Fields for Variable Physical Properties and for the Diffusion Field at High Concentrations," NACA TM 1275, Aug. 1944, NACA, Washington.

53. Spalding, D. B., "Theory of Particle Combustion at High Pressures," ARS Journal, Vol. 29, No. 11, Nov. 1959, pp. 828-835.

54. Tee, L. S. et al., "Diffusion and Principles of Corresponding States," Proc. Am. Petrol. Inst., Vol. 46, 1966, pp. 235-243.

55. Torda, T. P. and Matlosz, Robert, "Liquid Droplet Evaporation in Stagnant High Pressure and High Temperature Environment," NASA CR-72373, May 1968, Illinois Institute of Technology, Chicago, Illinois.

56. Wertz, H. J., Personal Communication, May 1969, Madison, Wisconsin.

57. Wieber, Paul R., "Calculated Temperature Histories of Vaporizing Droplets to the Critical Point," AIAA Journal, Vol. 1, No. 2, Dec. 1963, pp. 2764-2770.

58. Winnikow, S. and Chao, B. T., "Droplet Motion in Purified Systems," Phys. Fluids, Vol. 9, No. 1, Jan. 1966, pp. 50-61.

59. Yuge, T., "Experiments on Heat Transfer from Spheres Including Combined Natural and Forced Convection," J. Heat Transfer, Vol. 82, No. 3, Aug. 1960, pp. 214-220.

60. Zenner, G. H. and Dana, L. I., "Liquid-Vapor Equilibrium Compositions of Carbon Dioxide-Oxygen-Nitrogen Mixtures," Chem. Eng. Progr. Symp. Ser., Vol. 59, No. 44, 1963, pp. 36-41.

Uncited References

Barnett, Henry C. and Hibbard, Robert R. (ed.), "Basic Considerations in the Combustion of Hydrocarbon Fuels with Air," NACA Report 1300, 1959, Lewis Lab, Cleveland, Ohio.

Brzustowski, T. A., "Chemical and Physical Limits on Vapor-Phase Diffusion Flames of Droplets," Can. J. Chem. Eng., Vol. 43, No. 1, Feb. 1965, pp. 30-35.

Downing, Carl G., "The Evaporation of Drops of Pure Liquids at Elevated Temperatures: Rates of Evaporation and Wet Bulb Temperatures," A.I.Ch.E. Journal, Vol. 12, No. 4, July 1966, pp. 760-766.

El-Wakil, M. M. et al., "Experimental and Calculated Temperature and Mass Histories of Vaporizing Fuel Drops," NACA TN 3490, Jan. 1956, NACA, Washington.

Elzinga, E. R. Jr. and Banchero, J. T., "Film Coefficient for Heat Transfer to Liquid Drops," Chem. Eng. Progr. Symp. Ser., Vol. 55, No. 29, pp. 149-161.

Griffith, R. M., "Mass Transfer from Drops and Bubbles," Chem. Eng. Sci., Vol. 12, 1960, pp. 148-213.

Groeneweg, John F., "The Statistical Description of a Spray in Terms of Drop Velocity, Size and Position," Ph.D. Thesis, U. of Wisconsin, 1967.

Kassoy, D. R. and Williams, F. A., "Liquid Droplet Combustion With Finite Rate Chemistry," AIAA Paper No. 68-181, AIAA 6th Aerospace Sciences Meeting, New York, January 22-24, 1968.

Hatsopoulos, George N. and Kennan, Joseph H., Principles of General Thermodynamics, Wiley, New York, 1965, pp. 303-309.

Hughmark, G. A., "Liquid-Liquid Spray Column Drop Size, Holdup and Continuous Phase Mass Transfer," Ind. Eng. Chem. Fundem., Vol. 6, No. 3, Aug. 1967, pp. 408-413.

Knudsen, James G. and Katz, Donald L., Fluid Dynamics and Heat Transfer, McGraw-Hill, New York, 1958, pp. 508-515.

McDowell, R. V. and Myers, J. E., "Mechanism of Heat Transfer to Liquid Drops," A.I.Ch.E. Journal, Vol. 2, No. 3, Sept. 1956, pp. 384-388.

Mehra, Vinod S., Brown, George Martin and Thodos, George, "Vapour-Liquid Equilibrium Constants up to the Critical Point for Binary Hydrocarbon Systems," Chem. Eng. Sci., Vol. 17, Jan. 1962, pp. 33-43.

Metais, B. and Eckert, E. R. G., "Forced, Mixed and Free Convection Regimes," J. Heat Transfer, Vol. 86, No. 2, May 1964, pp. 295-296.

Nordlie, Roland L. and Kreith, Frank, "Convection Heat Transfer from a Rotating Sphere," paper 54, Part II, 1961, International Heat Transfer Conference, Boulder, Colorado, New York, pp. 461-467.

Prausnitz, J. M. and Chueh, P. L., Computer Calculations for High Pressure Vapor-Liquid Equilibria, Prentice-Hall, Englewood Cliffs, N. J., 1968.

Rowe, P. N. and Claxton, K. T., "Heat and Mass Transfer from a Single Sphere to Fluid Flowing Through an Array," Trans. Inst. Chem. Eng. (London), Vol. 43, 1965, pp. 321-331.

Smith, K. A. and Smith, R. B., "Vaporization Equilibrium Constant and Activity Coefficient Charts," Petrol. Process., Vol. 4, No. 12, Dec. 1949, pp. 1355-1360.

Smith, K. A. and Watson, K. M., "High Pressure Vapor Liquid Equilibria - Activity Coefficients for Ideal Systems," Chem. Eng. Progr., Vol. 45, No. 8, 1949, pp. 494-506.

Spalding, D. B., "The Calculation of Mass Transfer Rates in Absorption Vaporization and Condensation and Combustion Processes," Proc. Inst. Mech. Eng. (London), Vol. 168, No. 19, pp. 545-570.

Spear, R. R., Robinson, R. L. and Chao, K. C., "Critical States of Mixtures and Equations of State," Ind. Eng. Chem. Fundam., Vol. 8, No. 1, Feb. 1969, pp. 2-7.

Strahle, Warren C., "The Temporal Development of a Reacting Boundary Layer Near the Stagnation Point of a Vaporizing Drop," AIAA Paper No. 69-174, AIAA 7th Aerospace Sciences Meeting, New York, New York, January 20-22, 1969.

Strom, J. R. and Kintner, R. C., "Wall Effect for the Fall of Single Drops," A.I.Ch.E. Journal, Vol. 4, No. 2, June 1958, pp. 153-156.

Williams, F. A., "On the Assumptions Underlying Droplet Vaporization and Combustion Theories," J. Chem. Phys., Vol. 33, No. 1, July 1960, pp. 133-144.

DISTRIBUTION LIST

NASA Lewis Research Center
21000 Brookpark Road
Cleveland, Ohio 44135
Attn: Dr. R.J. Priem (2)

NASA Lewis Research Center
21000 Brookpark Road
Cleveland, Ohio 44135
Attn: Norman T. Musial

NASA Lewis Research Center
21000 Brookpark Road
Cleveland, Ohio 44135
Attn: Library (2)

NASA Lewis Research Center
21000 Brookpark Road
Cleveland, Ohio 44135
Attn: Repart Control Office

NASA Scientific and Technical Information Facility
P.O. Box 33
College Park, Maryland 20740
Attn: NASA Representative (6)

NASA Lewis Research Center
21000 Brookpark Road
Cleveland, Ohio 44135
Attn: E.W. Conrad

NASA Headquarters
6th and Independence Ave, S.W.
Washington, D.C. 20546
Attn: R.W. Levine, Code RPL

NASA
George C. Marshall Space Flight Center
R-P and VE-PA
Huntsville, Alabama 35812
Attn: R.J. Richmond

NASA
Manned Spacecraft Center
Houston, Texas 77058
Attn: J.G. Thibadaux

AFRPL(RPRRC)
Edwards, California 93523
Attn: B.R. Bornhorst

AFRPL(RPPZ)
Edwards, California 93523
Attn: Capt. C.J. Abbe

Air Force Office of Scientific Research
1400 Wilson Blvd.
Arlington, Virginia 22209
Attn: B.T. Wolfson

Chemical Propulsion Information Agency
8621 Georgia Avenue
Silver Spring, Maryland 20910
Attn: T.W. Christian

U.S. Naval Weapons Center
China Lake, California 93555
Attn: D. Couch

Office of Naval Research
Navy Department
Washington, D.C. 20360
Attn: R.D. Jackel, 429

U.S. Naval Weapons Center
China Lake, California 93555
Attn: E.W. Price, Code 508

U.S. Army Missile Command
AMSMI-RKL, Attn: W.W. Wharton
Redstone Arsenal, Alabama 35808

ARL(ARC)
Attn: K. Scheller
Wright-Patterson AFB
Dayton, Ohio 45433

University of California
Department of Aeronautical Sciences
Attn: A.K. Oppenhiem
6161 Etcheverry Hall
Berkeley, California 94720

University of California
Mechanical Engineering,
Thermal System
Attn: Dr. R.F. Sawyer
Berkeley, California 94720

University of California
Aerospace Engineering Department
Attn: F.A. Williams
P.O. Box 109
LaJolla, California 92038

Jet Propulsion Laboratory
California Institute of Technology
Attn: R.M. Clayton
4800 Oak Grove Drive
Pasadena, California 91103

Jet Propulsion Laboratory
California Institute of Technology
Attn: J.H. Rupe
4800 Oak Grove Drive
Pasadena, California 91103

Colorado State University
Attn: C.E. Mitchell
Fort Collins, Colorado 80521

Dartmouth University
Attn: P.D. McCormack
Hanover, New Hampshire 03755

Georgia Institute of Technology
Aerospace School
Attn: B.T. Zinn
Atlanta, Georgia 30332

Illinois Institute of Technology
Rm 200 M.H.
Attn: T.P. Torda
3300 S. Federal Street
Chicago, Illinois 60616

Massachusetts Institute of
Technology
Department of Mechanical Engr.
Attn: T.Y. Toong
Cambridge, Massachusetts 02139

The Pennsylvania State University
Mechanical Engineering Department
Attn: G.M. Faeth
207 Mechanical Engineering Blvd.
University Park, Pa. 16802

Princeton University
James Forrestal Campus Library
Attn: I. Glassman
P.O. Box 710
Princeton, New Jersey 08540

Princeton University
James Forrestal Campus Library
Attn: D. Harrje
P.O. Box 710
Princeton, New Jersey 08540

Purdue University
School of Mechanical Engineering
Attn: J.R. Osborn
Lafayette, Indiana 47907

Sacramento State College
School of Engineering
Attn: F.H. Reardon
6000 J. Street
Sacramento, California 95819

Purdue University
Jet Propulsion Center
Attn: R. Weiss
W. Lafayette, Indiana 47907

University of Southern California
Attn: M. Gerstein, Dept. Mech. Engr.
University Park
Los Angeles, California 90007

University of Michigan
Aerospace Engineering
Attn: J.A. Nicholls
Ann Arbor, Michigan 48104

Ohio State University
Dept. of Aeronautical and
Astronautical Engineering
Attn: P. Edse
Columbus, Ohio 43210

Bell Aerosystems Company
Attn: L.M. Wood
P.O. Box 1
Mail Aone J-81
Buffalo, New York 14205

Multi-Tech., Inc.
Attn: F.B. Cramer
601 Glenoaks Blvd.
San Fernando, California 91340

Rocketdyne
A Division of
North American Aviation
Attn: E.C. Clinger
6633 Canoga Avenue
Canoga Park, California 91304

Rocketdyne
A Division of
North American Aviation
Attn: R.B. Lawhead
6633 Canoga Avenue
Canoga Park, California 91304

Purdue University
School of Aeronautics, Astronautics,
and Engineering Sciences
Attn: Dr. A.A. Ranger
Lafayette, Indiana

Aerojet-General Corporation
Attn: R. McBride
P.O. Box 296
Dept. 4921 Bldg. 160
Azusa, California 91703

Aerospace Corporation
Attn: O.W. Dykema
P.O. Box 95085
Los Angeles, California 90045

Dynamic Science, a Division
of Marshall Industries
Attn: B.P. Breen
1900 Walker Avenue
Monrovia, California 91016

Pratt and Whitney Aircraft
Florida Research and Development
Center
Attn: G.D. Garrison
P.O. Box 2691
West Palm Beach, Florida 33402

TRW Systems
Attn: G.W. Elverum
1 Space Park
Redondo Beach, California 90278

University of Connecticut
Aerospace Department
Attn: Dr. F.K. Dabora
Storrs, Connecticut 06268